Asymmetric retinal direction tuning predicts optokinetic eye movements across stimulus conditions

Scott C. Harris[1,2]* and Felice A. Dunn[1]*

1. Department of Ophthalmology, University of California, San Francisco, San Francisco, CA 94143, USA
2. Neuroscience Graduate Program, University of California San Francisco, San Francisco, CA 94158, USA
*Corresponding Authors, Scott.Harris@ucsf.edu, Felice.Dunn@ucsf.edu

ABSTRACT

Across species, the optokinetic reflex (OKR) stabilizes vision during self-motion. OKR occurs when ON direction-selective retinal ganglion cells (oDSGCs) detect slow, global image motion on the retina. How oDSGC activity is integrated centrally to generate behavior remains unknown. Here, we discover mechanisms that contribute to motion encoding in vertically-tuned oDSGCs, and leverage these findings to empirically define signal transformation between retinal output and vertical OKR behavior. We demonstrate that motion encoding in vertically-tuned oDSGCs is contrast-sensitive and asymmetric for oDSGC types that prefer opposite directions. These phenomena arise from the interplay between spike threshold nonlinearities and differences in synaptic input weights, including shifts in the balance of excitation and inhibition. In behaving mice, these neurophysiological observations, along with a central subtraction of oDSGC outputs, accurately predict the trajectories of vertical OKR across stimulus conditions. Thus, asymmetric tuning across competing sensory channels can critically shape behavior.

INTRODUCTION

From humans to insects, a wide range of organisms depend on vision to navigate their environments. When these animals respond to incoming visual information by enacting motor plans, however, relative motion is created between the eye and the visual scene. Such motion, termed “retinal slip,” has the potential to corrupt subsequent vision and threaten survival. To compensate for this possibility, the optokinetic reflex (OKR) is a highly conserved visual behavior that stabilizes retinal image motion across species (including invertebrates[1], reptiles,

amphibians, fish, birds, and all mammals, reviewed by Masseck and Hoffmann[2]). OKR consists of visually-evoked, compensatory eye movements (or head movements in some species) that offset the slow, global image motion generated by self-movement[3]. In most species, OKR also changes across stimulus conditions: adjustments to stimulus contrast, color, location, velocity, or spatial frequency, for example, can elicit distinct OKR patterns[4–11]. Nonetheless, neurophysiological mechanisms for such phenomena remain unknown.

The anatomical pathways that underlie OKR in mammals are well defined (reviewed by Masseck and Hoffmann[2], Simpson[3], Dhande et al.[12], Giolli et al.[13]). Starting in the retina, a dedicated class of biological motion detectors known as ON direction-selective retinal ganglion cells (oDSGCs) encode the slow global image motion that occurs during retinal slip. Classic work identified three types of oDSGCs that each spike maximally in response to a different cardinal direction of stimulus motion (i.e., upward/superior, downward/inferior, and nasal/anterior)[14,15]. A recent study also identified a fourth oDSGC type in mice that encodes temporal/posterior motion[16]. Projections from oDSGCs avoid typical retinorecipient structures such as the superior colliculus and lateral geniculate nucleus. Instead, axons from vertically- and horizontally-preferring oDSGCs course along dedicated retinofugal tracts to a set of midbrain nuclei known collectively as the accessory optic system. Vertically-tuned oDSGCs terminate exclusively in, and comprise the sole retinal inputs to, the medial and lateral terminal nuclei (MTN and LTN)[12,17–22] (but see Kay et al.[23] and Discussion) - though in mice, LTN is engulfed within MTN[17,21,24,25]. Here, their inputs are likely integrated into a single velocity signal that reflects the vertical component of retinal slip. This information is then relayed deeper into the brainstem where corresponding eye movements are enacted. Likewise, horizontally-tuned oDSGCs exclusively target the nucleus of the optic tract/dorsal terminal nucleus (NOT/DTN) where their signals are similarly integrated to ultimately generate the horizontal component of OKR[17,24]. While correlations have been recognized between the physiological properties of oDSGCs and OKR - particularly a matched speed tuning[26] - little is known about how signals from multiple oDSGC types are integrated to generate OKR across varying stimulus conditions[12,27].

Here, we reveal a general mechanism by which OKR may be generated across a range of stimulus statistics. First, we focus on a single parameter that is known to affect OKR: motion direction. In many species - including both humans[28–31] (but see Knapp et al.[32]) and mice[21] - OKR is more robust in response to superior motion than inferior motion. We aim to illuminate the mechanism underlying this asymmetry in order to reveal more general processes by which oDSGC signals are centrally integrated to produce OKR. Focusing on the direction-sensitivity of

vertical OKR is methodologically strategic in that (1) it limits the source of possible neurophysiological mechanisms to functions of only the vertical OKR pathway, and (2) unlike horizontal OKR, which relies on interhemispheric communication and mirror-image motion signals from each eye[2,17,33], vertical OKR can be studied unilaterally. Our results indicate that the behavioral asymmetry between superior and inferior OKR is linked to differences in the direction tuning properties of oDSGCs that prefer superior and inferior motion. These physiological differences arise from a shift in the balance of excitatory and inhibitory (E/I) synaptic inputs across cell types, along with nonlinear transformations associated with spike thresholding. More generally, we demonstrate that motion encoding in vertically-tuned oDSGCs is uniquely sensitive to such changes in synaptic input weights and show how this sensitivity, along with a central subtraction of oDSGC activity, can account for changes to OKR across additional stimulus conditions in behaving mice.

RESULTS

Superior OKR is more robust than inferior OKR

Across species, superior motion generates a more robust OKR than inferior motion (e.g. cat[33–35], chicken[36], monkey[37], human[28–31]). In mice, this phenomenon has been reported in juvenile animals[21]. To investigate if an asymmetry between superior and inferior OKR exists in adult mice, we designed a behavioral rig to accurately evoke and quantify vertical OKR in head-fixed animals (**Fig 1A-B**, **figure supplement 2,** Methods)[38]. Eye movements were measured in response to vertically-drifting, full-field gratings used previously to evoke OKR[19,21,24,39]. Across all adult mice, superior- and inferior-drifting gratings generated distinct, but reproducible eye movements: while superior gratings elicited repetitive slow, upward-drifting eye movements ("slow nystagmus") interleaved with frequent resetting saccades in the opposite direction ("fast nystagmus") (**Fig 1C**), inferior gratings tended to reliably drive only an initial slow nystagmus immediately following stimulus onset, after which fast nystagmuses were infrequent and eye position changed minimally (**Fig 1D**). To quantify these differences, we isolated periods of slow and fast nystagmus post hoc by extracting saccadic eye movements from the raw eye position trace. Superior stimuli elicited more frequent fast nystagmuses than did inferior stimuli (**Fig 1E**). In addition, the total distance traveled during slow nystagmus was greater for superior stimuli (**Fig 1F**). These results demonstrate that vertical OKR is asymmetric in adult mice.

Despite the stark asymmetry between superior and inferior OKR in response to unidirectional drifting gratings, quantifying OKR gain (ratio of eye velocity to stimulus velocity) under these conditions presented challenges due to variability in the OKR waveform across stimulus directions (**Fig 1C-D**). To better quantify gain, we designed a second stimulus in which a grating oscillated sinusoidally between superior and inferior motion while retaining a constant average position. This oscillating grating evoked sequential superior and inferior slow nystagmuses that were phase-locked to the stimulus (**Fig 1G, figure supplement 1**). Moreover gain tended to be higher during the superior stage compared to the inferior stage of individual oscillations (**Fig 1H**). This bias was reflected by an average offset of vertical eye position in the superior direction over the course of a single stimulus oscillation (**Fig 1I**). Taken together, these results demonstrate that superior motion drives a more robust OKR than inferior motion.

Superior and Inferior oDSGCs have distinct direction tuning properties

While behavioral asymmetries between superior and inferior OKR could arise anywhere along the vertical OKR pathway, a plausible neurophysiological substrate is at the level of the retina where the pathways that encode superior and inferior motion remain distinct. Further, because the ganglion cells that encode superior motion ("Superior oDSGCs") and inferior motion ("Inferior oDSGCs") together serve as an information bottleneck for the remainder of the pathway, any physiological asymmetry between these cell types will propagate to behavior unless specifically corrected for by subsequent circuitry (see Discussion). Thus, we hypothesized that the behavioral asymmetry between superior and inferior OKR may result from physiological differences between Superior and Inferior oDSGCs.

To probe oDSGCs involved in vertical OKR, we made central injections of a fluorescent retrograde tracer into their central target, MTN (**Fig 2A, figure supplement 1**). This approach labeled an average of 669±15 retinal ganglion cells (RGCs; N=20 retinas), across the contralateral retina (**Fig 2B, figure supplement 1**). Retrogradely labeled RGCs were targeted for electrophysiological investigation using epifluorescence, and we independently validated these data by using two-photon targeting in a separate set of experiments (**Fig 2 - figure supplement 3, 5;** epifluorescence targeting was used for all experiments unless otherwise specified in the figure legends). To investigate the direction tuning properties of MTN-projecting RGCs, we made cell-attached recordings from labeled RGCs while presenting a drifting bar stimulus that moved slowly (10°/s) across the retina in 8 directions (**Fig 2C**). The parameters of this stimulus matched those of the gratings used to evoke vertical OKR in behaving animals (i.e. equivalent cycle width, wavelength, and speed to the unidirectional gratings). The majority (94.76%) of retrogradely labeled RGCs were direction-selective and preferred either dorsal-to-ventral (n=116 of 286) [i.e., Superior oDSGCs, because these cells detect superior motion in visual space after accounting for inversion of the image by the eye's optics (**Fig 2D**)] or ventral-to-dorsal (i.e., Inferior oDSGCs, n=155 of 286) motion on the retina (**Fig 2E**). In agreement, mosaic analyses of soma locations indicated that retrogradely labeled cells likely consisted of two RGC types (**Fig 2 - figure supplement 1**). Both Superior and Inferior oDSGCs invariably had baseline firing rates of approximately 0 Hz (spikes/s: Sup. 0.0134±0.006; Inf. 0.0338±0.016; p=0.13 Sup. Vs. Inf.). Nonetheless, Superior oDSGCs tended to produce more total spikes than Inferior oDSGCs in response to the drifting bar stimulus (**Fig 2F-G**), and the total areas of their tuning curves were greater (**Fig 2G-H, figure supplement 3A**). Similarly, we noticed topographic differences within cell types, with MTN-projecting RGCs in dorsal retina

spiking more than those in ventral retina **(Fig 2 - figure supplement 5)**. However, the firing rates of Superior and Inferior oDSGCs covaried, with Superior oDSGCs spiking more than Inferior oDSGCs in every retinal quadrant **(Fig 2 - figure supplement 4)**.

We wondered if the difference in response magnitude between Superior and Inferior oDSGCs could be explained by a simple scaling difference of their tuning curves (i.e., same shape, different size), or if it was instead associated with an asymmetry in tuning curve shape. To answer this question, we normalized and aligned the tuning curve of each cell in our dataset to its preferred direction (vector sum, see Methods) response (**Fig 2I**). If the tuning curves of Superior oDSGCs were scaled versions of those of Inferior oDSGCs, then this normalization and alignment procedure would eliminate any apparent differences between cell types. Instead, however, we found that the normalized tuning curves of Superior oDSGCs had greater widths at 50% response magnitude (**Fig 2 - figure supplement 2A**) and total areas (**Fig 2J, figure supplement 3C**), indicating that their tuning curves were broader than those of Inferior oDSGCs. In agreement, circular Gaussian fits (see Methods) of Superior oDSGC tuning curves were consistently wider than those of Inferior oDSGCs (**Fig 2 - figure supplement 2B**). To understand how this difference in tuning curve width might affect the ability of Superior and Inferior oDSGCs to encode motion, we quantified the direction selectivity index (DSI) of each cell (magnitude of the vector sum divided by the scalar sum, see Methods). In agreement, the DSIs of Superior oDSGCs were lower than those of Inferior oDSGCs (**Fig 2K, figure supplement 3B**). Finally, we tested if these asymmetries persisted across stimulus conditions by using a drifting bar stimulus with 5-fold lower contrast. As before, Superior oDSGCs spiked more and had broader tuning curves in response to lower contrast bars (**Fig 2H, J, K insets**).

Together, these data indicate that asymmetries in vertical OKR are concomitant with prominent physiological differences between Superior and Inferior oDSGCs: Superior oDSGCs not only spike more than Inferior oDSGCs, but also have broader tuning curves. Further, tuning curve size (i.e., area of the unnormalized tuning curve) and width (i.e., direction selectivity index) were correlated on a cell-by-cell basis (**Fig 2L, figure supplement 3D**), indicating that asymmetries in these metrics could arise from a common mechanism.

Superior oDSGCs receive more excitatory input than Inferior oDSGCs

We sought to determine the source of tuning curve asymmetries between Superior and Inferior oDSGCs. As in the more widely studied class of direction-selective retinal ganglion cell known as the ON-OFF DSGCs (ooDSGCs)[40–43], oDSGCs inherit the bulk of their direction

selectivity via greater inhibition from starburst amacrine cells (SACs) in response to null direction stimuli[44–46] (reviewed by Wei[27], Mauss et al.[47], Vaney et al.[48]). Therefore, we postulated that the difference in tuning curve width between Superior and Inferior oDSGCs may result from asymmetric inhibitory inputs between the two cell types.

To investigate this possibility, we made whole-cell voltage-clamp recordings at the reversal potential for excitation to isolate inhibitory inputs to Superior and Inferior oDSGCs in response to the drifting bar stimulus (**Fig 3A-B**). Across cells, we found no significant difference in the magnitude of inhibitory postsynaptic currents (IPSCs) between Superior and Inferior oDSGCs (**Fig 3C, figure supplement 1A**). IPSCs in Superior oDSGCs, however, were slightly more direction-selective than those in Inferior oDSGCs (**Fig 3D**), which is unlikely to explain their broader spike tuning curves (see Discussion). Thus, the canonical model of retinal direction selectivity involving inhibition cannot account for the differences between Superior and Inferior oDSGC spike tuning curves.

We next asked if excitatory inputs could better explain the asymmetries between the spike tuning curves of Superior and Inferior oDSGCs. To test this possibility, we made voltage-clamp recordings at the reversal potential for inhibition to isolate excitatory postsynaptic currents (EPSCs) during the drifting bar stimulus (**Fig 3E-F**). Across stimulus directions, EPSCs in Superior oDSGCs were between 1.4 and 2.3 times greater than those in Inferior oDSGCs (**Fig 3G**). EPSCs were also less direction-selective in Superior than in Inferior oDSGCs (**Fig 3H**). In agreement, the ratio of the peak EPSC to the peak IPSC (E/I) was greater for Superior oDSGCs than for Inferior oDSGCs (**Fig 3I, figure supplement 1A-C**), though not different in direction-selectivity (**Fig 3J)**. We found no difference in the relative timing of peak EPSCs and peak IPSCs across cell types (not shown). Based on these results, the difference in spike tuning curve size and shape between Superior and Inferior oDSGCs may be related to a corresponding shift in the balance of E/I, associated with an asymmetry in the amount of net excitation that each cell type receives.

To test whether this difference in the magnitude of excitatory input to Superior and Inferior oDSGCs generalized across stimulus types, we measured the spike responses and postsynaptic currents of both cell types in response to a full-field light increment (**Fig 3 - figure supplement 2**). As with the drifting bar, the light increment elicited more total spikes in Superior than in Inferior oDSGCs. We also observed significant correlations between the magnitude of a cell's increment response and both the area of its tuning curve (Sup: $R=0.68$, $p=4.39\times10^{-17}$; Inf: $R=0.68$, $p=1.24\times10^{-23}$) and its direction selectivity index (Sup: $R=-0.26$, $p=0.005$; Inf: $R=-0.38$, $p=7.10\times10^{-7}$). Under voltage-clamp conditions, the increment evoked greater EPSCs in Superior

than Inferior oDSGCs. However, there was no difference in IPSC magnitude between cell types. Further, we found a strong correlation between the maximum firing rate of a cell to the increment and the magnitude of its peak EPSC, but not peak IPSC. These results demonstrate that Superior oDSGCs spike more than Inferior oDSGCs across multiple stimuli, and, further, that this difference in spiking is consistently associated with the amount of excitatory, but not inhibitory input.

Postsynaptic differences may account for shifts in E/I

Differences in the postsynaptic currents of Superior and Inferior oDSGCs could result from asymmetries in presynaptic wiring and/or the postsynaptic properties of each oDSGC type. Serial block-face electron microscopy[40,49,50] and analysis of dendritic stratification[21] have not yet provided evidence of presynaptic wiring differences between oDSGCs with different preferred directions. Thus, we investigated possible postsynaptic asymmetries.

We analyzed the morphology of Superior and Inferior oDSGCs by filling cells of both types with intracellular dye (**Fig 4A**). Convex hull analysis revealed that the dendritic fields of Superior oDSGCs covered a larger area than those of Inferior oDSGCs (**Fig 4B**). Sholl analysis, however, showed similar dendritic complexities (**Fig 4C**). To identify synaptic differences between cell types, we stained for the excitatory postsynaptic density scaffolding protein PSD-95[51] (**Fig 4D-F**) and the inhibitory postsynaptic scaffolding protein gephyrin[52,53] (**Fig 4G-I**). These assays revealed no difference in the number of synaptic puncta between cell types. However, Superior oDSGCs had significantly larger excitatory, but not inhibitory, puncta (**Fig 4F, I**). This anatomy is consistent with greater amounts of excitatory synaptic input to Superior oDSGCs.

To complement these morphological observations, electrophysiological recordings revealed a number of intrinsic differences between Superior and Inferior oDSGCs. First, the membrane capacitances of Superior oDSGCs were greater than those of Inferior oDSGCs (**Fig 4 - figure supplement 1A**). Sequentially recording both the spike output and EPSCs of individual oDSGCs to the full-field increment stimulus also revealed that Superior oDSGCs had lower spike-to-EPSC ratios (**Fig 3 - figure supplement 2P**). This observation persisted for each direction of the drifting bar stimulus (**Fig 3 - figure supplement 1D-AA**). In agreement, the input resistances of Superior oDSGCs were lower than those of Inferior oDSGCs (**Fig 4 - figure supplement 1B**). These phenomena are consistent with the larger size of Superior oDSGCs relative to Inferior oDSGCs (**Fig 4B**). We found no significant differences in other intrinsic

properties including the resting membrane potential and spike threshold. Together, these data indicate that Superior oDSGCs are less intrinsically excitable than Inferior oDSGCs, but that this asymmetry is outweighed by counteracting discrepancies in the magnitude of excitatory synaptic input to each cell type.

Untuned excitation broadens spike tuning curves

That Superior oDSGCs receive relatively more excitation than Inferior oDSGCs explains their greater spike output (**Fig 2F-H, figure supplement 3; Fig 3 - figure supplement 2**). Less obvious, however, is whether this difference in excitatory input can also account for the observation that Superior oDSGCs have wider tuning curves (**Fig 2I-K, figure supplement 2, 3**). A debate remains over whether excitatory inputs to DSGCs are directionally tuned[48,50,54–58] (reviewed by Wei[27]). While our results indicate that MTN-projecting RGCs might receive different amounts of excitation based on stimulus direction (**Fig 3H**), the majority of directionally tuned inputs were inhibitory (**Fig 3K**). Further, the apparent direction selectivity of EPSCs is likely partially attributable to imprecise space clamp[48,56] (but see Percival et al.[55]). Thus, the extent to which the tuning curves of Superior and Inferior oDSGCs are shaped by direction selective excitation is unclear, and we remain agnostic on this point. Instead, we focus on the more pronounced observation that Superior oDSGCs receive more excitatory input than Inferior oDSGCs across stimulus directions (**Fig 3G, I, figure supplement 1**), regardless of the extent to which this excitation is tuned. In the following experiments, we investigate the relationship between spike tuning curve shape and the overall amount of excitation to an oDSGC. We ask whether and how different magnitudes of excitatory input to Superior and Inferior oDSGCs can explain their difference in tuning curve width.

To test how the magnitude of excitation, even when directionally untuned, to an oDSGC changes the shape of its tuning curve, we measured the spikes of Superior and Inferior oDSGCs in the current-clamp configuration (**Fig 5A-B, F**) while injecting constant amounts of either positive (to add ~6 mV, “depolarizing”) or negative (to subtract ~6 mV, “hyperpolarizing”) current across stimulus directions. Importantly, the depolarizing current injections were small enough such that every cell retained a baseline firing rate of 0 Hz. This approach allowed us to investigate how providing a cell with more or less directionally-untuned excitation influences the shape of its spike tuning curve, as quantified by the direction selectivity index (a metric that decreases with greater tuning curve width) and the area of the normalized tuning curve (referred to as “normalized area,” a metric that increases with tuning curve width). We found that tuning

curves measured under depolarizing conditions were not only larger (**Fig 5C-D, G**), but also wider, with lower direction selectivity indices (**Fig 5H**) and larger normalized areas (**Fig 5 - figure supplement 1F**) than those measured under hyperpolarizing conditions. These findings are not attributable to the effects of current injection on intrinsic properties of oDSGCs (**Fig 5 - figure supplement 2**). Thus, these experiments demonstrate that increasing the amount of untuned excitation to an oDSGC broadens its tuning curve.

Comparing these results to those recorded extracellularly in cell-attached recordings revealed an additional nuance: depolarizing current injections widened only the tuning curves of Inferior oDSGCs, while hyperpolarizing injections sharpened the tuning curves of both cell types (**Fig 5C-D, figure supplement 1A-B**). One possibility is that while excitation generally broadens tuning curve width, greater excitatory input minimally affects Superior oDSGCs (**Fig 5C**) because these cells are already positioned closer to an upper limit on this phenomenon. Nonetheless, our results highlight a causal relationship between tuning curve width and the amount of untuned excitation that an oDSGC receives.

Spike threshold plays a dominant role in setting tuning curve width

Two complementary mechanisms could explain how untuned excitation widens tuning curves. In the first mechanism, excitation influences the nonlinear transformation between synaptic input and spike output that is introduced by a neuron's spike threshold (**Fig 5E**). More specifically, thresholding may sharpen a neuron's spike tuning curve relative to the tuning of underlying membrane fluctuations by clamping spike output at zero in response to subthreshold membrane responses that are likely to occur for null direction stimuli[59]. When the amount of untuned excitatory input increases, however, membrane fluctuations more readily surpass the spike threshold for all stimulus directions, thereby broadening the spike tuning curve. In the second mechanism, untuned excitation directly circularizes the tuning curve of underlying membrane potentials by increasing null direction responses proportionally more than preferred direction responses. This "additive" contribution would then be inherited by the spike tuning curve[60].

We first tested whether thresholding contributes to the width of oDSGC tuning curves. To do so, we isolated the underlying subthreshold voltages (Vm) from our current-clamp recordings that also contained spikes (**Fig 5I**). Three independent observations about these Vm tuning curves each suggests that thresholding critically influences spike tuning curve shape. First, unlike for spikes, depolarizing and hyperpolarizing current injections did not affect the direction

selectivity **(Fig 5K, N)** or normalized area (**Fig 5 - figure supplement 1G, I**) of Vm tuning curves. The total areas of Vm tuning curves were, however, slightly larger under the hyperpolarizing condition, likely due to the marginally greater driving force on excitatory conductances in this setting (**Fig 5J**). Second, the Vm tuning curves of Superior oDSGCs were larger in magnitude than those of Inferior oDSGCs (**Fig 5J arrowheads**), but also more sharply tuned, with greater direction selectivity indices (**Fig 5K arrowheads**) and smaller normalized areas (**Fig 5 - figure supplement 1G arrowheads**). This latter result was anticipated from our voltage-clamp recordings which indicated that inhibition is more direction-selective in Superior oDSGCs (**Fig 3D**). It also suggests, however, that the shape of the spike tuning curve is not directly inherited from that of the underlying membrane potential, and instead reflects the interplay between Vm magnitude and spike threshold. Third, spike tuning curves were more direction-selective **(Fig 5L-M)** and had smaller normalized areas (**Fig 5 - figure supplement 1J-K**) than those of simultaneously measured Vms for both depolarizing and hyperpolarizing injections. The difference between the shape of the spike and Vm tuning curves was smaller for the depolarizing condition, however, because in this setting the majority of stimulus directions elicited Vm responses that surpassed the spike threshold (**Fig 5O, figure supplement 1L**). Together, these three results corroborate the notion that thresholding prominently influences the width of the spike tuning curve relative to the amount of untuned excitation that an oDSGC receives.

To test the extent to which excitation broadens oDSGC tuning curves through additive effects, we recomputed Vm tuning curves after including a constant, additive offset that reflected the average current injection supplied during depolarizing and hyperpolarizing injections. These offset-corrected Vm tuning curves were significantly wider under depolarizing conditions than they were under hyperpolarizing conditions (**Fig 5 - figure supplement 1E, H**). However, the observation that (uncorrected) Vm tuning curves — in which putative additive differences *between* cell types are expected to persist — were more sharply tuned for Superior than Inferior oDSGCs (**Fig 5K, figure supplement 1G, arrowheads**) indicates that thresholding has a greater influence on spike tuning curves than does additive excitation. In agreement, current injections caused significantly larger changes in spike tuning curves than in offset-corrected Vm tuning curves (**Fig 5N, figure supplement 1I**). These results demonstrate that while untuned excitation likely has some additive effect, complementary thresholding has greater influence over oDSGC spike tuning curves.

A parallel conductance model recapitulates the influence of thresholding on oDSGC direction tuning

Together, our current injection experiments suggest that (1) spike thresholding plays a prominent role in setting the width of oDSGC tuning curves, and (2) additive effects contribute minorly. To independently test these findings, we built a parallel conductance model of an oDSGC based on empirically measured parameters from a separate set of cells to those used for the current injection experiments. Among these parameters were 8 inhibitory conductances (one for each stimulus direction), and a single, directionally-untuned excitatory conductance (**Fig 6A-B**). We then tested how manipulating the gain of the excitatory conductance affected tuning curves generated from either spikes or the peak subthreshold membrane potentials (**Fig 6C-E, figure supplement 1**) (see Methods).

Increasing the gain of untuned excitation to the model oDSGC increased the total area of both spike and Vm tuning curves (**Fig 6D**). However, while the spike tuning curve rapidly widened and became less direction-selective with increasing excitatory gain, the width of the Vm tuning curve was much less dependent on excitatory gain (**Fig 6E, figure supplement 1**). The stark difference between the spike and Vm trajectories can only be attributed to thresholding effects. On the other hand, the shallow slope of the Vm curve in **Fig 6E** reflects the additive contribution of excitation. Consistent with our physiological results, thresholding played a critical role in setting the model oDSGC's tuning curve width, whereas additive effects were relatively minor. Further, the prior observation that depolarizing current injections influenced Superior oDSGCs less than Inferior oDSGCs (**Fig 5C-D, figure supplement 1A-B**) is supported by the diminishing marginal effect of additional excitatory gain on spike tuning curve width. We also noticed that the average empirically measured direction selectivity index (**Fig 6E** circle) and normalized tuning curve area (**Figure 6 - figure supplement 1**) fell within the regime where these metrics steeply depended on excitatory gain. In this regime, thresholding effects render small changes in synaptic inputs particularly influential for oDSGC direction tuning.

Thresholding effects produce contrast-sensitive direction tuning in oDSGCs

The dependence of oDSGC tuning on thresholding predicts that any stimulus which influences the magnitude of synaptic inputs may also alter tuning curve shape. We tested this hypothesis by comparing the tuning curves of Superior and Inferior oDSGCs in response to high contrast (stimuli used in all previous figures) and 5-fold lower contrast (i.e. 20% relative

contrast) drifting bars. For most cells, the low contrast bars elicited fewer spikes (**Fig 7A-B, figure supplement 2A**). However, as for the high contrast stimuli, Superior oDSGCs tended to spike more and have wider tuning curves than Inferior oDSGCs in response to low contrast bars (**Fig 2H, J-K, insets**). Nonetheless, cells of both types had sharper spike tuning curves in response to low, compared to high, contrast stimuli (**Fig 7C, figure supplement 1A, 2B-C**). To test whether this contrast-sensitivity could be attributed to thresholding, we measured the tuning curves of subthreshold membrane potentials. While the area of Vm tuning curves was greater under high contrast conditions (**Fig 7D**), the direction selectivity (**Fig 7E**) and normalized area (**Fig 7 - figure supplement 1B**) of Vm tuning curves did not change with stimulus contrast. In agreement, the fraction of cells with spike tuning curves that sharpened under low contrast was significantly different than the equivalent fraction of Vm tuning curves that followed the same trend (DSI: p=0.0046; normalized area: p=0.0019; 2-sided Fisher's exact) (**Fig 7C,E, figure supplement 1A-B**), and Vm tuning curves were less affected by stimulus contrast than the tuning curves of simultaneously measured spikes (**Fig 7F, figure supplement 1C**). These results indicate that thresholding is critical to setting oDSGC spike tuning curve width across stimulus contrasts, just as it is across cell types.

The finding that oDSGCs are contrast-sensitive departs from previous work which has shown that direction tuning in ooDSGCs is contrast-invariant[61–63]. Contrast-invariance in ooDSGCs appears to rely on the stability of E/I across contrasts. For this reason, we tested whether the contrast-sensitivity of oDSGCs was associated with a mutable E/I by sequentially measuring excitatory and inhibitory synaptic currents for preferred and null direction stimuli across contrasts. Our data show that E/I in neither the preferred nor null direction changed systematically with contrast (**Fig 7 - figure supplement 1D-E**). Further, the fraction of cells with spike tuning curves that sharpened under low contrast conditions was significantly greater than the fraction of E/I ratios that were lower under low contrast conditions (DSI: PD p=0.0044, ND p=0.0044; normalized area: PD p=0.0132, ND p=0.0132; 2-sided Fisher's exact) (**Fig 7C, figure supplement 1A, D-E**). These results suggest that as in ooDSGCs, E/I in oDSGCs is relatively stable across contrasts. However, the spike tuning curves of oDSGCs are nonetheless contrast-sensitive. Thus, stable E/I alone is insufficient to maintain the contrast-invariance of spikes. In the case of oDSGCs, changes to the absolute magnitude of synaptic inputs across contrasts, along with thresholding effects, appear to trump the contrast-invariance of E/I.

To further test the extent to which the magnitude of synaptic inputs can affect oDSGC tuning curves even with stable E/I, we revisited our parallel conductance model of an exemplary oDSGC. We modeled oDSGC responses while changing the gain of excitatory and inhibitory

conductances together, thereby keeping E/I constant while nevertheless adjusting the total magnitude of E and I. As in our empirical data, lowering the gain of E and I together to simulate responses to low contrast stimuli resulted in sharper spike tuning curves. The width of Vm tuning curves, however, remained relatively contrast-invariant (**Fig 7 - figure supplement 1F**). These results recapitulate our empirical findings and indicate that the spike threshold nonlinearity influences spike tuning curve width across contrasts. Other stimulus parameters that affect the magnitude of excitation, inhibition, or both are also likely to modulate the direction tuning properties of oDSGCs.

A subtraction algorithm predicts vertical OKR from oDSGC activity

Having established the tuning properties of Superior and Inferior oDSGCs, we asked whether the asymmetries between these cell types, along with their contrast-sensitivities, could explain how vertical OKR changes across stimulus conditions. Cross-species work has established that Superior and Inferior oDSGCs are likely centrally integrated by a subtraction algorithm[3,22,64]. In this model, OKR is predicted on the basis of the *difference* in spike rate between Superior and Inferior oDSGCs, rather than by the absolute spike rate of either cell type. A number of observations support this model: (1) stimuli that activate both Superior and Inferior oDSGCs (e.g. a full-field increment of light) do not elicit OKR, (2) stimuli that differentially activate Superior and Inferior oDSGCs (e.g. drifting gratings) maximally drive OKR (**Fig 1, 2**), (3) Superior and Inferior oDSGCs project to separate MTN subnuclei[21,22] that are mutually connected by inhibitory interneurons (i.e., a simple differentiating circuit)[22,65], (4) MTN neurons prefer either superior or inferior motion[21,22,64,66–68], but their preferred and null directions are not 180° apart; instead, they correspond to the preferred directions of opposing oDSGC types[64,67,68], which may differ by less than 180° [15] (but see Sabbah et al.[16]), and (5) MTN neurons maintain moderate baseline spike rates that are both augmented by preferred direction stimuli and diminished by null direction stimuli[64,66–68]. Together, along with the simplicity of the vertical OKR pathway and its isolation from other visual circuits, these lines of evidence all point to a circuit motif in which MTN neurons encode the difference in spike rate between Superior and Inferior oDSGCs. Thus, superior OKR likely occurs when Superior oDSGCs spike sufficiently more than Inferior oDSGCs, and vice versa. The robustness of OKR is putatively related to the magnitude of the spike rate difference (**Fig 8A**).

We used our empirically recorded electrophysiology data from Superior and Inferior oDSGCs to generate hypotheses for how OKR gain would change across stimulus conditions. Superior and Inferior oDSGC firing rate distributions were compared for superior and inferior drifting bars at high (full) and low (20% relative) contrast (i.e., four stimulus conditions) (**Fig 8B, figure supplement 1B-E**). We inferred that the relative OKR gain under each stimulus condition would be related to the corresponding difference in spike rate between Superior and Inferior oDSGCs under that same condition. For instance, gain in response to a high contrast superior grating was predicted by the difference between the preferred direction responses of Superior oDSGCs and the null direction responses of Inferior oDSGCs to high contrast bars. Importantly, such inferences constitute linear predictions of gain. Allowing for the possibility that downstream circuitry incorporates additional monotonic nonlinearities, a linear prediction is consistent with behavior so long as it predicts gain changes in the correct *direction* (but not magnitude) across stimulus conditions.

The asymmetries in the tuning curves of Superior and Inferior oDSGCs resulted in the following key predictions for how OKR gain would change across stimulus directions and contrasts: (1) gain would decrease with stimulus contrast, (2) OKR would be asymmetric, with superior stimuli eliciting greater gain than inferior stimuli, and (3) this asymmetry between responses to superior and inferior stimuli would decrease with stimulus contrast (**Fig 8C, figure supplement 1**). Next, we tested these predictions in behaving mice. OKR in the superior and inferior directions was measured in response to high (full) and low (20% relative) contrast oscillating gratings. All of the linear predictions were consistent with behavior (**Fig 8H, figure supplement 1, 3**). Most notably, gain decreased with stimulus contrast (**Fig 8H, figure supplement 1H-I, P, figure supplement 3**), and the asymmetry between superior and inferior OKR that we originally noticed under high contrast conditions diminished in response to low contrast stimuli (**Fig 8H, figure supplement 1L-M, Q, figure supplement 3**). While these results may be related, they do not *necessitate* each other, and instead rely on further subtleties in the relationship between Superior and Inferior oDSGC responses at both contrasts. Indeed, permuting the behavioral predictions by scrambling which cellular responses were assigned to superior/inferior motion and high/low contrast revealed that only 5 permutations (out of 256 possibilities, 1.95%) accurately matched our behavioral results. Consistent with these findings, the relationship between our linear predictions and behavioral results was fit well by a monotonic function that was near linear within the measured regime (**Fig 8D**).

Finally, we tested whether instantaneous subtraction of Superior and Inferior oDSGC firing rates on millisecond timescales could also predict vertical OKR behavior. We directly

recorded the spikes of Superior and Inferior oDSGCs in response to oscillating gratings with the same parameters as those used to induce behavioral OKR. This stimulus evoked more spikes in Superior oDSGCs as gratings drifted dorsal to ventral on the retina (superior motion), and more spikes in Inferior oDSGCs as gratings drifted ventral to dorsal on the retina (inferior motion) (**Fig 8E - figure supplement 2C-D**). To make behavioral predictions, the average population instantaneous firing rates of Superior and Inferior oDSGCs were subtracted every 5 milliseconds over the course of an oscillation cycle (**Fig 8 – figure supplement 2E-F**). Such values constituted linear predictions of instantaneous eye velocity for each time point, and their cumulative integrals yielded predictions of eye position (**Fig 8F, figure supplement 2G-H**). Recordings were initially made in response to both high (full) and 20% relative contrast gratings, however, the low contrast condition failed to evoke consistent spiking in oDSGCs. Thus, we instead used high (full) and 50% relative contrast gratings to predict how responses would change across contrasts (see Methods). Moment-by-moment subtraction of oDSGC firing rates indicated that (1) eye movements would track the sinusoidal pattern of stimulus motion, (2) gain would decrease with decreasing stimulus contrast, (3) OKR would be asymmetric with greater gain in response to superior motion than inferior motion, and (4) asymmetries between Superior and Inferior OKR would decrease with decreasing stimulus contrast. Not only do these predictions match those generated from the drifting bar stimulus, but they also accurately predict OKR in behaving mice (**Fig 8H**). The moment-by-moment difference between Superior and Inferior oDSGC firing rates was also generally linearly related to the time-matched eye velocity of behaving animals, with nonlinear regimes occurring only at extreme firing rate differences (**Fig 8G**). Together, these results provide a neurophysiological explanation for how vertical OKR changes across multiple stimulus conditions and reveal that the circuit and cellular properties that shape oDSGC motion encoding have direct and predictable consequences for behavior.

DISCUSSION

Our results depict a neurophysiological mechanism by which vertical OKR changes across stimulus conditions. We demonstrate that superior and inferior OKR are asymmetric in adult mice (**Fig 1**), and show how this behavioral phenomenon can be traced to novel asymmetries in the direction tuning properties of Superior and Inferior oDSGCs (**Fig 2**). Mechanistically, a shift in the balance of excitatory and inhibitory inputs across cell types

influences direction tuning, primarily through an effect associated with spike thresholding (**Fig 3-6**). Similar thresholding effects also confer contrast-sensitivity of the spike tuning curve, even when E/I is contrast-invariant (**Fig 7**). Together, these cellular properties accurately predict how vertical OKR changes with stimulus direction and contrast (**Fig 8**).

Directional asymmetries in OKR are common across species. Besides the vertical asymmetries investigated here, horizontal OKR is asymmetric in many organisms[2,69]. This asymmetry manifests nearly universally as higher OKR gain in response to temporal-to-nasal (anterior) motion than to nasal-to-temporal (posterior) motion, and often only when stimuli are viewed monocularly. Such horizontal asymmetries may similarly be linked to direction tuning in the retina: while anterior-preferring oDSGCs are critical to horizontal OKR[12,24,39], posterior-preferring oDSGCs were only recently identified in rodents and display distinct direction tuning properties compared to their anterior-preferring counterparts[16]. Further, a subtraction mechanism between horizontally tuned oDSGCs may also underlie horizontal OKR[33]. However, at least two confounds obscure a connection between the tuning properties of Anterior and Posterior oDSGCs and asymmetries in horizontal OKR. First, oDSGCs in the left and right eyes, and their contralateral central targets (NOT/DTN), encode different absolute directions of stimulus motion (reflection occurs over the sagittal body axis). To compensate, signals are compared across eyes/hemispheres prior to behavior[33], and, in some species, NOT/DTN receives descending, often binocular, inputs from visual cortex[2,13,70,71]. Second, recent studies have suggested that ooDSGCs could be involved in horizontal OKR[17,23]. Asymmetries in the horizontal version of the behavior may thus depend on more complex considerations.

Analogous confounds are less concerning when considering the mechanisms that could account for asymmetries in vertical OKR. For one, stimuli that induce vertical OKR, such as the gratings used here, are perceived identically by both eyes. Interhemispheric communication is unlikely to influence behavior under such conditions. Though signals are probably also exchanged between the horizontal and vertical OKR pathways[3,13,18], these channels may play a minimal role in shaping OKR to purely vertical stimuli. Finally, while it has been suggested that a vertically-tuned ooDSGC may also project to MTN[23], this cell type was not clearly revealed by either anatomical or electrophysiological analyses during our retrograde labeling experiments (**Fig 2 - figure supplement 1; Fig 3 - figure supplement 2**). Instead, we find that two populations of ganglion cells project to MTN, and that these cells can be classified as Superior and Inferior oDSGCs. These results are consistent with characterizations of MTN-projecting RGCs across many species[20,21,72–74]. Thus, unlike for horizontal OKR, asymmetries in vertical OKR can be explained more simply by the physiology of oDSGCs.

Despite the possibility that asymmetries in vertical and horizontal OKR are influenced by separate mechanisms, the two phenomena could share a common ethological function. Optic flow associated with forward locomotion typically includes a large posterior component. Thus, it has been suggested that posterior OKR is less reliable than anterior OKR in order to mitigate lateral eye movements that might otherwise occur when an animal walks forward[75]. Similar reasoning may explain the asymmetry between superior and inferior OKR[28,35,37]. Indeed, recent work in freely moving mice demonstrated that optic flow has a stronger inferior than superior component[76]. Thus, the cellular and behavioral asymmetries identified in this study may provide an ethological advantage by mitigating aberrant eye movements during forward locomotion. Future work should address this possibility by mapping OKR gain as a function of the extent to which various stimuli reflect locomotion-associated optic flow.

From a physiological perspective, our results provide the first evidence that Superior and Inferior oDSGCs encode motion asymmetrically. Superior oDSGCs produce more spikes and have broader tuning curves than Inferior oDSGCs (**Fig 2**). These findings coincide with previous work demonstrating genetic[77] and anatomical differences between oDSGC types. Multiple transgenic lines are known to label either Superior or Inferior oDSGCs, but not both[18,20,21,74]. The axons of Superior and Inferior oDSGCs take separate retinofugal tracts and project to different MTN subnuclei in mice[21]. Additional differences exist between vertically- and horizontally-tuned oDSGCs[12,24]. The competitive advantage of mitigating OKR during forward locomotion may have thereby shaped the development of many differences between oDSGC types.

The asymmetric spike tuning of Superior and Inferior oDSGCs is associated with differences in the magnitude of excitatory synaptic input to each cell type (**Fig 3**). Three synaptic partners are primary candidates for the source of this asymmetry: (1) glutamatergic input from bipolar cells (types 5 and 7), (2) cholinergic input from SACs, and (3) glutamatergic input from VGluT3 amacrine cells[44–46,49,50,58,78,79]. Glutamatergic conductances in oDSGCs rely on AMPARs and NMDARs, whereas cholinergic conductances rely on nicotinic AChRs[80]. These conductances have been studied primarily in ooDSGCs and deserve further characterization in oDSGCs. Interestingly, VGluT3 amacrine cells also corelease glycine, which cancels oDSGC spiking in response to high-velocity stimuli[49,57,78,79]. Asymmetries at the VGluT3-oDSGC synapse could coincide with differences in the speed tuning properties of Superior and Inferior oDSGCs. A combination of genetic, optical, and pharmacological manipulations could distinguish among these possible sources of asymmetric tuning.

In addition to the gain of excitatory inputs, other mechanisms could contribute to tuning curve differences between Superior and Inferior oDSGCs. Debate remains over the extent to

which excitatory inputs to DSGCs are directionally tuned[48,50,54–58]. Our data indicate that excitation may be less direction selective in Superior than in Inferior oDSGCs (**Fig 3H**), which could contribute to their broader spike tuning curves. Qualitatively, excitation also showed a bimodal average tuning curve in Superior oDSGCs (**Fig 3G**) that matched their average spike tuning curve (**Fig 2G**). However, bimodal spike tuning curves also resulted from directionally untuned depolarizing current injections in both cell types (**Fig 3C-D**), so the influence of excitatory tuning remains unclear. In addition, previous studies with simultaneous somatic and dendritic recordings have revealed that dendritic spikes in rabbit oDSGCs contribute to directional tuning[81]. Different spatial distributions of voltage-gated sodium channels along dendrites could also contribute to asymmetric direction tuning between oDSGC types. Indeed, we show that Superior and Inferior oDSGCs have distinct morphologies (**Fig 4**). Thus, while a single compartment conductance model captured the empirical data in this study (**Fig 6**), development of multi-compartment models could elucidate potential contributions of dendritic spikes to asymmetric tuning between oDSGC types. Intriguingly, however, among mechanisms that are unlikely to explain differences between Superior and Inferior oDSGC tuning curves is that of direction selective inhibition. We find that inhibition is more sharply tuned in Superior oDSGCs (**Fig 3C, D**), and that this is associated with sharper Vm tuning curves (**Fig 5K, arrowheads**). To explore this relationship in more depth, analyses leveraging our parallel conductance model also demonstrated that, all else equal, sharper inhibitory tuning contributes to sharper Vm and spike tuning in oDSGCs (not shown). Nonetheless, empirically measured spike tuning curves are broader in Superior oDSGCs than in Inferior oDSGCs (**Fig 2J-K**). Thus, while the relationship between inhibitory tuning curve shape and spike tuning curve shape is nuanced and requires further investigation, the difference in spike tuning curve shape between Superior and Inferior oDSGCs is unlikely to be explained by inhibitory tuning. Evidently, other mechanisms, including differences in excitatory gain (**Fig 3G**), counteract and outweigh the influence of differences in inhibition. Consequently, a comprehensive understanding of direction selectivity will require mapping the contributions of mechanisms that have been less well-studied than directionally tuned inhibition.

Further insight into how oDSGCs encode motion can be gained by comparing their tuning properties to those of the more comprehensively studied ooDSGCs. While prior work has focused on speed tuning as the primary difference between oDSGCs and ooDSGCs[14,26,49,57,79], our results reveal an additional difference between these two classes of DSGCs that has been previously overlooked: oDSGCs are contrast-sensitive (**Fig 7**), whereas ooDSGCs are not[62]. In ooDSGCs, preservation of E/I across contrasts is apparently critical for retaining

contrast-invariant direction tuning[61,63]. Counterintuitively, we find that E/I in oDSGCs is also relatively stable across contrasts (**Fig 7 - figure supplement 1D-E**). Therefore, stability of E/I is not alone sufficient for contrast-invariant spike tuning; independence from thresholding effects is also required. Indeed, thresholding modulates oDSGC direction tuning following changes to either E/I (**Fig 5-6**) or the absolute magnitude of E and I (**Fig 7 - figure supplement 1F**). Evidently, the influence of thresholding constitutes a major difference in the mechanisms that govern how oDSGCs and ooDSGCs encode motion.

That E/I is contrast-insensitive in both oDSGCs and ooDSGCs also indicates some extent of shared circuitry between these cell types. Contrast-invariance of E/I in ooDSGCs relies on postsynaptic NMDA conductances and constrains possible presynaptic wiring motifs[61,63]. oDSGCs likely share many of these features. Indeed, serial block-face electron microscopy has confirmed that oDSGCs and ooDSGCs share many of their presynaptic partners[40,43,49,50,54]. Nonetheless, differences in the intrinsic properties between and within DSGC classes, including dependence on thresholding, could magnify the impact of subtle circuit differences on spike output.

Finally, our results show that vertical OKR is predicted by a simple subtraction between the outputs of Superior and Inferior oDSGCs (**Fig 8**). It is interesting that asymmetries in oDSGCs are not apparently corrected by downstream circuitry, considering that normalization operations pervade the nervous system[82]. One explanation is that there is no simple compensatory solution to normalize the responses of Superior and Inferior oDSGCs because multiple stimulus parameters (e.g., stimulus direction and contrast) simultaneously affect the asymmetry magnitude. On the other hand, the ethological advantage of asymmetric OKR (i.e mitigating aberrant eye movements during forward locomotion) may have provided sufficient evolutionary pressure to allow asymmetries between Superior and Inferior oDSGCs to propagate to behavior when they might otherwise have been compensated. Regardless, a linear subtraction of oDSGC outputs offers an accurate and parsimonious explanation of vertical OKR. Moreover, this algorithm fits well with both the anatomy and physiology of MTN and the isolation of the vertical OKR pathway from other visual circuits[13,21,22,64–68].

Similar subtraction algorithms are prevalent across the animal kingdom. In the mammalian retina, such computations confer both the spatial center-surround[83–85] and chromatic dichotomy[86–88] of receptive fields. In Drosophila, spatially offset antennae allow accurate estimation of wind velocity by differentiation of signals across two input sites[89]. Similar mechanisms likely underlie tropotaxic orienting behaviors that also rely on spatially offset receptors, including arthropod antennae[90], reptile forked tongues[91], and mammalian ears[92]. The

ubiquity of this circuit motif may reflect an efficient solution for integrating complementary information streams. Our results highlight how such circuits can be influenced by subtle asymmetries across input channels. Further investigation will determine whether diverse sensory systems rely on asymmetric inputs to adaptively change behavior across stimulus conditions.

ACKNOWLEDGEMENTS

We would like to thank Connie Chen and Jeremiah John for technical assistance; Annika Balraj, Kevin Bender, David Copenhagen, Luca Della Santina, Daniel Denman, Tonatiuh Garcia Ruiz, Jonathan Horton, Jeanette Hyer, David Kastner, Joo Yeun Lee, Yien Ming-Kuo, Satoru Miura, Yvonne Ou, Massimo Scanziani, Manuel Solino, and Alfred Yu for helpful discussions; David Berson, Guy Bouvier, and Fred Rieke for comments on the manuscript. This work was supported by NIH through F31 EY-033225 (S.C.H.), R01 EY-029772 (F.A.D.), R01 EY-030136 (F.A.D.), and the Vision Core Grant P30 EY-002162 (UCSF), internally by the Moritz-Heyman Discovery Fellowship (S.C.H.) and the Kavli Institute for Neuroscience (UCSF), and through foundation grants from the McKnight Scholar Award (F.A.D.), Research to Prevent Blindness (Unrestricted Grant), and That All May See (UCSF).

AUTHOR CONTRIBUTIONS

Both authors conceptualized the project, designed experiments, and constructed experimental rigs. S.C.H. conducted and analyzed the behavioral and electrophysiological experiments and performed the modeling. F.A.D. conducted and analyzed the confocal imaging. Both authors wrote the manuscript and acquired funding and resources.

DECLARATION OF INTERESTS

The authors declare no competing interests.

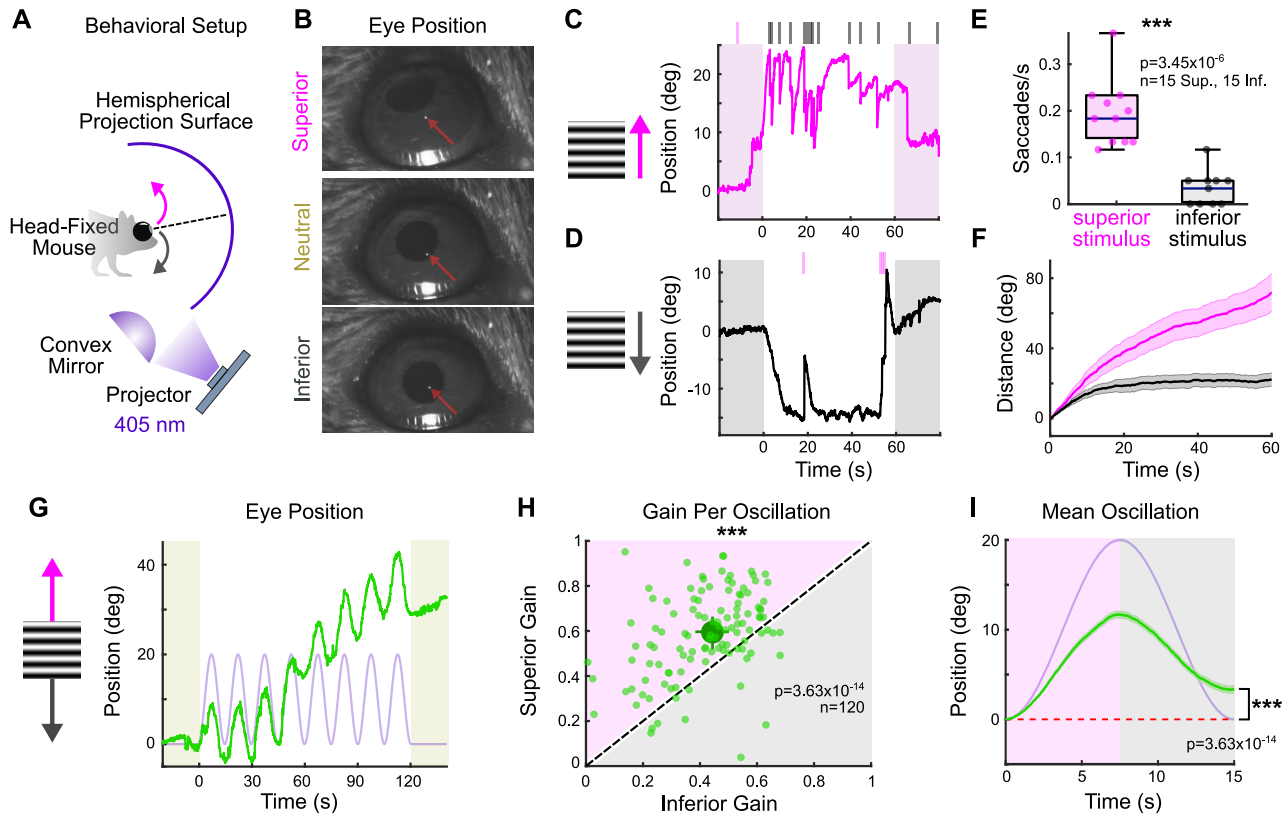
A
Behavioral Setup
Hemispherical Projection Surface
Head-Fixed Mouse
Convex Mirror
Projector
405 nm
B
Eye Position
Superior
Neutral
Inferior
C
Position (deg)
D
Position (deg)
Time (s)
E
***
p=3.45x10^-6
n=15 Sup., 15 Inf.
Saccades/s
superior stimulus
inferior stimulus
F
Distance (deg)
Time (s)
G
Eye Position
Position (deg)
Time (s)
H
Gain Per Oscillation
***
Superior Gain
Inferior Gain
p=3.63x10^-14
n=120
I
Mean Oscillation
Position (deg)
***
p=3.63x10^-14
Time (s)

Figure 1

Figure 1. Superior and inferior OKR are asymmetric in adult mice. (A) Schematic of behavioral setup to elicit the vertical optokinetic reflex (OKR). The mouse is situated so that one eye is centered in a hemisphere. Stimuli are projected onto the hemisphere's concave surface via reflection off of a convex mirror. Eye movements are tracked using an infrared-sensitive camera and corneal reflection (see Methods). **(B)** Example video frames demonstrating that the eye traverses between superior, neutral, and inferior positions in the presence of vertically-drifting sinusoidal gratings. Red arrows mark the infrared corneal reflection. **(C-D)** Example of OKR in response to full-contrast **(C)** superior and **(D)** inferior drifting gratings (10°/s). For each epoch, a continuous 60 second stimulus was flanked by 20 seconds of a static grating (shaded regions). Ticks above the plots mark the time of fast nystagmus either in the superior (magenta) or inferior (gray) direction. Examples from one animal. **(E)** Rate of vertical fast nystagmus for superior and inferior stimuli on each epoch for N=5 mice. Horizontal line represents median, box boundaries are the interquartile range (IQR), whiskers represent most extreme observation within 1.5xIQR. **(F)** Cumulative vertical distance traveled during slow nystagmus in response to superior (magenta) and inferior (gray) drifting gratings (mean±SEM). **(G)** Example of OKR in response to a vertically oscillating sinusoidal grating. The eye position is shown in green and the stimulus position is shown in lavender. Saccades ("fast nystagmuses") have been removed to reveal the asymmetry between superior and inferior OKR. For each epoch, animals viewed 8 oscillation cycles lasting a total of 120 seconds, flanked by 20 seconds of a static grating (shaded regions). **(H)** Average gain of slow nystagmus during the superior versus inferior stage of individual oscillations. Each small dot is a single oscillation. The region of magenta [or gray] indicates that gain was greater for the superior [or inferior] stage of the oscillation. Points that fall on the line indicate equivalent gain for both stimulus directions. Large point and whiskers represent univariate medians and 95% confidence intervals (via bootstrapping), respectively. Significance value indicates whether the points tend to fall unevenly on one side of the unity line (2-sided signed-rank). **(I)** Eye position (green) and stimulus position (lavender) averaged across all oscillations and all animals (mean±SEM). Starting eye position is normalized to 0° at cycle onset. The average ending eye position is displaced in the superior direction (2-sided signed-rank). N=5 mice for all experiments; n=number of trials. *p<0.05, **p<0.01, ***p<0.001.

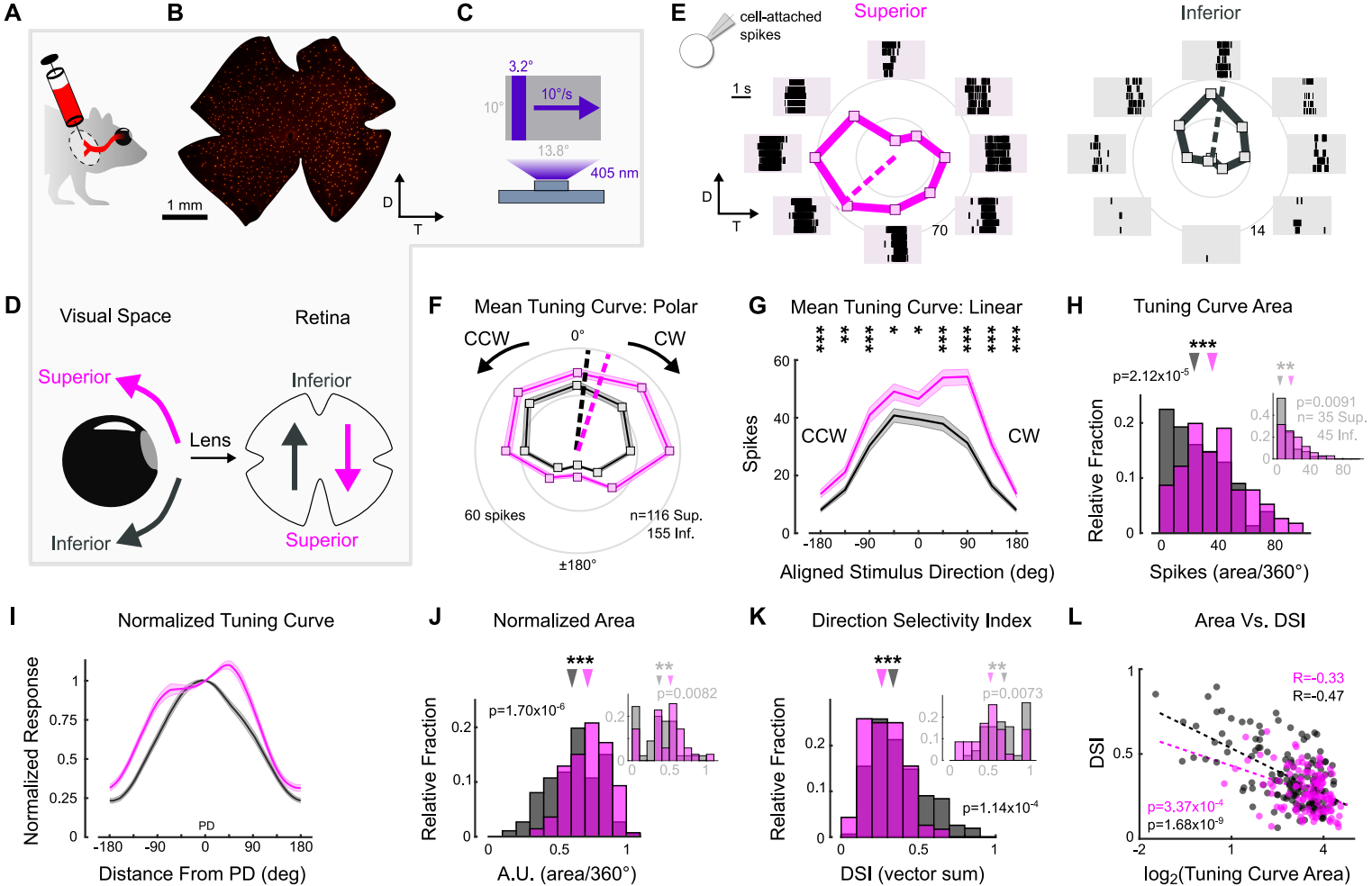
A
B
C
1 mm
D
T
3.2°
10°/s
10°
13.8°
405 nm
E
cell-attached spikes
Superior
Inferior
1 s
70
14
D
Visual Space
Retina
Superior
Inferior
Lens
Inferior
Superior
F
Mean Tuning Curve: Polar
CCW
CW
0°
60 spikes
n=116 Sup.
155 Inf.
±180°
G
Mean Tuning Curve: Linear
Spikes
CCW
CW
Aligned Stimulus Direction (deg)
H
Tuning Curve Area
p=2.12x10-5
p=0.0091
n= 35 Sup.
45 Inf.
Relative Fraction
Spikes (area/360°)
I
Normalized Tuning Curve
Normalized Response
PD
Distance From PD (deg)
J
Normalized Area
p=1.70x10-6
p=0.0082
Relative Fraction
A.U. (area/360°)
K
Direction Selectivity Index
p=0.0073
p=1.14x10-4
Relative Fraction
DSI (vector sum)
L
Area Vs. DSI
R=-0.33
R=-0.47
p=3.37x10-4
p=1.68x10-9
DSI
log2(Tuning Curve Area)

Figure 2

Figure 2. Superior and Inferior oDSGCs have asymmetric spike tuning curves. **(A)** Schematic illustrating unilateral bead injections into medial terminal nucleus (MTN) to retrogradely label ganglion cells in the contralateral retina. **(B)** Flat-mount retina with retrogradely labeled, MTN-projecting ganglion cells. **(C)** Drifting bar stimulus (3.2° x limiting projector dimension, 10°/s, 2.4×10^4 S-cone photoisomerization/s). **(D)** Definitions of superior (magenta) and inferior (gray) motion in visual space and on the retina. Directions are inverted by the lens. **(E)** Cell-attached spikes from labeled retinal ganglion cells in a flat-mount retina in response to a bar drifting in 8 directions. Spike responses and average tuning curves from example Superior (left, magenta) and Inferior (right, gray) oDSGCs. Mean spike counts are presented as the distance from the origin, marked by concentric circles. Numbers on circles indicate spike counts. Dashed lines represent the preferred direction of each cell, calculated as the direction of the vector sum of all responses. Coordinates are in retinal space. **(F-G)** Population tuning curves across all Superior and Inferior oDSGCs (mean±SEM). **(F)** Polar plots [as in (E)] aligned by rotating the tuning curves of Superior cells by 180°. **(G)** Linear representation of the same data (referred to as the "linear tuning curve"). CW: clockwise, nasal for Superior oDSGCs, temporal for Inferior oDSGCs; CCW: counterclockwise, temporal for Superior oDSGCs, nasal for Inferior oDSGCs. 0° represents directly superior/inferior motion. **(H)** Histograms of the area under the curve of the linear tuning curve of every cell. Inset shows the same metric for a stimulus at 20% relative contrast. **(I)** Population mean (±SEM) normalized tuning curves - computed by normalizing and aligning (at 0°) the response of each cell to its response in the preferred direction. **(J)** Histograms of the area under the curve of the normalized tuning curve [as in (I)] of every cell (referred to as "normalized area"). A larger normalized area indicates a wider tuning curve. Inset shows the same metric for a stimulus at 20% relative contrast. **(K)** Histograms of the direction selectivity index (DSI, vector sum, see Methods) of every cell. Inset shows the same metric for a stimulus at 20% relative contrast. **(L)** Linear tuning curve area, [as in (H)] and direction selectivity index [as in (K)] were correlated (Spearman's rank) on a cell-by-cell basis for both Superior and Inferior oDSGCs. Dashed lines are least squares linear regressions, R and p values are Spearman's rank correlation coefficient and associated 2-sided p-value, respectively. For all histograms, medians of Superior (magenta) and Inferior (gray) oDSGC distributions are indicated by arrows. *$p<0.05$, **$p<0.01$, ***$p<0.001$.

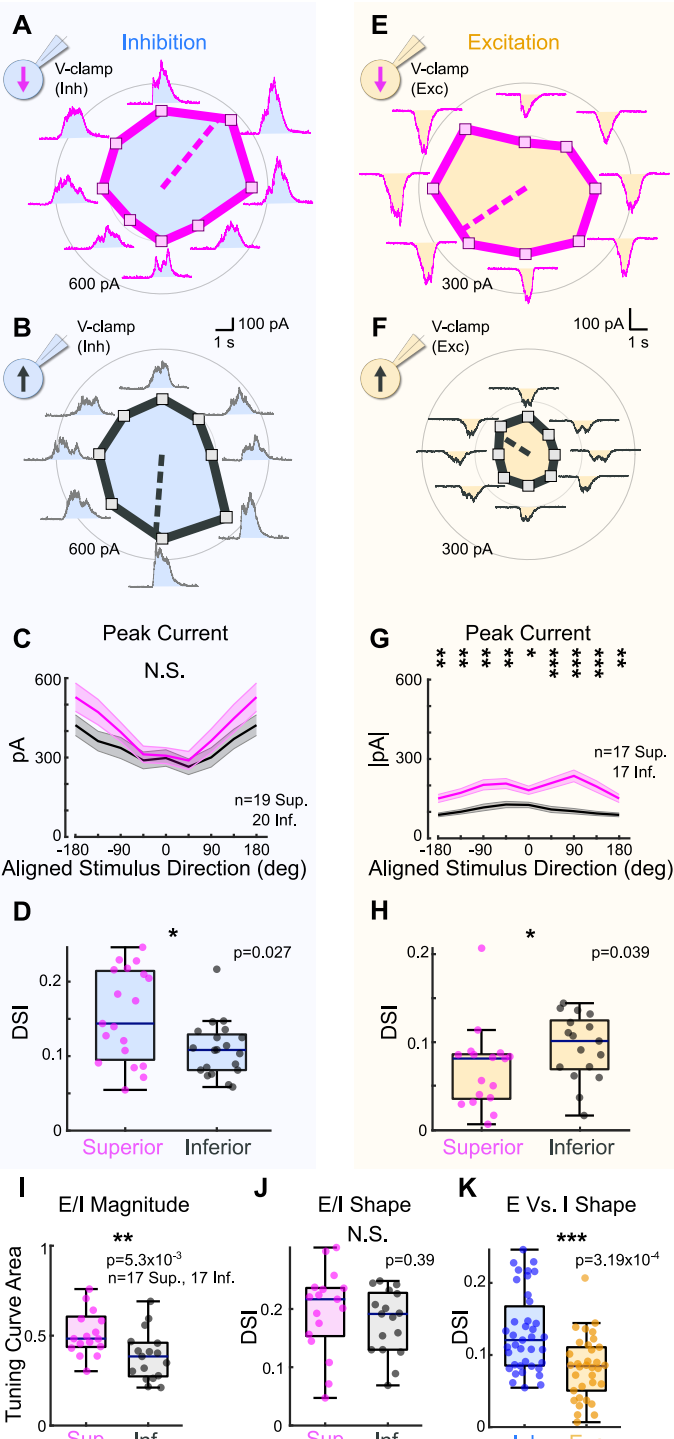
A
Inhibition
V-clamp
(Inh)
600 pA
B
V-clamp
(Inh)
100 pA
1 s
600 pA
C
Peak Current
N.S.
600
300
0
pA
n=19 Sup.
20 Inf.
-180
-90
0
90
180
Aligned Stimulus Direction (deg)
D
*
p=0.027
0.2
0.1
0
DSI
Superior
Inferior
E
Excitation
V-clamp
(Exc)
300 pA
F
V-clamp
(Exc)
100 pA
1 s
300 pA
G
Peak Current
** ** ** ** * *** *** *** **
600
300
0
|pA|
n=17 Sup.
17 Inf.
-180
-90
0
90
180
Aligned Stimulus Direction (deg)
H
*
p=0.039
0.2
0.1
0
DSI
Superior
Inferior
I
E/I Magnitude
**
p=5.3x10-3
n=17 Sup., 17 Inf.
1
0.5
0
Tuning Curve Area
Sup.
Inf.
J
E/I Shape
N.S.
p=0.39
0.2
0.1
0
DSI
Sup.
Inf.
K
E Vs. I Shape
***
p=3.19x10-4
0.2
0.1
0
DSI
Inh.
Exc.

Figure 3

Figure 3. Superior oDSGCs receive similar inhibitory inputs but greater excitatory inputs compared to Inferior oDSGCs. (A) Inhibitory currents measured from an exemplar Superior oDSGC under voltage-clamp at +10 mV in response to a bar drifting in 8 directions. **(B)** Same as (A) for an exemplar Inferior oDSGC. **(C)** Population responses for peak inhibitory currents across stimulus directions for Superior (magenta) and Inferior (gray) oDSGCs (mean±SEM). Stimulus directions are aligned across cell types, where 0° indicates directly superior (for Superior oDSGCs) or inferior (for Inferior oDSGCs) motion. Positive directions are clockwise. **(D)** Distributions of the direction selectivity index for peak inhibitory currents in individual Superior and Inferior oDSGCs. **(E)** Excitatory currents measured from an exemplar Superior oDSGC under voltage-clamp at -60 mV in response to a bar drifting in 8 directions. Same cell as in (A). **(F)** Same as (E) for an exemplar Inferior oDSGC. Same cell as in (B). **(G)** Population responses for peak excitatory currents across stimulus directions for Superior (magenta) and Inferior (gray) oDSGCs (mean±SEM). **(H)** Distributions of the direction selectivity index for peak excitatory currents in individual Superior and Inferior oDSGCs. **(I-J)** The ratio of the peak excitatory current to the peak inhibitory current (E/I) was calculated for each stimulus direction for cells in which both metrics were recorded. **(I)** Distributions of the linear tuning curve area of E/I. **(J)** Distributions of the direction selectivity index for E/I. **(K)** Direction selectivity index for peak inhibitory (blue) and excitatory (yellow) currents collapsed across Superior and Inferior oDSGCs. For box plots, horizontal line represents median, box boundaries are IQR, and whiskers represent the most extreme observation within 1.5xIQR. *$p<0.05$, **$p<0.01$, ***$p<0.001$.

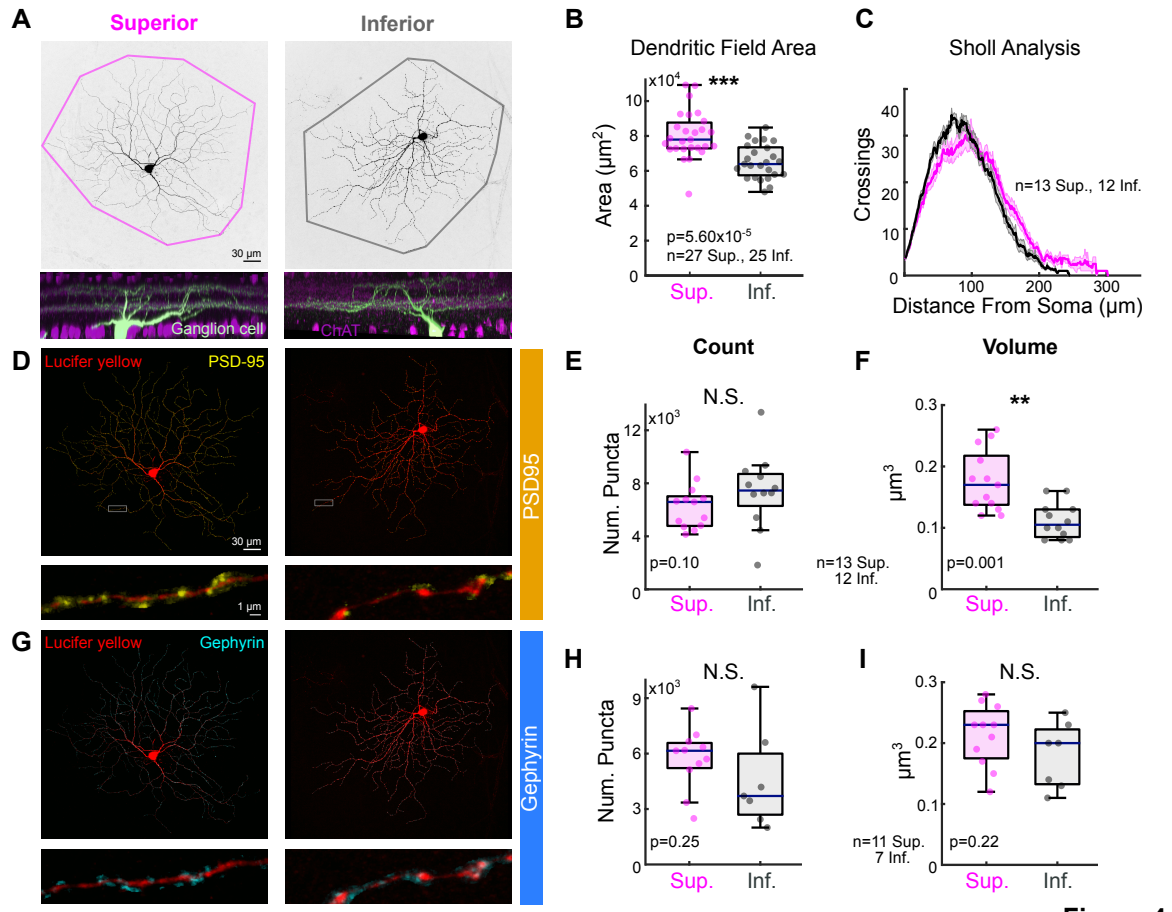
A
Superior
Inferior
30 µm
Ganglion cell
ChAT
B
Dendritic Field Area
x10^4
***
Area (µm^2)
p=5.60x10^-5
n=27 Sup., 25 Inf.
Sup.
Inf.
C
Sholl Analysis
Crossings
n=13 Sup., 12 Inf.
Distance From Soma (µm)
D
Lucifer yellow
PSD-95
30 µm
1 µm
PSD95
E
Count
N.S.
x10^3
Num. Puncta
p=0.10
n=13 Sup.
12 Inf.
F
Volume
**
µm^3
p=0.001
G
Lucifer yellow
Gephyrin
Gephyrin
H
N.S.
x10^3
Num. Puncta
p=0.25
I
N.S.
µm^3
n=11 Sup.
7 Inf.
p=0.22

Figure 4

Figure 4. Superior oDSGCs have greater dendritic fields and larger excitatory postsynaptic sites. (A) Confocal images of a Superior (left) and Inferior (right) oDSGC filled with dye. Convex polygons are drawn around the tips of their dendrites. (Bottom) Side views of different Superior and Inferior oDSGCs filled and stained for acetylcholinesterase (ChAT) bands. Both cell types have dendrites that stratify in the ON and OFF ChAT bands, with the majority of dendrites in the ON sublamina. **(B)** Convex polygon areas across cells. **(C)** Sholl analysis indicating the number of dendritic crossings as a function of radial distance from the soma (mean±SEM). **(D, H)** Ganglion cells with immunostaining for **(D)** excitatory postsynaptic scaffolding protein PSD-95 or **(H)** inhibitory postsynaptic scaffolding protein gephyrin. (Bottom) Magnification of a stretch of dendrites with labeled puncta. **(E, G)** Total number of puncta within each ganglion cell for **(E)** PSD-95 and **(G)** gephyrin. **(F, H)** Quantification of average puncta volume for **(F)** PSD-95 and **(H)** gephyrin. For box plots, horizontal line represents median, box boundaries are IQR, and whiskers represent the most extreme observation within 1.5xIQR. *$p<0.05$, **$p<0.01$, ***$p<0.001$.

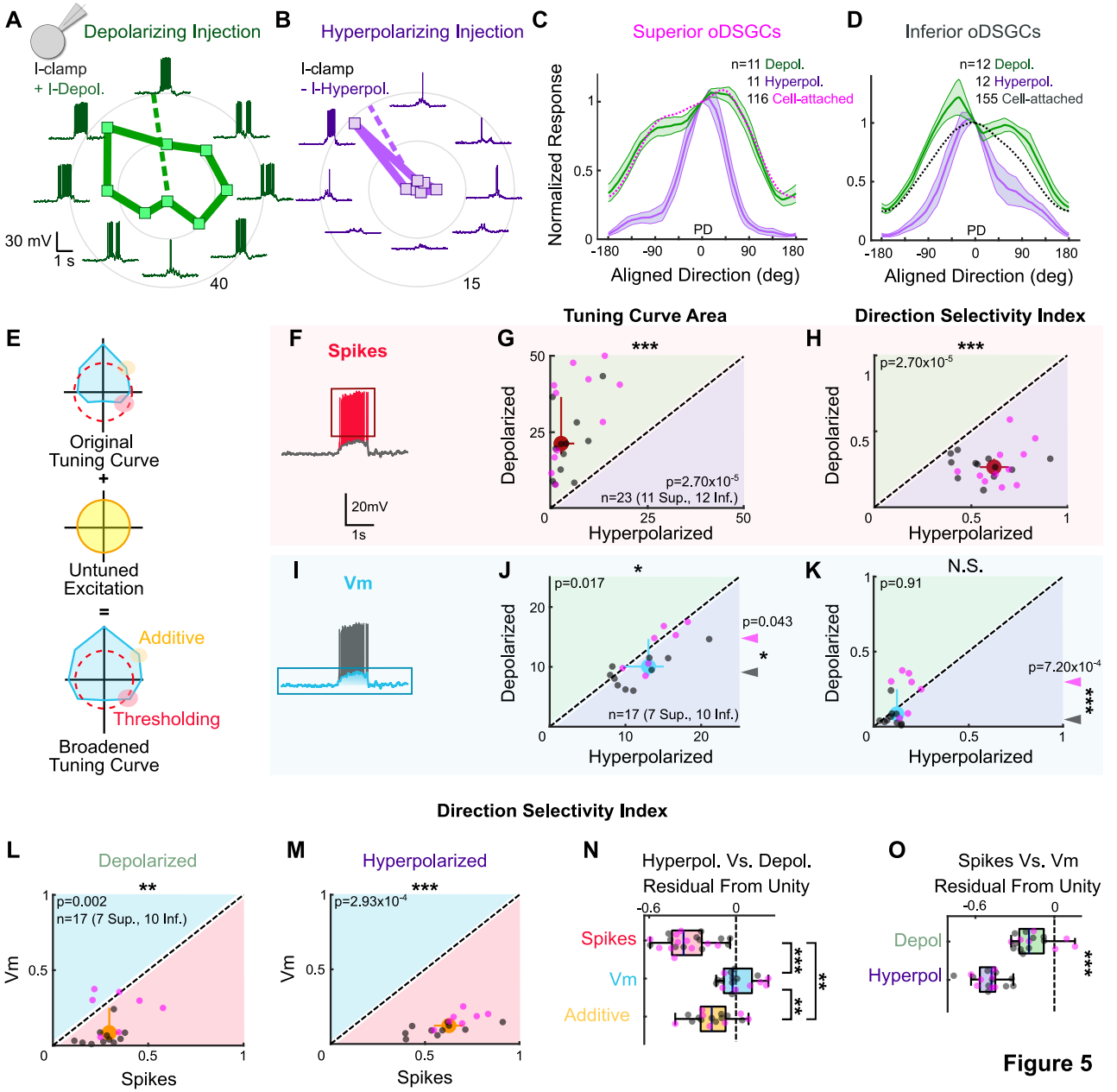
A
Depolarizing Injection
I-clamp
+ I-Depol.
30 mV
1 s
40
B
Hyperpolarizing Injection
I-clamp
- I-Hyperpol.
15
C
Superior oDSGCs
n=11 Depol.
11 Hyperpol.
116 Cell-attached
Normalized Response
PD
Aligned Direction (deg)
D
Inferior oDSGCs
n=12 Depol.
12 Hyperpol.
155 Cell-attached
PD
Aligned Direction (deg)
E
Original
Tuning Curve
+
Untuned
Excitation
=
Additive
Thresholding
Broadened
Tuning Curve
F
Spikes
20mV
1s
G
Tuning Curve Area
***
Depolarized
Hyperpolarized
p=2.70x10-5
n=23 (11 Sup., 12 Inf.)
H
Direction Selectivity Index
***
p=2.70x10-5
Depolarized
Hyperpolarized
I
Vm
J
*
p=0.017
p=0.043
*
n=17 (7 Sup., 10 Inf.)
Depolarized
Hyperpolarized
K
N.S.
p=0.91
p=7.20x10-4
***
Depolarized
Hyperpolarized
Direction Selectivity Index
L
Depolarized
**
p=0.002
n=17 (7 Sup., 10 Inf.)
Vm
Spikes
M
Hyperpolarized
***
p=2.93x10-4
Vm
Spikes
N
Hyperpol. Vs. Depol.
Residual From Unity
Spikes
Vm
Additive
***
**
**
O
Spikes Vs. Vm
Residual From Unity
Depol
Hyperpol
***

Figure 5

Figure 5. Thresholding differentiates the tuning properties of Superior and Inferior oDSGCs. (A-B) Exemplar Inferior oDSGC in whole-cell current-clamp during **(A)** depolarizing and **(B)** hyperpolarizing current injection in response to a bar moving in 8 directions. Numbers on concentric circles indicate spike counts. **(C-D)** Mean (±SEM) normalized tuning curves (aligned and normalized to the response of each cell in its preferred direction) for **(C)** Superior and **(D)** Inferior oDSGCs under conditions of depolarizing (green) and hyperpolarizing (purple) current injection. Dotted lines indicate the average normalized spike tuning curves of each population from cell-attached recordings (as in Fig 2I). **(E)** Illustration of the influence of untuned excitation on the tuning curve through additive (yellow) and thresholding (red) effects. The blue area indicates the membrane potential and the dashed red line indicates the spike threshold. **(F, I)** Example whole-cell current-clamp recording in which **(F)** spikes and **(I)** subthreshold voltages (Vm) have been separated. **(G)** Linear tuning curve area and **(H)** direction selectivity index of the spike tuning curve metrics during hyperpolarizing (abscissa) and depolarizing (ordinate) current injections. **(J)** Linear tuning curve area and **(K)** direction selectivity index of subthreshold membrane potential tuning curves. For (G-H, J-K), regions of green [or purple] indicate that the metric is greater during depolarizing [or hyperpolarizing] injections. Points that fall on the line indicate equivalent metrics under the two conditions. Individual cells are shown as dots (Superior in magenta, Inferior in gray). Red and blue circles represent univariate medians (collapsed across cell type) and whiskers indicate 95% confidence intervals determined via bootstrapping. Significance values indicate whether the data tend to fall unevenly on one side of the unity line (2-sided signed-rank). Arrowheads in (J-K) represent the median of Superior (magenta) and Inferior (gray) oDSGCs along the unity line, and associated significance values indicate comparison between Superior and Inferior oDSGCs (2-sided rank-sum). **(L-M)** Direction selectivity index for spikes (abscissa) and simultaneously measured subthreshold voltages (ordinate) under **(L)** depolarizing and **(M)** hyperpolarizing conditions. Significance values indicate whether the data tend to fall unevenly on one side of the unity line (2-sided signed-rank). **(N)** Residuals from the unity line for individual cells from the plots in (H) and (K). Dashed line indicates unity (i.e. no difference across depolarizing and hyperpolarizing conditions). **(O)** Residuals from the unity line for individual cells from the plots in (L) and (M). Dashed line indicates unity (i.e., no difference between spikes and subthreshold voltages). Comparisons in (N-O) are made between conditions (2-sided rank-sum). For box plots, the blue line represents median, box boundaries are IQR, and whiskers represent the most extreme observation within 1.5xIQR. *$p<0.05$, **$p<0.01$, ***$p<0.001$.

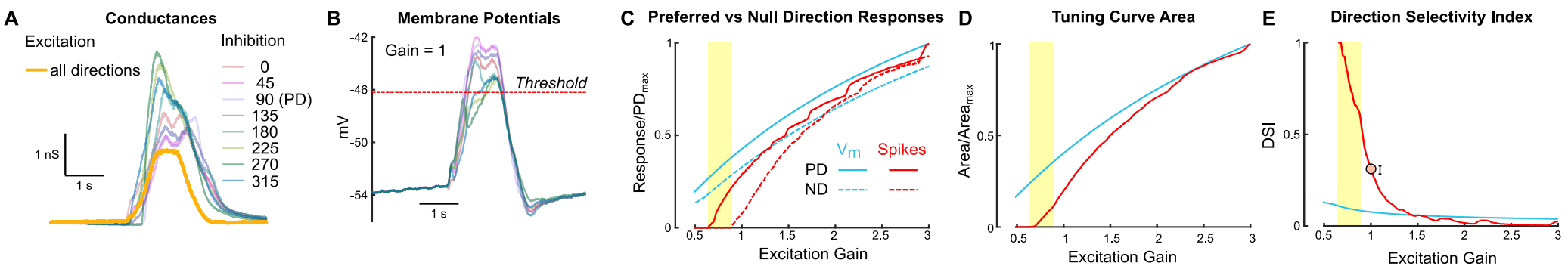
A
Conductances
Excitation
all directions
Inhibition
0
45
90 (PD)
135
180
225
270
315
1 nS
1 s
B
Membrane Potentials
Gain = 1
Threshold
mV
-42
-46
-50
-54
1 s
C
Preferred vs Null Direction Responses
Response/PD$_{max}$
Vm
Spikes
PD
ND
Excitation Gain
D
Tuning Curve Area
Area/Area$_{max}$
Excitation Gain
E
Direction Selectivity Index
DSI
I
Excitation Gain

Figure 6

Figure 6. A parallel conductance model demonstrates how untuned excitation contributes to direction tuning. An exemplar oDSGC was modeled using parameters recorded directly from cells, including directionally tuned inhibitory conductances for each drifting bar direction, and a single, untuned excitatory conductance (see Methods). **(A)** Inhibitory (pastel colors) and excitatory (yellow) conductances of the model oDSGC in response to bars moving in 8 directions. **(B)** The parallel conductance model uses the empirically measured parameters to model membrane potential across bar directions, shown here for the case in which the excitatory gain (i.e. a multiplication factor applied to the excitatory conductance) is set to 1.0. The red dotted line indicates the spike threshold. **(C)** Preferred (solid lines) and null (dotted lines) direction responses of subthreshold voltages (blue) and spikes (red) across a range of excitatory gains. Values are normalized to the maximum preferred direction response for each metric. The yellow column indicates the regime in which the null direction elicits zero spikes but the preferred direction has nonzero spikes, an example of nonlinear behavior caused by the spike threshold. **(D-E)** Directional tuning properties as a function of excitatory gain for subthreshold voltages (blue) and spikes (red): **(D)** area of the linear tuning curve (normalized to the maximum area for each metric), and **(E)** direction selectivity index. Orange dot [and error bars] in (E) correspond to the empirically measured median [and 95% confidence intervals determined via bootstrapping] for each metric from cell-attached recordings, collapsed across cell types.

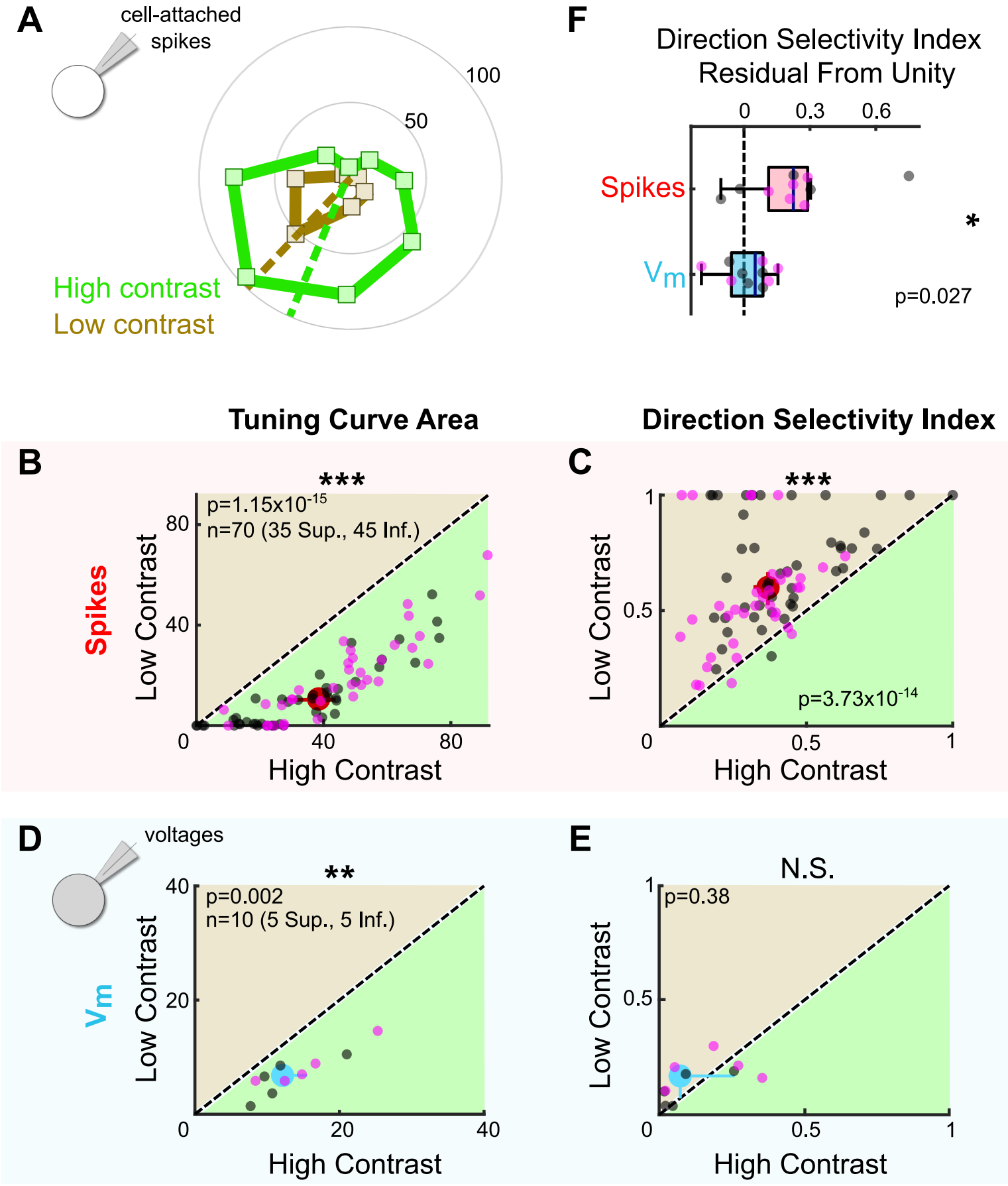
A
cell-attached
spikes
100
50
High contrast
Low contrast
F
Direction Selectivity Index
Residual From Unity
0
0.3
0.6
Spikes
Vm
*
p=0.027
Tuning Curve Area
Direction Selectivity Index
B
***
p=1.15x10-15
n=70 (35 Sup., 45 Inf.)
Spikes
Low Contrast
High Contrast
C
***
p=3.73x10-14
D
voltages
**
p=0.002
n=10 (5 Sup., 5 Inf.)
Vm
E
N.S.
p=0.38

Figure 7

Figure 7. Stimulus contrast modulates the spike tuning curves of oDSGCs. (A) Example cell-attached tuning curves from a Superior oDSGC at high (green) and low (tan) contrasts. Numbers on concentric circles indicate spike counts. **(B)** Linear tuning curve area and **(C)** direction selectivity index from spike responses to high (abscissa) and low (ordinate) contrast bars drifting in 8 directions. Differences between Superior (magenta) and Inferior (gray) oDSGCs persist under low contrast (see Fig 2). **(D)** Linear tuning curve area and **(E)** direction selectivity index from subthreshold voltage responses to high (abscissa) and low (ordinate) contrast bars drifting in 8 directions. **(F)** Residuals from the unity line of the direction selectivity index under high and low contrast conditions for simultaneously measured spikes and subthreshold voltages. Comparison is made across conditions. For all scatter plots, the region of green [or tan] indicates the metric is greater under high [or low] contrast conditions. Points on the line indicate equivalent metrics under the two conditions. Individual cells are represented by small dots. Large dots represent univariate medians (collapsed across cell type). Whiskers indicate 95% confidence intervals determined via bootstrapping. Significance values indicate whether the data tend to fall unevenly on one side of the unity line (2-sided signed-rank). *$p<0.05$, **$p<0.01$, ***$p<0.001$

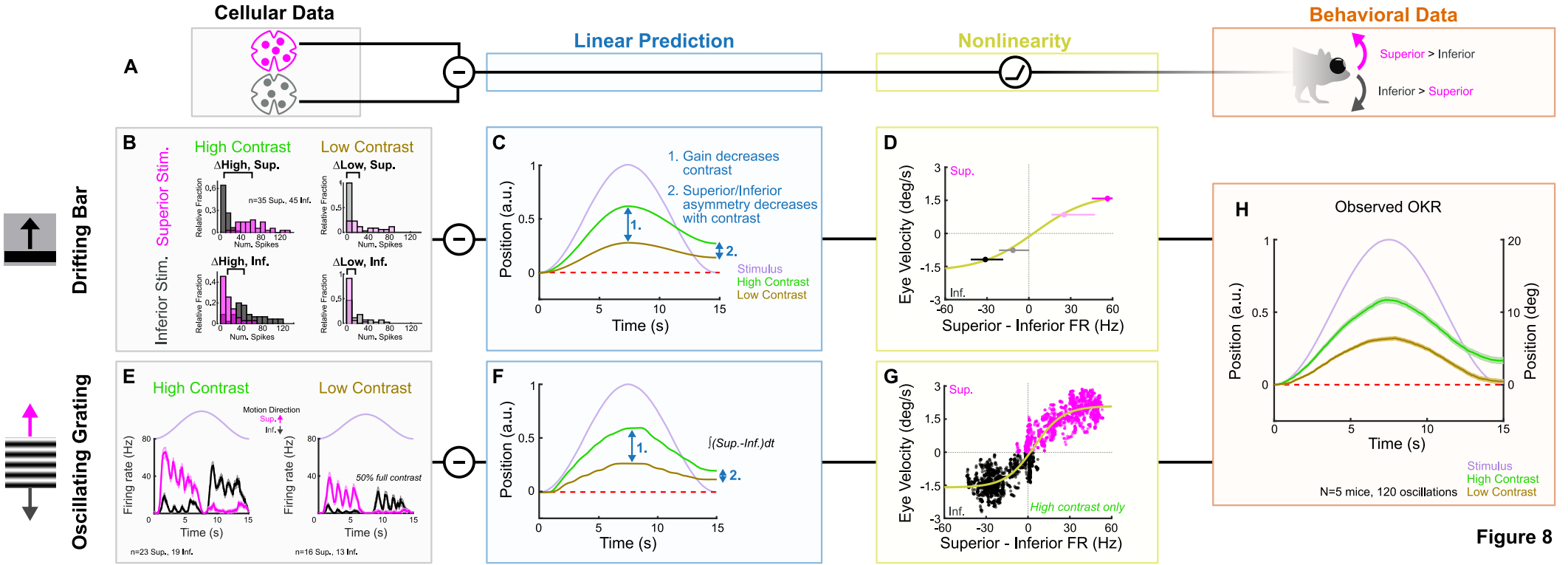
Cellular Data
Linear Prediction
Nonlinearity
Behavioral Data
A
Superior > Inferior
Inferior > Superior
Drifting Bar
Oscillating Grating
B
High Contrast
Low Contrast
Superior Stim.
Inferior Stim.
ΔHigh, Sup.
ΔLow, Sup.
ΔHigh, Inf.
ΔLow, Inf.
n=35 Sup., 45 Inf.
Relative Fraction
Num. Spikes
C
1. Gain decreases contrast
2. Superior/Inferior asymmetry decreases with contrast
Position (a.u.)
Time (s)
Stimulus
High Contrast
Low Contrast
D
Sup.
Inf.
Eye Velocity (deg/s)
Superior - Inferior FR (Hz)
H
Observed OKR
Position (a.u.)
Position (deg)
Time (s)
N=5 mice, 120 oscillations
E
High Contrast
Low Contrast
Motion Direction
Sup.
Inf.
Firing rate (Hz)
Time (s)
50% full contrast
n=23 Sup., 19 Inf.
n=16 Sup., 13 Inf.
F
∫(Sup.-Inf.)dt
G
High contrast only

Figure 8

Figure 8. oDSGC responses predict behavioral OKR across stimulus types, directions, and contrasts. (A) Schematic of the putative computation between oDSGCs and OKR, consisting of a subtraction between Superior and Inferior oDSGC spikes and a nonlinearity. **(B-H)** Two separate implementations of the subtraction model described in (A). **(B-D)** Prediction of OKR behavior from oDSGC responses to the drifting bar stimulus. **(B)** Distributions of Superior (magenta) and Inferior (gray) oDSGC spike responses across high (left) and low (right, 20% relative) contrast superior (top) and inferior (bottom) drifting bars. The brackets denote the difference between the medians of the Superior and Inferior oDSGC response distributions in each condition. **(C)** Linear predictions of OKR are made for the average gain over the course of each half oscillation cycle based on the difference in firing rate between Superior and Inferior oDSGCs [i.e. brackets in (B)] to high and low contrast bars drifting in the corresponding direction. The shape of the curves as sinusoids is inferred from the stimulus position over time (lavender). **(D)** The empirically computed nonlinearity shows the relationship between linear behavioral predictions [as in (C)] from the drifting bar stimulus and the corresponding average eye velocities measured during behavioral OKR experiments for superior (magenta points) and inferior (gray points) stimuli at high (dark points) and low (light points) contrast. The points indicate univariate medians for each condition and whiskers are 95% confidence intervals computed via bootstrapping (vertical error bars are too small to see). The solid line is a fitted sigmoid function of the form $v(r) = \frac{(v_{min} - v_{max})}{(1+10^{(r_{50}-r)m})}$, where v_{min} is the minimum eye velocity, v_{max} is the maximum eye velocity, r_{50} is the firing rate along the azimuth that corresponds to the inflection point, m controls the slope, and $v(r)$ is the expected eye velocity for a given firing rate, r. The fit curve has parameters $v_{min} = -1.71$, $v_{max} = 1.79$, $r_{50} = 4.10$, $m = 0.022$. **(E-G)** Prediction of OKR behavior from oDSGC responses to an oscillating sinusoidal grating. **(E)** Median responses of Superior (magenta) and Inferior (gray) oDSGCs across a single cycle of the oscillating grating for high (left) and low (right, 50% relative) contrast stimuli. Lavender traces represent the relative position of the stimulus across time. Directions of superior/inferior motion are indicated by arrows. These recordings were made using two-photon targeting. **(F)** Linear predictions of OKR are made by subtracting the instantaneous firing rates of Superior and Inferior oDSGCs across time. **(G)** The empirically computed nonlinearity shows the difference between Superior and Inferior oDSGC firing rates plotted against the time-matched average eye velocity of behaving animals. Each small point represents the firing rate difference

and eye velocity at a single time point over the course of one stimulus oscillation cycle. Magenta points represent superior eye velocities (i.e. above 0 on the ordinate) and gray points represent inferior eye velocities (i.e. below 0 on the ordinate). The solid line is a fitted sigmoid curve of the form described in (D) and has parameters $v_{min} = -1.60$, $v_{max} = 2.09$, $r_{50} = 4.42$, and $m = 0.042$. Only data for the high contrast condition were used. **(H)** Mean eye position of behaving mice in response to a single oscillation of a high (green, as in Fig 1I) or low (tan, 20% relative) contrast gratings. Compare to linear predictions in (C) and (F).

MATERIALS AND METHODS

RESOURCE AVAILABILITY

Lead Contact

Further information and requests for resources and reagents should be directed to and will be fulfilled by the Lead Contact, Felice Dunn (Felice.Dunn@ucsf.edu).

Material availability

This study did not generate new unique reagents.

Data and code availability

- All data reported in this paper is publicly available at datadryad.org/stash/share/4B8W-Q-8rAbneQkAKQLw4HS8PPqZhT_83t_DkU35NcA
- All original code for visual stimulus generation and confocal image analysis has been deposited on Github and is publically available as of the date of publication. The information is listed in the key resources table.
- Any additional information required to reanalyze the data reported in this paper is available from the lead contact upon request.

EXPERIMENTAL MODEL AND SUBJECT DETAILS

Animals: Adult wildtype C57BL/6 mice between the ages of postnatal day P60 and P100 of both sexes were used for all experiments. Animals were kept on a 12 hour dark-12 hour light cycle with continuous access to food and water. All experiments were performed in accordance with protocols approved by the University of California, San Francisco Institutional Animal Care and Use Program.

METHOD DETAILS

Behavior rig: To accurately evoke and measure OKR, we custom designed a behavior rig that was capable of presenting full-field, binocular stimuli to behaving mice. The design of the rig was based on Denman et al. [38]. Briefly, an acrylic hemisphere (diameter=24 inches, California Quality Plastics) was covered with a custom paint that had 50% diffuse reflectivity between 350 and 750 nm (Twilight Labs) in order to limit reflections within the hemisphere. Stimuli were emitted from a DLP projector with peak emission at 405 nm (LightCrafter through EKB Technologies) and were reflected onto the hemisphere via a silver-coated brass hemisphere ("convex mirror", diameter=6 inches, Wagner). Stimuli were built using Psychopy[93] (www.psychopy.org) and a custom wrapper to manage their sequential presentation and alignment with eye tracking videos. The wrapper and stimuli are both available at https://github.com/ScottHarris17/Bassoon. Aberrations in the projection were corrected by

applying a manually-fit spherical morph to all stimuli (Meshmapper, www.paulbourke.net). Blackout curtains surrounded the rig to minimize light contamination.

Unidirectional OKR stimuli: Unidirectional sinusoidal gratings were presented in groups of 6 consecutive epochs. Each epoch consisted of 20 seconds of a static grating, followed by 60 seconds of a grating drifting either directly upward or directly downward, and an additional 20 seconds of a static grating. The 6 total epochs consisted of 3 upward and 3 downward epochs that were randomly interleaved. All gratings moved at 10°/s and had a spatial frequency of 0.15 cycles/°. The brightest part of the grating evoked 1.38×10^3 S-cone photoisomerizations/s and the darkest part of the grating evoked 25.9 S-cone photoisomerizations/s. M-cone photoisomerizations were 60% those of S-cone.

Oscillating OKR stimuli: Oscillating sinusoidal gratings were presented in groups of 3 consecutive epochs. Each epoch consisted of 20 seconds of a static grating, followed by 120 seconds of oscillation, and an additional 20 seconds of a static grating. During the oscillation, the grating velocity was modulated sinusoidally up and down. The oscillation had an amplitude of 20°, a period of 15 seconds, and a phase shift of 0°. 8 oscillations were completed over the course of one epoch. All gratings had a spatial frequency of 0.15 cycles/°. The intensities of high contrast oscillating gratings were equivalent to those used for unidirectional OKR stimuli and had 5-fold greater Michelson contrast than low contrast oscillating gratings (i.e. low contrast gratings were "20% relative contrast"). High and low contrast gratings had the same mean luminance.

Eye tracking: Prior to eye tracking experiments, animals underwent stereotaxic surgery for implantation of a custom head-fixing apparatus. After surgery, animals were given 7 days to recover. Animals were then gradually habituated to the behavior rig by spending increasing amounts of time head-fixed on the rig for five consecutive days prior to the beginning of experiments.

Eye tracking experiments were run over the course of up to 3 days per animal. Each animal spent no more than 30 minutes per day on the rig. During experiments, mice were head-fixed in the center of the hemisphere, which filled the entirety of their visual field. Eye movements were recorded using a GigE camera (Photonfocus), an infrared filter, and a hot mirror (Edmund Optics) that allowed the camera to be positioned outside of the animal's field of view. Infrared LEDs (880 nm) were mounted on the top and side of the camera to generate corneal reflections that marked the meridian and equator of the eye, respectively. StreamPix software (NorPix) was used to capture video of the eye and align it to stimuli via TTL signals.

After completion of the experiments, Deeplabcut (www.deeplabcut.org) was used to train a neural network to locate the pupil and corneal reflection on each video frame. The two dimensional pupil location was then translated to angular eye position for every recording frame using the methods described by Stahl et al. [94,95] and Zoccolan et al. [96]. In short, prior to experiments, we calibrated the eye tracking system for each animal by repeatedly swinging the camera ±6° in the horizontal plane and measuring the relative position of the pupil and corneal reflection. This process was repeated across 5 different luminances to fit a linear regression between pupil size and angular eye position. The meridian and equator of the eye were measured by turning on the top- and side-aligned infrared LEDs in sequence. During experiments, only the top LED was on. Angular eye position was then calculated as $\phi = arcsin(\frac{\Delta x}{\sqrt{R_{p0}^2 - \Delta y^2}})$ [Eq. 1] and $\theta = arcsin(\frac{\Delta y}{R_{p0}})$ [Eq. 2], where ϕ is the horizontal eye position, θ is the vertical eye position, Δx is the horizontal distance measured between the eye center and the pupil, Δy is the vertical distance measured between the eye center and the pupil,

and R_{p0} is the radius of rotation between the pupil and the eye's center, which was computed empirically for each pupil diameter for each animal. For all stimuli, fast and slow nystagmus were separated on the basis of eye velocity and acceleration using custom MATLAB scripts. For all analyses in this report, we consider only θ, the vertical eye position, and $\Delta\theta/\Delta t$, the vertical component of eye velocity.

By measuring the vertical eye velocity ($\Delta\theta/\Delta t$) in response to the static gratings (multiple contrasts) that occurred before the onset of all stimuli, we also computed a baseline median eye drift of 0.0787°/s (IQR: 4.1792°/s; p=0.015) in the ventral direction across animals. This drift may reflect either the error associated with the estimation of the eye's center during our calibration process, or a natural biological eye drift associated with our rig. It is not possible to disambiguate between these possibilities. Since the eye position was near neutral for the time in which this drift was calculated, we baseline subtracted it from the eye position traces for all oscillating grating stimuli (for which the average eye position was also approximately neutral). For unidirectional gratings, we were unable to calculate an appropriate drift for baseline subtraction since the eye position was not often near neutral during these stimuli (**Fig 1 - figure supplement 2, Fig 8 - figure supplement 4**).

For oscillating OKR stimuli, saccades were removed from the eye trace post hoc. This was achieved by setting the eye velocity ($\Delta\theta/\Delta t$) during saccades to its value immediately prior to the saccade onset, and then reintegrating $\Delta\theta/\Delta t$ to compute the position of the eye across time.

Retrograde labeling: MTN-projecting retinal ganglion cells were labeled via stereotaxic injection of red fluorescent retrobeads (Lumafluor) into MTN. Prior to surgery, mice were anesthetized by IP injection of ketamine/xylazine and 5% isoflurane inhalation. Once fully anesthetized, as assessed by absence of the pedal reflex, animals were transferred to a sterile heated surface and the eyes were covered with a lubricating ointment. 2% isoflurane was administered continuously to maintain anesthesia. Fur was removed prior to incision and lidocaine (<7 mg/kg) was injected locally under the scalp. After incision, animals' heads were leveled by aligning bregma and lambda in the horizontal plane. A burr hole was drilled at A/P: 0.00 mm, M/L: 0.85 mm from bregma. All injections were performed into the right MTN. A glass needle filled with retrobeads (diluted 1:3 in di-water) and connected to a Hamilton syringe was lowered into the burr hole at an angle of 30° A/P to a depth of 5.36 mm below the surface of the brain. After 10 minutes, an injection of 400 nL was made at a rate of 5 nL/s. After injection, the needle was left in place for an additional 10 minutes before removal. The scalp was sutured and animals recovered in a heated cage. Analgesics [buprenorphine (0.05-0.1 mg/kg) and NSAIDs (5-10 mg/kg)] were delivered via subcutaneous injection immediately after animals awoke from anesthesia, again 12 hours later, and a third time the following morning. Animal health was monitored for three days after surgery and additional analgesics were administered as required. Labeling of retinal ganglion cells in the contralateral eye was typically observed as soon as 48 hours following surgery and did not increase with time.

Empirical mosaic analysis: All mosaic analyses occurred ≥2 days after injection of the retrograde tracer into MTN. Retinas were dissected, fixed in 4% PFA for 20 minutes, and flat-mounted onto a microscope slide with a spacer. One widefield fluorescent image was taken of each retina. The location of each labeled cell in the image was determined using custom MATLAB scripts. Only retinas with near complete labeling (determined as greater than 500 identified RGCs) were included in analyses. The retina perimeter, optic nerve head, and dorsal-ventral axis were manually measured. These points were used to define a normalized polar coordinate system that allowed for the comparison of cell locations and densities across retinas. Density recovery profiles were calculated using the methods described by Rodieck [97].

Mosaic models: To model spatial distributions of single and multiple mosaics, we randomly generated mosaics in a model circular retina that had an equivalent radius to that of the average whole-mount retina used for empirical density recovery profile estimation. "Cell bodies" were modeled as circles with radius 15 μm and scattered randomly across the model retina so long as the following conditions were met: (1) No two cell bodies can overlap in space (i.e., cells must form a 'monolayer'), and (2) Adjacent cells that are members of the same mosaic must obey a (noisy) exclusion zone that is set by the mosaic coverage factor (number of cells/retina area). Coverage factors were changed systematically such that the total number of cells across all mosaics - regardless of the number of mosaics being modeled - always approximated the number of retrogradely labeled cells per retina in our empirical data set. Density recovery profiles were computed as described for empirical data.

Electrophysiology tissue preparation: All electrophysiology experiments occurred ≥2 days after injection of the retrograde tracer into MTN. Prior to electrophysiology experiments, mice were dark-adapted for ≥12 hours. Mice were then euthanized by cervical dislocation and the left eye was enucleated (contralateral to the right MTN injection). Retina dissections occurred in the dark using infrared converters and warmed bicarbonate-based Ames solution, equilibrated with 95% O_2/5% CO_2. Brains were simultaneously harvested and fixed in 4% PFA for imaging and to confirm that the retrograde tracer was properly injected into MTN. Retinas were whole mounted, keeping track of orientation, and continuously perfused at 10 mL/min with freshly equilibrated Ames heated to 35 °C throughout the course of experiments.

Retinal location of recorded cells: At the beginning of electrophysiology experiments, the center and radius of the retina were measured: two-dimensional coordinates of 8 standardized points around the perimeter of the retina were noted. The center of the retina was estimated by computing the median of the circumcenters of all unique triangles that could be formed from these 8 points. The radius of the retina was estimated by finding the median radius of the circles that circumscribed these same triangles. In all cases, the convex hull of the whole-mount retina was well approximated by a circle and the retina center estimation was near the optic nerve head. The coordinates of each recorded cell were computed in reference to the retina center. Cell locations were combined across retinas by normalizing to the estimated radius in a polar coordinate system.

Identification of MTN-projecting RGCs: An NIR light source (950 nm, Sutter) was used to visualize the tissue for the majority of the experiment. To identify retrogradely-labeled ganglion cells, a green epifluorescent light was turned on briefly (~1-3 seconds) prior to recording from each cell. This light evoked a moderate number of spikes in oDSGCs. At least 1 minute of darkness was provided between the offset of the epifluorescent light and the beginning of subsequent experiments. The epifluorescence exposure likely contributed variance to our dataset by differentially modulating adaptation states along the dorsal/ventral retinal axis as the absorption spectra of cone photoreceptors change. However, for all electrophysiology experiments, care was taken to record from comparable spatial distributions of Superior and Inferior oDSGCs such that reported asymmetries between cell types cannot be attributed to uneven proportions of Superior and Inferior oDSGCs recorded from dorsal and ventral retina. Further, repeated exposures to epifluorescence throughout an experiment had no effect on oDSGC responsivity. Moreover, asymmetries between Superior and Inferior oDSGC tuning curves were observed within each retinal quadrant and between pairs of Superior and Inferior oDSGCs (within 30 µm of each other) across the retina (**Fig 2 - figure supplement 4**).

For a subset of cell-attached experiments, two-photon targeting was employed to validate and replicate our central findings. In these experiments, retrogradely-labeled retinal

ganglion cells were targeted on a two-photon microscope with peak emission at 860 nm and laser power approximately 17-40 mW. Two-photon and epifluorescence targeting were never performed on the same retina. Data collected during two-photon targeting are presented *only* in **Fig 2 - figure supplements 3, 5; Fig 7 - figure supplement 2; Fig 8E-G;** and **Fig 8 - figure supplement 2**. The figure legends also clearly indicate experiments in which two-photon targeting was used. Unless otherwise stated, electrophysiology data came from experiments in which epifluorescence was used.

Electrophysiology: Patch electrodes were pulled from borosilicate glass (Sutter) to 3-5 MOhm resistance using a Narishige puller. A MultiClamp 700B Amplifier (Axon Instruments) with acquisition rate of 10 kHz was used for all recordings. Cell-attached experiments were performed using electrodes filled with HEPES buffered Ames. Voltage-clamp experiments were performed using fresh electrodes filled with cesium methanesulfonate[98]. Current-clamp experiments were performed using fresh electrodes filled with potassium aspartate[99]. A subset of cells were recorded in both cell-attached and whole-cell configurations. In these cases, cell-attached recordings were performed first. Voltage-clamp and current-clamp recordings were never made from the same cell. Electrophysiology experiments were conducted using Symphony DAS (https://symphony-das.github.io/) and light stimuli were constructed and presented using Stage (https://stage-vss.github.io/).

Light increment stimulus: Light increments were the first stimulus to be presented, and were often additionally interleaved between other stimuli. Light increments were delivered for 1 second from darkness using an LED with peak emission at 405 nm. The increments had an intensity of 8.6×10^4 S-cone photoisomerizations/s. M-cone photoisomerizations were 79% of those of S-cone. The LED spot had diameter 500 μm or 300 μm (no significant difference was observed in the responses to either spot size), was centered on the cell body of each recorded cell, and was focused on the photoreceptor layer of the retina.

Drifting bar stimulus: Drifting bars were presented from a DLP projector with peak emission at 405 nm (LightCrafter through EKB Technologies, same model as used for behavioral experiments). The native optics of the projector were replaced with neutral density filters and optics to focus stimuli on the photoreceptor layer of the retina via a condenser. The projector covered a rectangular area of 427x311 μm which was centered on the soma of each recorded cell. Drifting bars had a width of 3.2° and moved at 10°/s using a conversion factor of 31 μm/°[100]. Bar height was limited only by the area covered by the projector. High contrast bars measured 2.4×10^4 S-Cone photoisomerizations/s and were presented on top of a background of 124 S-cone photoisomerizations/s [for drifting bar experiments utilizing two-photon targeting (**Fig 2 - figure supplements 3, 5; Fig 7 - figure supplement 2**) the background was 1.9×10^3 S-cone photoisomerizations/s]. M-cone photoisomerizations were 74% of those of S-cone. See below for the specifications of low contrast bars. For tuning curve estimation, bars moved in 8 directions separated by 45°. The presented sequence of stimulus directions was randomized for each recording. Tuning curves were estimated by mean measurements taken over 5 repetitions per stimulus direction.

Retinal ganglion cell classification: Retrogradely-labeled retinal ganglion cells were classified as either Superior or Inferior oDSGCs if they had a direction selectivity index of greater than 0.05 and a preferred direction more than 30° off of the temporal-nasal axis, as calculated by spike outputs measured in the cell-attached configuration. The vast majority of recorded cells met these criteria, but those that did not were excluded from further analyses (**Fig 2 - figure supplement 1**). All recorded cells in our data set were dominated by ON responses to a light increment (**Fig 3 - figure supplement 2**).

Current injections: Depolarizing or hyperpolarizing currents were continuously injected while measuring voltages across stimulus directions in the current-clamp configuration. The magnitude of current injections changed subtly from cell to cell depending on resting membrane potential, input resistance, and spike threshold. On average, depolarizing current injections increased the membrane potential by ~6 mV (to ~-48 mV), whereas hyperpolarizing current injections decreased the membrane potential by ~6 mV (to ~-60 mV). Depolarizing injections were always small enough such that the new resting membrane potential remained below spike threshold and each cell's baseline firing rate was 0 Hz. The order of depolarizing and hyperpolarizing injections was randomized across cells.

Isolation of spikes and subthreshold voltages: From current-clamp recordings, the onset and offset of each action potential were determined using the first and second derivatives of the voltage trace and a fixed minimum refractory period. The subthreshold voltage was then linearly interpolated between action potential onsets and offsets.

Subthreshold voltage tuning curves: The maximum voltage deflection from baseline was used to determine subthreshold membrane potential tuning curves. Values were averaged over 5 repetitions for each stimulus direction. Tuning curve metrics were calculated as for spikes.

Electrophysiology at low contrast: For experiments using epifluorescence targeting (i.e. all data in **Fig 7** and **Fig 7 - figure supplement 1**), low contrast drifting bars had an intensity of 0.5×10^4 S-cone photoisomerizations/s (~5-fold dimmer than high contrast bars, or "20% relative contrast") from the same background of 124 S-cone photoisomerizations/s. For experiments using two-photon targeting (i.e. **Fig 7 - figure supplement 2)**, low contrast bars had an intensity of 2.4×10^4 S-Cone photoisomerizations/s and were presented on top of a background of 1.3×10^4 S-Cone photoisomerizations/s. For both epifluorescence and two-photon targeting experiments, all other stimulus parameters were equivalent to what they were under high contrast conditions. In a subset of cells, low contrast bars failed to elicit spikes for every stimulus direction. In such cases, the cell's spike tuning curve area was set to 0, the area of its normalized tuning curve was set to 0, and its direction selectivity index was set to 1. We chose this convention because of the observation that, across cells, as the total number of spikes approached 0, the direction selectivity index approached 1 and the area of the normalized tuning curve approached 0. This pattern also fits the prediction made by our parallel conductance model (**Fig 7 - Figure Supplement 1F**). Cells with no responses under low contrast were classified as Superior or Inferior on the basis of their responses to high contrast stimuli.

Immunohistochemistry: Individual ganglion cells were filled with either Lucifer yellow or biocytin during electrophysiology experiments. Retinas were subsequently fixed in 2% paraformaldehyde for 20 minutes at room temperature. The following protocol was used to enhance for the cell fills [anti-Lucifer yellow (Life Technologies A5750) and/or streptavidin-488 (Thermo Fisher S11223)], label synaptic puncta [anti-postsynaptic density (PSD-95, UC Davis NeuroMab 75-028), anti-Gephyrin (Synaptic Systems 147 111)], and stain for cholinergic starburst amacrine cells [anti-choline acetyltransferase (ChAT, Millipore AB144P)]: blocking serum (1 day), primary antibody incubation (5 days), rinse 3x in PBS, secondary antibody (Jackson ImmunoResearch) incubation (1 day), rinse 3x in PBS. Retinas were mounted with a spacer in VECTASHIELD (Vector labs) and under a coverslip.

Imaging: Individual oDSGCs with known direction selectivity and their associated synaptic puncta were imaged on a confocal microscope (Leica SP8) using a 40x objective (NA 1.3) at a resolution of 0.102 x 0.102 x 0.3 μm.

Image analysis: Confocal images were first median filtered in 3 dimensions (Fiji). Ganglion cell dendrites were reconstructed using the filament function in Imaris (Oxford Instruments). Convex polygons, dendritic branch numbers, and total dendritic length were obtained from the filaments. Excitatory PSD-95 and inhibitory gephyrin puncta were identified and quantified within the filament mask of the ganglion cell dendrites (ObjectFinder, https://lucadellasantina.github.io/ObjectFinder/). Quantification of the puncta density from the center to periphery and along dendritic depth were also obtained in ObjectFinder.[102]

Electrical properties of oDSGCs: The resting membrane potential, spike threshold, and input resistance of oDSGCs were all measured during whole-cell current-clamp recordings. Resting membrane potential was taken as the initial membrane voltage immediately after establishing intracellular access. Spike threshold and input resistance were both calculated by injecting a slow ramp of current. Spike threshold was the average voltage at which a cell initiated its first action potential in response to the ramp. Input resistance was calculated from the average slope of the I-V response below spike threshold. Both metrics were averaged over at least 5 repetitions of the ramp stimulus per cell. The membrane capacitance was measured during voltage-clamp recordings using the built-in capacitance calculator from the MultiClamp 700B Amplifier (Axon Instruments).

Parallel conductance model: We implemented a parallel conductance model in MATLAB to build the model oDSGC (adopted from Antoine et al. [101]). Excitatory (Gex) and inhibitory (Gin) conductances were calculated at each time point for each direction of stimulus motion using Ohm's law: $G = I/(Vhold - Erev)$ [Eq. 3], where I was the mean current trace recorded in voltage-clamp across both Superior and Inferior cells, $Vhold$ was the holding potential, and $Erev$ was the reversal potential for either excitation or inhibition. A liquid junction potential of 5 mV was subtracted from $Vhold$ and $Erev$. Because our model called for directionally untuned excitation, but the recorded excitatory conductances were slightly different for each direction of stimulus motion (likely due in part to space-clamp error), we used an identical excitatory conductance for all directions of stimulus motion that was equal to the maximum conductance at each time point across all recorded directions (space-clamp errors reduce empirically recorded excitatory currents in voltage-clamp mode). The excitatory conductance was then multiplied by a gain value to achieve a final time series for Gex. Next, we used the equation

$C\frac{dV}{dt} = Gex(Eex - Vm) + Gin(Ein - Vm) + Grest(Erest - Vm)$ [Eq. 4]

to determine the membrane potential at each time point. C was the median capacitance of Superior and Inferior oDSGCs as measured during whole-cell recordings. $Grest$ was the reciprocal of the median input resistance, which we calculated by injecting a slow ramp of current in a subset of recorded cells and determining the average slope of the I-V response below spike threshold. $Erest$ was the median resting membrane potential. Vm was calculated at each point in time by initializing it at $Erest$, and then determining each subsequent value using Euler's method and an integration time step of 1 ms. The peak change in this Vm value above $Erest$ was used to construct the Vm tuning curves in the version of the model without a spiking component.

In the version of the model with a spiking component, we again solved for Vm at every time point using Euler's method. In this case, however, whenever Vm surpassed the threshold potential, a "spike" was counted and a 3 ms pause corresponding to the spike time and refractory period was initiated, after which Vm was reset to $Erest$ and the process continued. The threshold value was fixed such that the the normalized area and direction selectivity index of the model oDSGC's spike tuning curve matched the median empirical values for these metrics (taken from cell-attached recordings) when the excitatory gain was set to 1.0. This

resulted in a threshold value of -46.2 mV, which was 2.9 mV more negative than the median empirically recorded spike threshold.

Because resetting Vm to $Erest$ after each spike also changed the driving forces for excitation and inhibition - and therefore possibly the shape of resulting spike tuning curves - we also simulated spike responses by assuming that the number of spikes produced to a given stimulus was linearly proportional to the amount of time that Vm (calculated without a spiking mechanism in place) spent above spike threshold (data not shown). Results from this model were not substantively different than those from the model in which a refractory period was included and Vm was reset to $Erest$ after each spike.

This same model was used to test the contrast-dependence of spike and Vm tuning curves. In this case, both the excitatory and each of the 8 inhibitory conductance time series were multiplied by the gain value to calculate Gex and Gin, respectively.

Behavioral predictions from drifting bar stimulus: Predictions for OKR gain were calculated on the basis of the difference in median firing rates between Superior and Inferior oDSGC populations to the drifting bar stimulus. The preferred and null directions of each cell in our dataset were computed in response to high contrast drifting bars. Gain predictions were made for high and low (20% relative) contrast stimuli moving in the superior and inferior directions (i.e. four total conditions) by (1) resampling from distributions of oDSGC responses for that condition 10,000 times, (2) computing the difference (i.e., "delta") between the median preferred and null direction responses on each iteration for the appropriate cell types, and (3) using the median of these bootstrapped distributions of delta as an estimate of relative gain (**Fig 8 - figure supplement 1**). The amplitudes of the predicted eye movements shown in **Fig 8B** reflect these predictions, while the sinusoidal trajectories are inferred from the stimulus motion.

Computing the preferred and null direction of each cell has the advantage of controlling for the fact that the observed preferred direction of individual oDSGCs can change based on retinotopic location when the retina is flat mounted. Assigning the preferred direction to a constant stimulus direction across cells (e.g. dorsal-to-ventral motion on the retina for Superior oDSGCs) did not change the behavioral predictions (data not shown).

Behavioral predictions from oscillating grating stimulus: oDSGC responses were measured in the cell-attached configuration in response to the same oscillating grating stimulus used in behavioral experiments. Two-photon targeting was used for all oscillating grating electrophysiology experiments. Stimulus oscillations were sinusoidal and had a period of 15 seconds and an amplitude of 20°. The intensity of the grating was also sinusoidal across space, and had a spatial frequency of 0.15 cycles/°. For the high contrast stimulus, the mean light intensity of the grating evoked 3.8×10^3 S-cone photoisomerizations/s, the peak intensity evoked 7.6×10^3 S-cone photoisomerizations/s, and the trough intensity evoked 124 S-cone photoisomerizations/s. For the low contrast stimulus, the 20% relative (Michelson) contrast stimulus used in behavior experiments failed to evoke consistent spiking in oDSGCs. That 20% relative contrast gratings evoked OKR behavior but not oDSGC spikes can likely be explained by the fact that absolute contrasts and adaptation states were not matched between behavior and electrophysiology. However, assuming monotonic nonlinearities, it is only necessary to match the *direction* (e.g. higher to lower) of contrast change to predict the corresponding *direction* of behavioral change across contrasts. Thus, in electrophysiology experiments, we used a version of the low contrast oscillating grating stimulus that was 50% relative contrast compared to the high contrast stimulus described above. The mean light intensity of this stimulus evoked 3.8×10^3 S-cone photoisomerizations/s, the peak intensity evoked 5.7×10^3 S-cone photoisomerizations/s, and the trough intensity evoked 1.9×10^3 S-cone photoisomerizations/s. For all stimuli, M-cone photoisomerizations were 74% those of S-cones. The initial positional phase of the grating was randomized between cells.

Linear behavioral predictions were made from the spike responses of Superior and Inferior oDSGCs to these oscillating stimuli (**Fig 8 - figure supplement 2**). The following procedure was repeated separately for responses to high and low contrast gratings: first, the median spike rate of Superior and Inferior oDSGCs was computed every 5 ms over the course of a single 15 second oscillation cycle (**Fig 8 - figure supplement 2C-D**). A point-by-point subtraction was then performed (**Fig 8 - figure supplement 2E-F**). The difference between the median spike rates of Superior and Inferior oDSGCs served as a linear prediction of eye velocity at each point in time. Therefore, predictions of eye position were computed across time by integrating these differences: $p(t) = \int(Sup. - Inf.)dt$ [Eq. 5], where $p(t)$ is the vertical position of the eye at time t. The starting position of the eye was set to 0° (**Fig 8 - figure supplement 2G-H**).

Empirical Nonlinearity: The relationship between linear predictions of OKR and measured eye velocities was estimated by finding the least squares fit of a sigmoid function of the form $v(r) = \frac{(v_{min} - v_{max})}{(1+10^{(r_{50}-r)m})}$ [Eq. 6], where v_{min} is the minimum eye velocity, v_{max} is the maximum eye velocity, r_{50} is the firing rate along the azimuth that corresponds to the inflection point, m controls the slope, and $v(r)$ is the expected eye velocity for a given firing rate, r. For the drifting bar stimulus (**Fig 8D**), the linear predictions and behavioral eye velocities for superior and inferior stimuli at high and low contrast, along with a fifth point at the origin (0, 0), were used to fit the curve. For the oscillating grating stimulus (**Fig 8G**), the high contrast instantaneous linear predictions and the time-matched average eye velocities during high contrast stimuli were used to fit the curve. Fit parameters for both curves are reported in the legend of **Fig 8**.

QUANTIFICATION AND STATISTICAL ANALYSIS

Statistics: All metrics reported in the text refer to population mean±SEM unless otherwise specified. Nonparametric hypothesis tests were used to compute significance values wherever possible. Mann-Whitney U tests were used for instances in which the test type is not specified. Wilcoxon signed-rank and Fisher's exact tests were used where specified in the text and/or figure legends. All tests were two-sided. R values are Spearman's rank correlation coefficients. Lines of best fits are least squares linear regressions. Significance markings are as follows: not significant (N.S.), p≥0.05, *p<0.05, **p<0.01, ***p<0.001. All values can be found in the figures, figure legends, and Results section. All statistical analyses were performed in MATLAB.

Tuning curve area: Tuning curve area was calculated by dividing the area under the curve of the linear tuning curve by 360°. For clarity, this metric is also referred to as the "linear tuning curve area."

Preferred direction: The preferred direction was calculated as the direction of the vector sum of spike responses to all 8 stimulus directions. Thus, the preferred direction was not necessarily equivalent to the single stimulus direction that evoked the largest response. The null direction was defined as 180° away from the preferred direction.

Normalized tuning curves: Normalized tuning curves were calculated by first determining the cell's preferred direction (see above), and then dividing the response in all 8 stimulus directions to the response in that preferred direction. For cases in which the preferred direction did not match a stimulus direction that was specifically probed, the preferred direction response was estimated by a linear interpolation of the two neighboring probed directions. The area of the normalized tuning curve (abbreviated as the "normalized area") was calculated by dividing the

area under the curve of the linear normalized tuning curve by 360°. The area of the normalized tuning curve is always greater than 0, but has no upper bound - though it tended to fall below 1. Larger values indicate a wider tuning curve. Perfectly circular tuning curves take a value of 1.

Direction selectivity index: The direction selectivity index (DSI) was calculated as the magnitude of the vector sum divided by the scalar sum of responses to all 8 stimulus directions. The direction selectivity index ranges between 0 and 1, with larger values indicating sharper tuning curves.

Von Mises fit: Tuning curves were fit to the Von Mises function by minimizing the sum of squared residuals. The Von Mises function is a circular analog of the Gaussian curve defined as $f(x) = \frac{e^{\kappa cos(x-\mu)}}{2\pi I_0(\kappa)}$ [Eq. 7], where μ is the center of the curve, $1/\kappa$ controls the width of the curve, and I_0 is the modified Bessel function of the first kind, of order 0. A larger κ value indicates a sharper fit.

RESOURCES TABLE

REAGENT or RESOURCE	SOURCE	IDENTIFIER
Antibodies		
Rabbit polyclonal anti-Lucifer yellow	Invitrogen	Cat #A5750: RRID:AB_1501344
Mouse monoclonal anti-gephyrin	Synaptic System	Cat# 147 111: RRID: AB_887719
PSD-95 MAGUK scaffolding protein	Neuromab	Cat# 75-028; RRID:AB_2292909
Anti-choline acetyltransferase	Millipore	Cat# AB144P: RRID:AB_2079751
Donkey polyclonal anti-mouse-Dylight 405	Jackson Immunoresearch	Cat# 715-475-150; RRID:AB_2340839
Donkey polyclonal anti-mouse-Alexa 647	Jackson Immunoresearch	Cat# 715-605-151; RRID:AB_2340863
Goat anti-mouse IgG, Fc_Subclass 1 Specific-Dylight 405	Jackson Immunoresearch	Cat# 115-475-205; RRID:AB_2338799
Goat anti-mouse IgG, Fc_Subclass 2a Specific-Alexa 647	Jackson Immunoresearch	Cat# 115-605-206; RRID:AB_2338917
Donkey polyclonal anti-rabbit-Alexa 488	Jackson Immunoresearch	Cat# 711-545-152; RRID:AB_2313584
Donkey anti-goat IgG (H+L)-Alexa 647	Jackson Immunoresearch	Cat# 705-605-147; RRID:AB_2340437
Streptavidin 488	Molecular Probes	Cat# S32354; RRID: AB_2315383
Chemicals, Peptides, and Recombinant Proteins		
Normal Donkey Serum	Jackson Immunoresearch	Cat# NC9624464

Ames' Medium	United States Biological	Cat# A1372-25
Vectashield	Vector Laboratories	Cat# H-1000; RRID: AB_2336789
Red Retrobeads	Lumafluor	https://lumafluor.com/information
Lucifer yellow CH dilithium salt	Sigma	Cat# L0259
Biocytin	Invitrogen	Cat# B1592
Experimental Models: Organisms/Strains		
WT C57BL/6J Mice	The Jackson Laboratory	N/A
Software and Algorithms		
Amira	Thermo-Fisher Scientific	https://www.fei.com/software/amira-avizo/, RRID: SCR_014305
Bassoon	Scott Harris	https://github.com/ScottHarris17/Bassoon https://doi.org/10.5281/zenodo.6757605
Igor Pro	Igor Pro	RRID:SCR_000325
ImageJ	NIH	https://imagej.nih.gov/ij/ RRID: SCR_003070
Imaris	Bitplane	http://www.bitplane.com/ RRID: SCR_007370
MATLAB	Mathworks	https://www.mathworks.com/products/matlab.html RRID: SCR_001622
Meshmapper	Paul Bourke	http://paulbourke.net/dome/meshmapper/
Object Finder	Della Santina et al., 2013[102]	https://github.com/lucadellasantina/ObjectFinder http://doi.org/10.5281/zenodo.4767847
Psychopy	Open Science Tools Ltd.[93]	https://psychopy.org/about/index.html
ScanImage	MBF Bioscience	https://www.mbfbioscience.com/products/scanimage
StreamPix	NorPix	https://www.norpix.com/products/streampix/streampix.php

Symphony and Stage	Mark Cafaro and Fred Rieke	https://github.com/Symphony-DAS/symphony-matlab https://github.com/Stage-VSS/stage-v1
VolumeCut	Della Santina et al., 2021[103]	https://github.com/lucadellasantina/VolumeCut http://doi.org/105281/zenodo.5048331

SUPPLEMENTAL MATERIAL

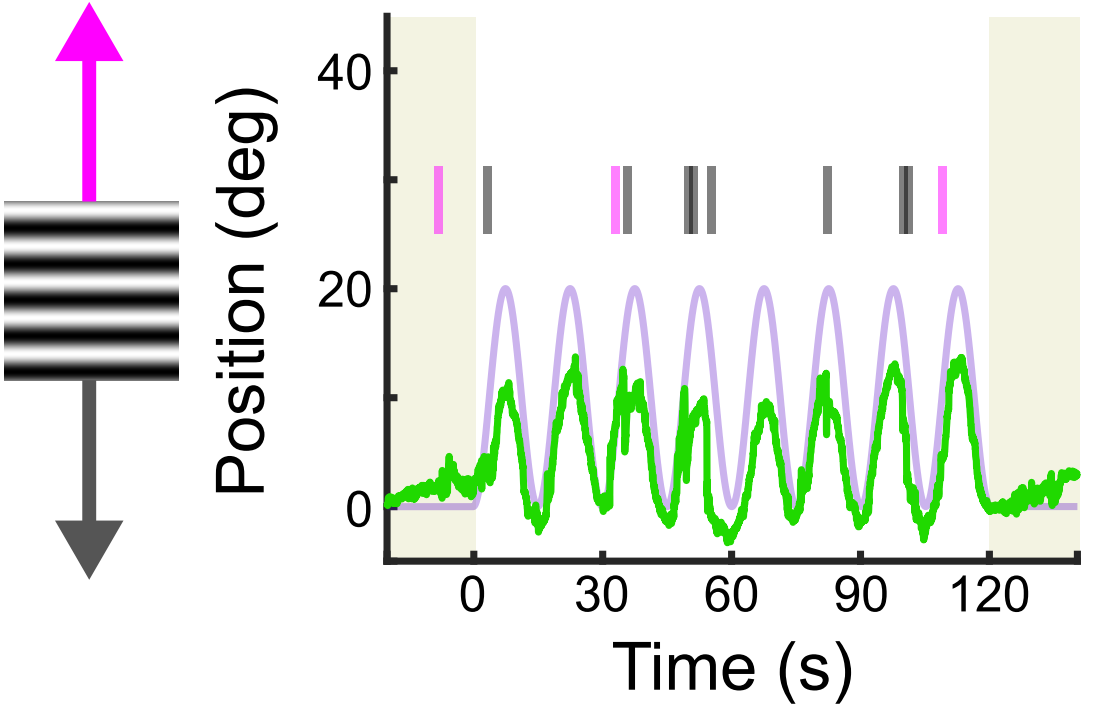

Figure 1 S1

Figure 1 - figure supplement 1. Example of sinusoidal vertical OKR before saccade removal. Eye position (green) is plotted across time as a full-field, black and white grating oscillates vertically (lavender). The eye trace includes saccades (i.e., “fast nystagmuses,” as indicated by tick marks: magenta for superior, gray for inferior). Saccades tend to occur in the opposite direction as the "slow nystagmus" and do not facilitate image stabilization, however saccades are necessary to keep the eye centered in its orbit. Removing these resetting saccades from the eye trace isolates the slow nystagmus component and reveals the asymmetry between Superior and Inferior OKR (Fig 1G).

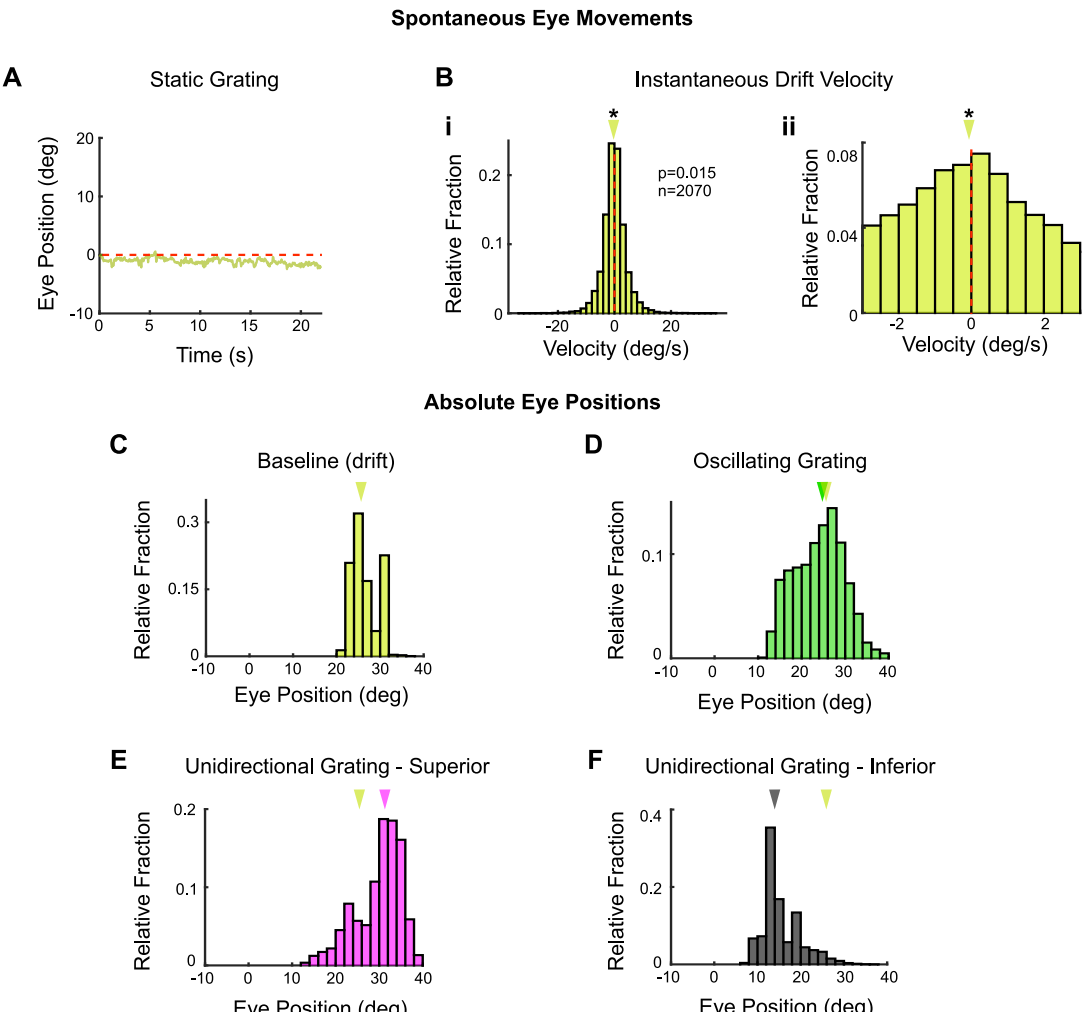
Spontaneous Eye Movements
A
Static Grating
Eye Position (deg)
Time (s)
B
Instantaneous Drift Velocity
i
p=0.015
n=2070
Relative Fraction
Velocity (deg/s)
ii
Relative Fraction
Velocity (deg/s)
Absolute Eye Positions
C
Baseline (drift)
Relative Fraction
Eye Position (deg)
D
Oscillating Grating
Relative Fraction
Eye Position (deg)
E
Unidirectional Grating - Superior
Relative Fraction
Eye Position (deg)
F
Unidirectional Grating - Inferior
Relative Fraction
Eye Position (deg)

Figure 1 S2

Figure 1- figures supplement 2. Baseline vertical eye movements in headfixed mice (see also Fig 8 - figure supplement 4). Vertical eye movements were measured in response to static gratings to calculate eye drifts for baseline subtraction. **(A)** Example raw eye trace over 22 seconds of a static grating. The calculated position of the eye drifts downward over time, which could reflect true eye movements or a calibration error in our recording configuration. These two possibilities cannot be disambiguated (see Methods). The magnitude of eye position drift during static gratings is approximately 18-fold less than the magnitude of the eye movements elicited by drifting gratings. **(B)** Distribution of instantaneous eye velocity across N=5 animals for the 20 seconds prior to the onset of all drifting grating stimuli [unidirectional and oscillating gratings at high (full) and low (20% relative) contrasts] used to evoke OKR. On average, there is a slight bias toward inferior (i.e. downward/negative) eye velocities during this baseline period, with a median velocity of -0.0787°/s. **(Bi)** Full distribution. **(Bii)** Same data, zoomed in on 0° to reveal the inferior bias. **(C-F)** Absolute vertical position of the eye without drift correction **(C)** prior to stimulus onset [when the drift was calculated as in (B), includes data from high (full) and low (20% relative) contrast, oscillating and unidirectional experiments], and during (D) high contrast oscillating gratings, **(E)** superior unidirectional gratings and **(F)** inferior unidirectional gratings. Absolute eye position is similar to that measured during baseline only for oscillating gratings. The eye moves to more extreme positions during unidirectional stimuli. For this reason, the baseline subtraction was only applied to eye movements measured in response to oscillating gratings. For all histograms, arrows mark the median of the distribution. Yellow arrow in (D-F) marks the median of the distribution shown in (C). See Fig 8 - figure supplement 2 for further data on eye drift in response to low contrast gratings. *$p<0.05$, **$p<0.01$, ***$p<0.001$

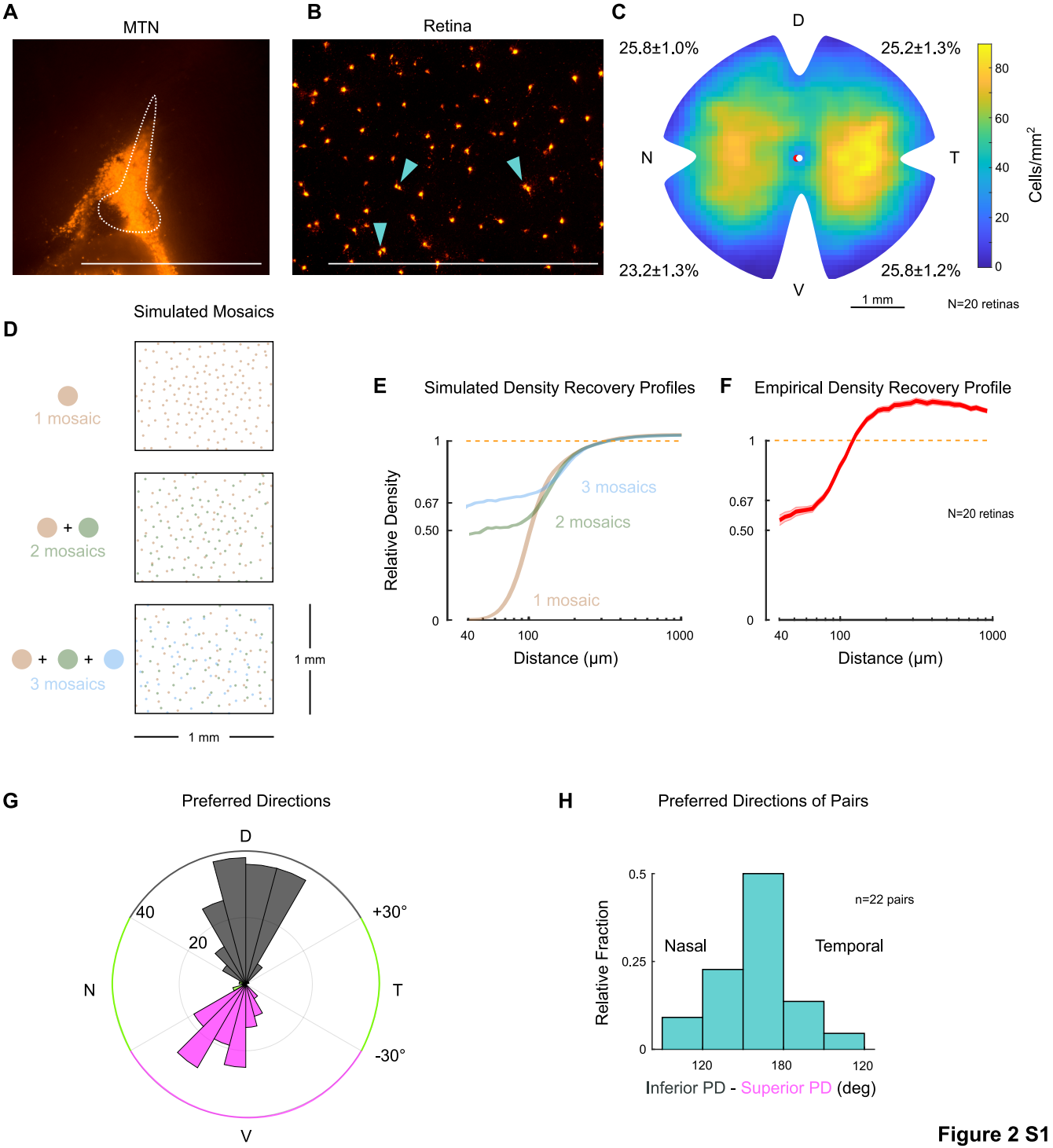
A
MTN
B
Retina
C
D
25.8±1.0%
25.2±1.3%
N
T
23.2±1.3%
25.8±1.2%
V
1 mm
N=20 retinas
Cells/mm2
80
60
40
20
0
D
Simulated Mosaics
1 mosaic
2 mosaics
3 mosaics
1 mm
1 mm
E
Simulated Density Recovery Profiles
Relative Density
1
0.67
0.50
0
3 mosaics
2 mosaics
1 mosaic
40
100
1000
Distance (μm)
F
Empirical Density Recovery Profile
1
0.67
0.50
0
N=20 retinas
40
100
1000
Distance (μm)
G
Preferred Directions
D
40
20
+30°
N
T
-30°
V
H
Preferred Directions of Pairs
Relative Fraction
0.5
0.25
0
n=22 pairs
Nasal
Temporal
120
180
120
Inferior PD - Superior PD (deg)

Figure 2 S1

Figure 2 - figure supplement 1. Two retinal ganglion cell types project to the medial terminal nucleus. (A) Sagittal section of medial terminal nucleus (MTN) following injection of fluorescent retrobeads (scale bar=1 mm). Dotted line outlines MTN. **(B)** Retrogradely labeled ganglion cell somas in a flat-mount retina after contralateral MTN injection. Arrowheads point to examples where labeled cells form "pairs" (i.e., are within 30 µm of each other; scale bar=1 mm), as described previously[20]. **(C)** Density heatmap of retrogradely-labeled ganglion cells across the contralateral retina. Numbers around the perimeter indicate percentage of cells found in each quadrant (mean±SEM). D, T, V, and N denote dorsal, temporal, ventral, and nasal directions, respectively, on the retina. Pairwise comparisons of the average number of cells per quadrant did not reveal any significant differences. However, comparing across halves showed that densities were marginally greater in dorsal compared to ventral retina (p=0.047), and in temporal compared to nasal retina (p=0.021). **(D)** Simulations of ganglion cell populations that consist of one (top), two (middle) and three (bottom) mosaics. Each simulation contains approximately the same number of total cells. When only one mosaic is present (top), cells obey exclusion zones and do not cluster next to each other. When more than one mosaic is present, cells do not respect the exclusion zones of other cell types and "pairs" (middle) and "trios" (bottom) begin to form. Ganglion cells of distinct types are well known to tile the retina in separate mosaics. **(E)** Mean density recovery profiles (DRPs) for simulated ganglion cell populations of one (tan), two (green), and three (blue) mosaics (n=30 repetitions each). Only single mosaics exhibit a complete exclusion zone. The DRP of two mosaics converges to 50% of its average density (dashed line) as distance approaches 0, and the DRP of three mosaics converges to 67% of its average density. More generally, a spatial distribution of ganglion cells will converge to $\frac{n-1}{n} \times 100\%$ of its average density, where n is the total number of mosaics[72]. **(F)** DRP measured from retrogradely labeled MTN-projecting ganglion cells (mean±SEM). The empirical DRP lacks a full exclusion zone and converges to ~50% of its average density (1.0), indicating that there are likely two ganglion cell types, each forming an independent mosaic. Note that the DRP overshoots 1.0 within the shown domain because oDSGCs are not uniformly distributed across the retina [as shown in (C)]. Normalizing to the peak density yields similar results. **(G)** Polar histogram of preferred directions measured in cell-attached mode across retrogradely labeled ganglion cells identified by epifluorescence targeting. Colored segments of the outer circle indicate preferred direction thresholds for classification of Superior (magenta), Inferior (gray), and other ganglion cells (green). Concentric circles indicate the number of cells per bin. Labeled ganglion cells divide into two major physiological types: superior-preferring and inferior-preferring. Only a small fraction of cells prefer horizontal directions (green). **(H)**

Preferred directions of cells found in pairs (somas within 30 μm of each other). Paired cells tend to prefer opposite directions of motion (180° apart), further indicating that (1) two separate populations of ganglion cells project to MTN and (2) each population forms an independent mosaic.

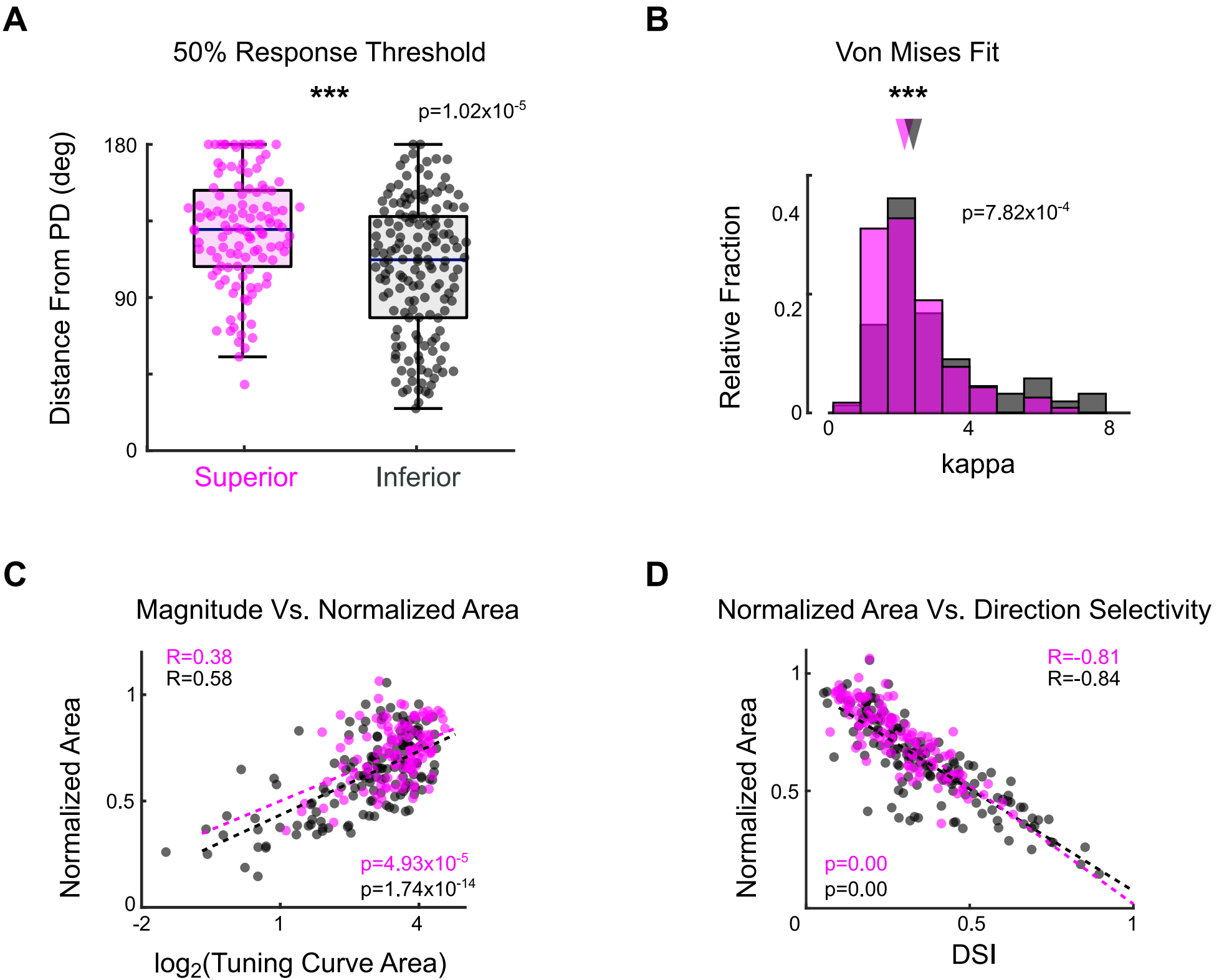
A
50% Response Threshold
***
p=1.02x10^-5
Distance From PD (deg)
180
90
0
Superior
Inferior
B
Von Mises Fit
***
p=7.82x10^-4
Relative Fraction
0.4
0.2
0
0
4
8
kappa
C
Magnitude Vs. Normalized Area
R=0.38
R=0.58
Normalized Area
1
0.5
0
-2
1
4
p=4.93x10^-5
p=1.74x10^-14
log2(Tuning Curve Area)
D
Normalized Area Vs. Direction Selectivity
R=-0.81
R=-0.84
Normalized Area
1
0.5
0
0
0.5
1
p=0.00
p=0.00
DSI

Figure 2 S2

Figure 2 - figure supplement 2. Additional metrics of oDSGC spike tuning curve width. (A) Distributions of the distance (in degrees) from each cell's preferred direction to the point at which its response magnitude first drops below 50% of the response in the preferred direction. Larger values indicate a wider tuning curve. Horizontal line represents median, box boundaries are the IQR, whiskers represent most extreme observation within 1.5xIQR. Points represent individual cells. **(B)** Histograms of the kappa parameter for the Von Mises fit of the tuning curve of each cell (see Methods). A smaller kappa value indicates a wider tuning curve. **(C)** The area of the linear tuning curve and the area of the normalized tuning curve were positively correlated on a cell-by-cell basis. **(D)** The direction selectivity index and the area of the normalized tuning curve were negatively correlated on a cell-by-cell basis. Dashed lines in C and D are least-squares linear regressions for Superior (magenta) and Inferior (gray) oDSGCs. R and p values for scatter plots are the Spearman's rank correlation coefficient and associated significance, respectively. *$p<0.05$, **$p<0.01$, ***$p<0.001$.

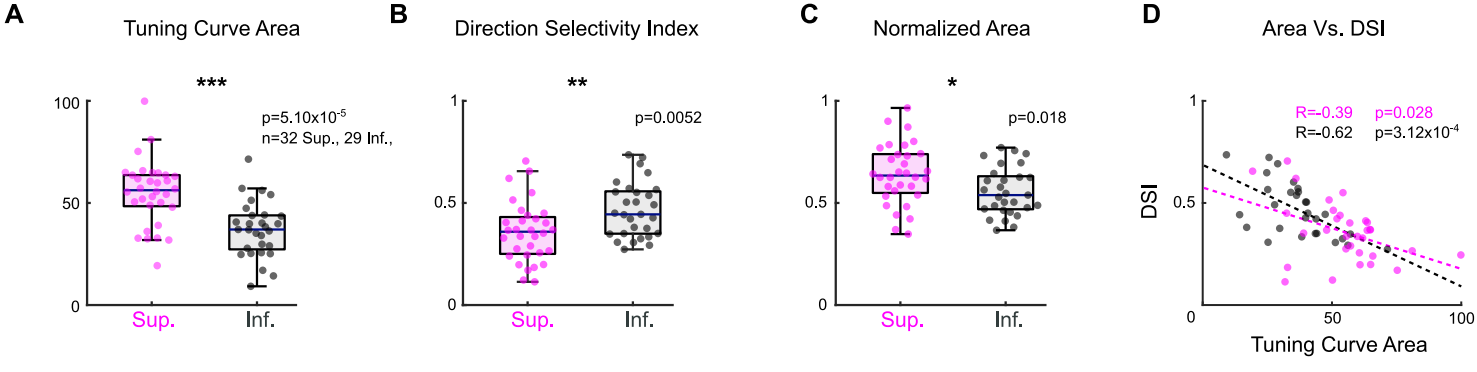
A
Tuning Curve Area
***
p=5.10x10^-5
n=32 Sup., 29 Inf.,
100
50
0
Sup.
Inf.
B
Direction Selectivity Index
**
p=0.0052
1
0.5
0
Sup.
Inf.
C
Normalized Area
*
p=0.018
1
0.5
0
Sup.
Inf.
D
Area Vs. DSI
R=-0.39 p=0.028
R=-0.62 p=3.12x10^-4
DSI
1
0.5
0
50
100
Tuning Curve Area

Figure 2 S3

Figure 2 - figure supplement 3. Asymmetries between Superior and Inferior oDSGCs persist under two-photon targeting. Retrogradely labeled oDSGCs were targeted for cell-attached recordings using a two-photon laser (860 nm). Spikes were measured from Superior and Inferior oDSGCs in response to the drifting bar stimulus. Under two-photon conditions, Superior oDSGCs had **(A)** greater area of the linear tuning curve, **(B)** lower direction selectivity, and **(C)** greater area of the normalized tuning curve compared to Inferior oDSGCs. **(D)** Direction selectivity and tuning curve area were significantly correlated on a cell-by-cell basis for both Superior and Inferior oDSGCs. Dashed lines are least-squares linear regressions for Superior (magenta) and Inferior (gray) oDSGCs. R and p values for scatter plots are the Spearman's rank correlation coefficient and associated significance, respectively. These findings confirm the results from experiments in which ganglion cells were targeted by epifluorescence (Fig 2, Fig 2 - figure supplement 2). Cells in this two-photon dataset come from tissue that was never exposed to epifluorescence. No cell is in both the epifluorescence and two-photon datasets. *$p<0.05$, **$p<0.01$, ***$p<0.001$.

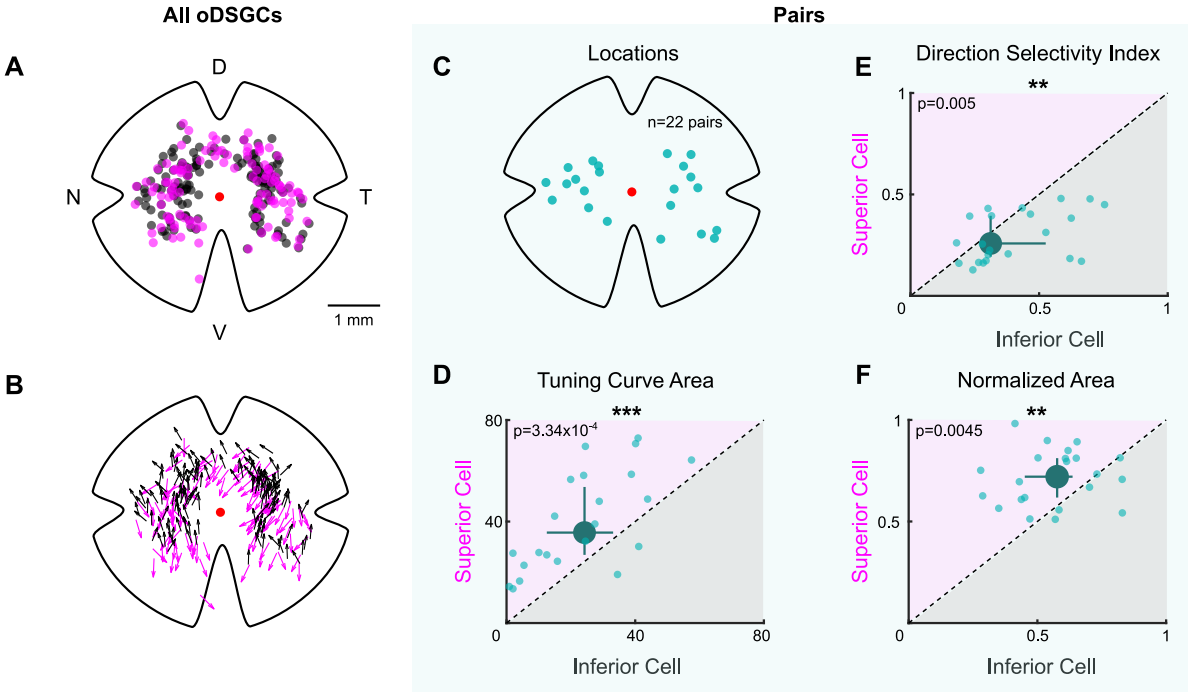
All oDSGCs
Pairs
A
D
N
T
V
1 mm
B
C
Locations
n=22 pairs
E
Direction Selectivity Index
**
p=0.005
Superior Cell
Inferior Cell
D
Tuning Curve Area
***
p=3.34x10-4
F
Normalized Area
**
p=0.0045

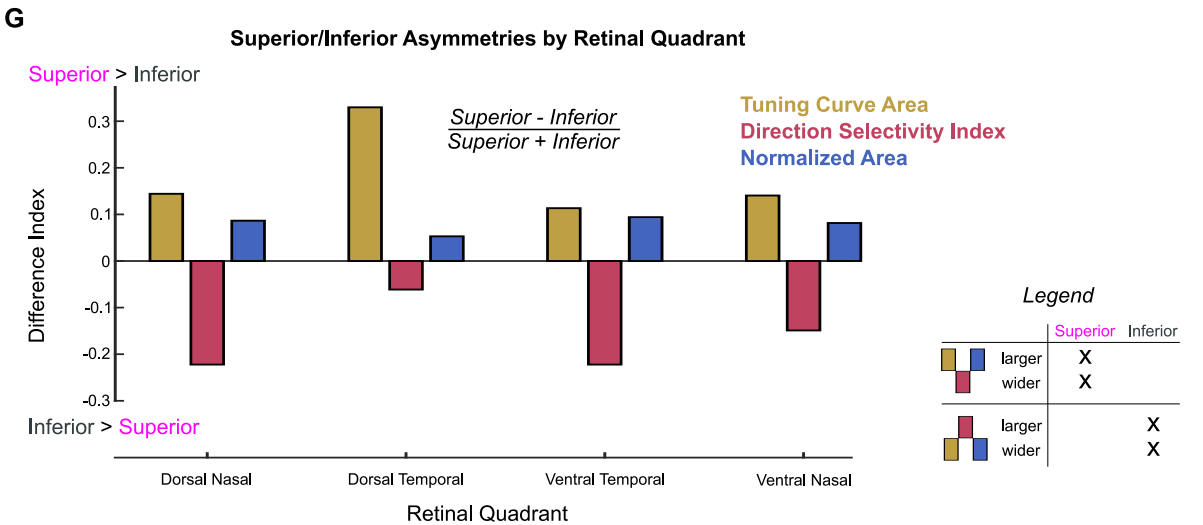
G
Superior/Inferior Asymmetries by Retinal Quadrant
Superior > Inferior
Inferior > Superior
Difference Index
Superior - Inferior
Superior + Inferior
Tuning Curve Area
Direction Selectivity Index
Normalized Area
Dorsal Nasal
Dorsal Temporal
Ventral Temporal
Ventral Nasal
Retinal Quadrant
Legend
Superior
Inferior
larger
wider
larger
wider

Figure 2 S4

Figure 2 - figure supplement 4. Physiological differences between Superior and Inferior oDSGCs are consistent across retinal topography. (A) Map of retinal locations of all MTN-projecting ganglion cells recorded during cell-attached experiments in which epifluorescence targeting was used. D, T, V, and N denote dorsal, temporal, ventral, and nasal directions, respectively, on the retina and apply to all maps. **(B)** Map of the preferred direction of each cell in (A). The arrow base marks the location of the cell soma. The arrowhead points in the preferred direction. Preferred directions varied systematically across the retina, as reported previously[16]. **(C-F)** Data from Superior and Inferior oDSGCs that formed "pairs" (i.e., somas within 30 µm of each other, see Fig 2 - figure supplement 1). Pairwise comparisons in these cells remove potential confounds caused by differences in topographic distributions when looking for asymmetries across Superior and Inferior oDSGC populations. **(C)** Retinal location of each recorded pair. **(D-F)** Tuning curve metrics for the Superior and Inferior oDSGCs in each pair: **(D)** linear tuning curve area, **(E)** direction selectivity index, and **(F)** area of the normalized tuning curve. Dashed lines indicate unity. Large points represent the univariate medians. Whiskers are 95% confidence intervals for each median, determined via bootstrapping. Significance values indicate pairwise comparisons between Superior and Inferior oDSGCs (2-sided signed-rank). Superior oDSGCs spike more **(D)**, are less direction selective **(E)**, and have wider tuning curves **(F)** when compared to the Inferior oDSGCs with which they form pairs. **(G)** Comparison of tuning curve metrics between Superior and Inferior oDSGCs found in each retinal quadrant. Bars show a difference index [(Superior - Inferior)/(Superior + Inferior)] calculated from the median linear tuning curve area (olive), direction selectivity index (red), or area of the normalized tuning curve (blue) per quadrant for each oDSGC type. Positive values indicate that the metric is greater for Superior cells in that quadrant and negative values indicate that the metric is greater for Inferior cells in that quadrant. Difference indices are bound between -1 and 1. Within each retinal quadrant, Superior oDSGCs have a larger linear tuning curve area, a lower direction selectivity index, and a larger normalized tuning curve area than Inferior oDSGCs. Data match the first possibility illustrated in the legend. *$p<0.05$, **$p<0.01$, ***$p<0.001$

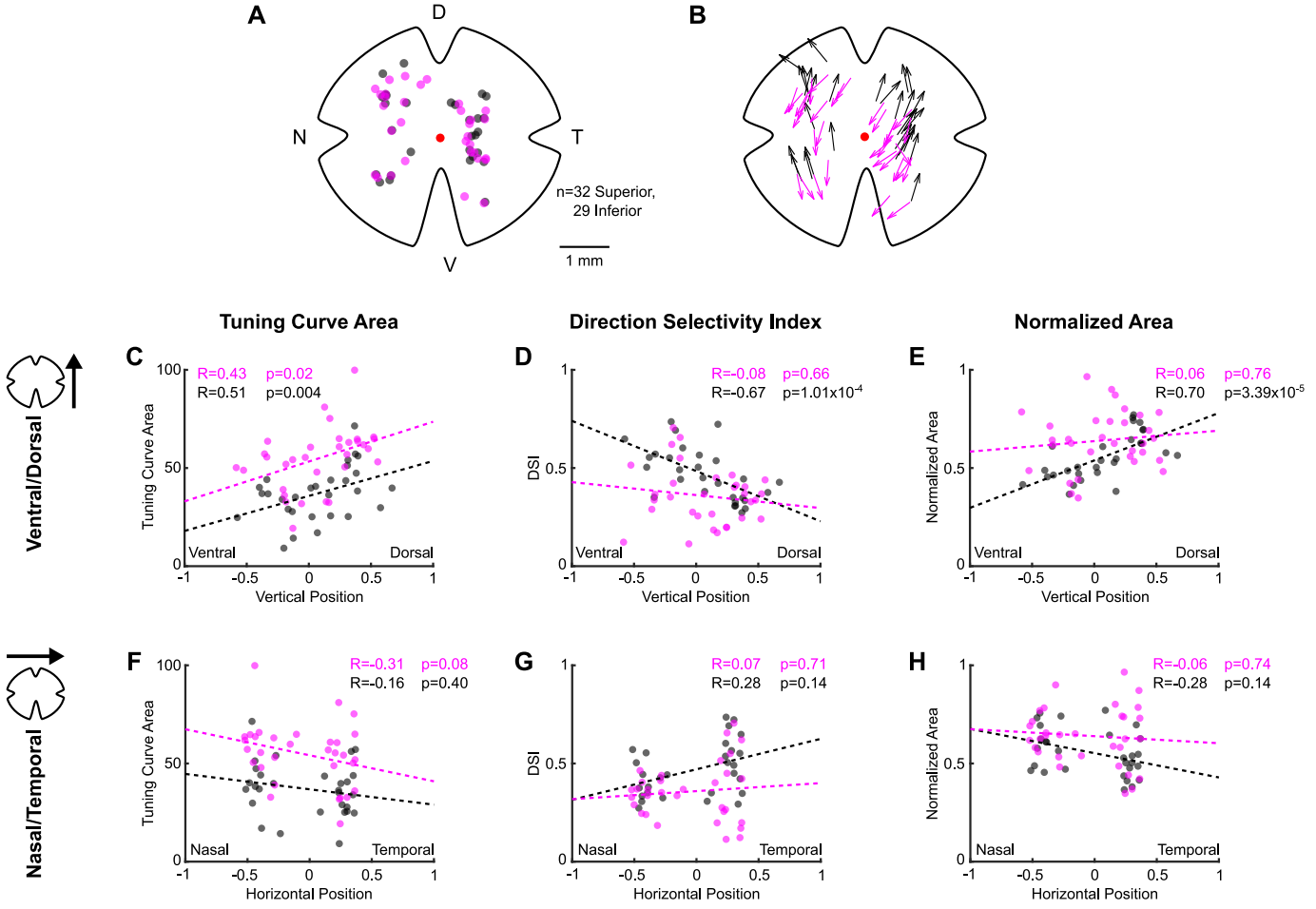
A
D
N
T
V
n=32 Superior,
29 Inferior
1 mm
B
Tuning Curve Area
Direction Selectivity Index
Normalized Area
Ventral/Dorsal
Nasal/Temporal
C
R=0.43 p=0.02
R=0.51 p=0.004
Tuning Curve Area
Ventral
Dorsal
Vertical Position
D
R=-0.08 p=0.66
R=-0.67 p=1.01x10-4
DSI
Ventral
Dorsal
Vertical Position
E
R=0.06 p=0.76
R=0.70 p=3.39x10-5
Normalized Area
Ventral
Dorsal
Vertical Position
F
R=-0.31 p=0.08
R=-0.16 p=0.40
Tuning Curve Area
Nasal
Temporal
Horizontal Position
G
R=0.07 p=0.71
R=0.28 p=0.14
DSI
Nasal
Temporal
Horizontal Position
H
R=-0.06 p=0.74
R=-0.28 p=0.14
Normalized Area
Nasal
Temporal
Horizontal Position

Figure 2 S5

Figure 2 - figure supplement 5. Topographic variation in direction tuning properties across the retina revealed by two-photon targeting. (A) Map of retinal locations of all MTN-projecting ganglion cells recorded during cell-attached experiments in which two-photon targeting was used. D, T, V, and N denote dorsal, temporal, ventral, and nasal directions, respectively, on the retina and apply to all maps. **(B)** Map of the preferred direction of each cell in (A). The arrow base marks the location of the cell soma. The arrowhead points in the preferred direction. Preferred directions varied systematically across the retina, as seen using epifluorescence targeting (Fig 2 - figure supplement 4) and as reported previously[16]. **(C-H)** Scatter plots of tuning curve metrics as a function of each cell's position along either the ventral-dorsal **(C-E)** or nasal-temporal **(F-H)** axis of the retina. Coordinates are normalized to the size of the retina from which each cell was recorded (normalized coordinates range between -1 and 1, see Methods). Inferior oDSGCs change tuning curve size (C) and width (D, E) as a function of dorsal-ventral location, whereas only the tuning curve size (C) of Superior oDSGCs is modulated along the same axis. No metric is significantly related to position along the nasal-temporal axis for either cell type (F-H). Further, Superior oDSGCs tend to have larger and wider tuning curves than Inferior oDSGCs across all dimensions (separation between magenta and gray lines). For all scatter plots, dashed lines are least-squares linear regressions for Superior (magenta) and Inferior (gray) oDSGCs. R and p values are the Spearman's rank correlation coefficient and associated two-tailed significance, respectively. Two-photon targeting was used for this experiment so as to avoid confounds associated with epifluorescence exposure and photoreceptor absorption spectra gradients across retinal topography.

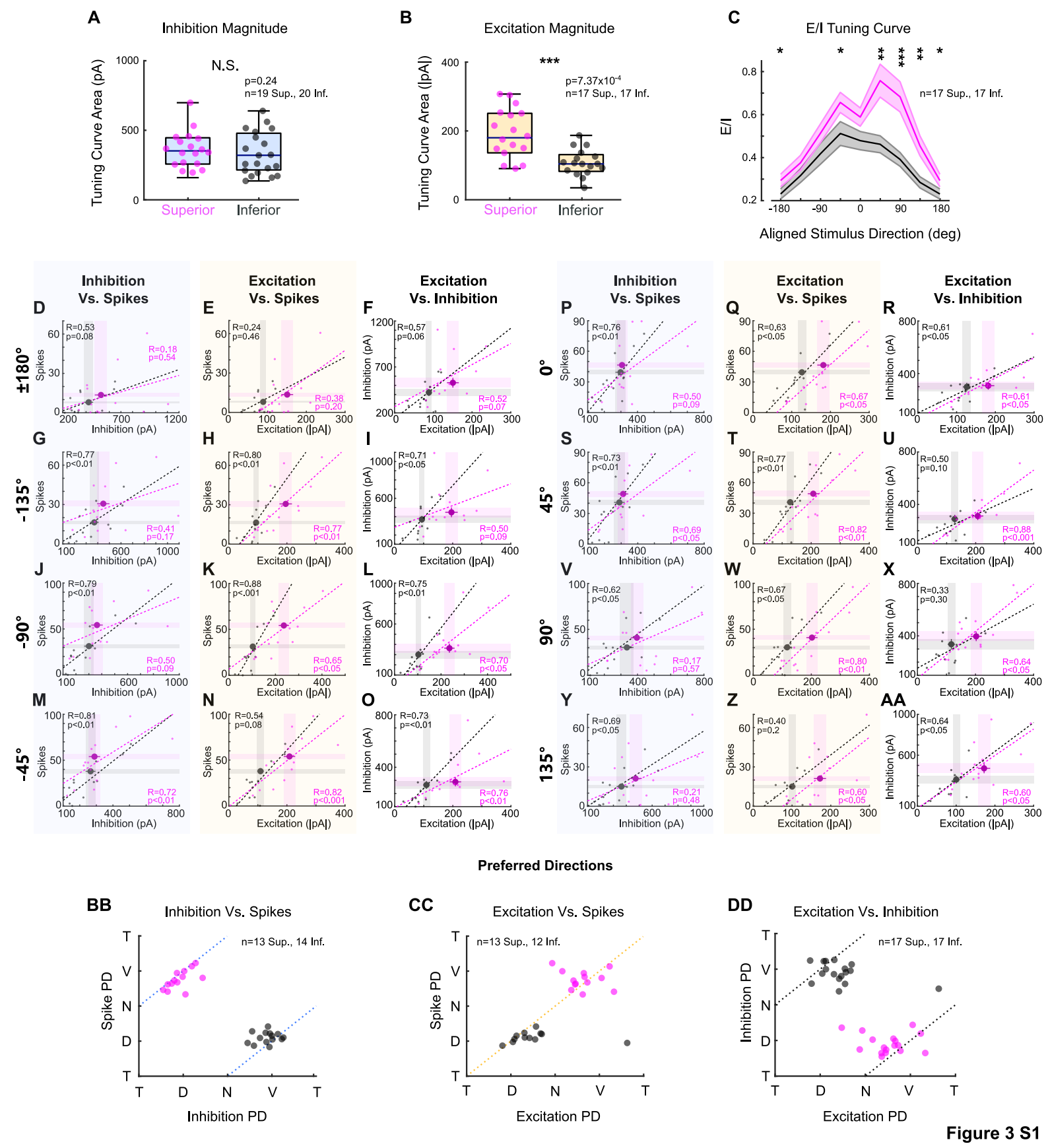
A
Inhibition Magnitude
Tuning Curve Area (pA)
N.S.
p=0.24
n=19 Sup., 20 Inf.
Superior
Inferior
B
Excitation Magnitude
Tuning Curve Area (|pA|)
***
p=7.37x10-4
n=17 Sup., 17 Inf.
Superior
Inferior
C
E/I Tuning Curve
E/I
n=17 Sup., 17 Inf.
Aligned Stimulus Direction (deg)
Inhibition Vs. Spikes
Excitation Vs. Spikes
Excitation Vs. Inhibition
±180°
-135°
-90°
-45°
0°
45°
90°
135°
Spikes
Inhibition (pA)
Excitation (|pA|)
Preferred Directions
BB
Inhibition Vs. Spikes
n=13 Sup., 14 Inf.
Spike PD
Inhibition PD
CC
Excitation Vs. Spikes
n=13 Sup., 12 Inf.
Spike PD
Excitation PD
DD
Excitation Vs. Inhibition
n=17 Sup., 17 Inf.
Inhibition PD
Excitation PD

Figure 3 S1

Figure 3 - figure supplement 1. Superior oDSGCs receive more excitatory input, but are less intrinsically excitable, than Inferior oDSGCs. (A-B) Linear tuning curve areas of the peak **(A)** inhibitory and **(B)** excitatory current measured in voltage-clamp recordings. Horizontal line represents median, box boundaries are IQR, and whiskers represent most extreme observation within 1.5xIQR. **(C)** Ratio of peak excitatory to peak inhibitory current (E/I) for each aligned stimulus direction (mean±SEM), for cells in which both metrics were measured. 0° is directly superior (for Superior oDSGCs) or inferior (for Inferior oDSGCs) motion. Positive directions are clockwise. Statistical significance for each stimulus direction changes depending on how the tuning curves of Superior and Inferior oDSGCs are aligned (e.g. 180° rotation vs. reflection over the x-axis). In general, E/I of Superior oDSGCs is greater than that of Inferior oDSGCs. **(D-AA)** For each bar direction, inhibition vs. spikes, excitation vs. spikes, and excitation vs. inhibition for cells in which both metrics were recorded (excitation and inhibition are peak values from voltage-clamp recordings, spikes are counts from cell-attached recordings). Dashed lines are least-squares linear regressions for Superior (magenta) and Inferior (gray) oDSGCs. R and p values are the Spearman's rank correlation coefficient and associated two-sided significance, respectively. Large points represent univariate means±SEM for each cell type taken from full data sets (i.e., small dots represent only a subset of cells in which both metrics were recorded, but full univariate datasets also consist of cells in which just one metric was recorded). Directions indicate aligned stimulus directions [as in (C)]. For excitation vs. spikes, the fit line for Superior oDSGCs tends to fall below the fit line for Inferior oDSGCs, indicating lower intrinsic excitability. However, greater excitatory inputs to Superior oDSGCs outweigh the difference in intrinsic excitability, leading to more total spikes in Superior oDSGCs. Further, inhibition does not intuitively explain spike outputs since there is a positive correlation between inhibitory input and number of spikes across directions. This correlation is likely caused by an additional positive correlation between excitation and inhibition. Therefore, spikes are best explained by excitation. **(BB)** Preferred direction of inhibition vs. preferred direction of spikes recorded in the same cell. Dashed line represents the prediction for a 180° difference. **(CC)** Preferred direction of excitation vs. preferred direction of spikes recorded in the same cell. Dashed line represents prediction for 0° difference. **(DD)** Preferred direction of excitation vs. preferred direction of inhibition recorded in the same cell. Dashed line represents the prediction for 180° difference. Labels of T, D, N, and V correspond to temporal, dorsal, nasal, and ventral directions on the retina, respectively. *$p<0.05$, **$p<0.01$, ***$p<0.001$

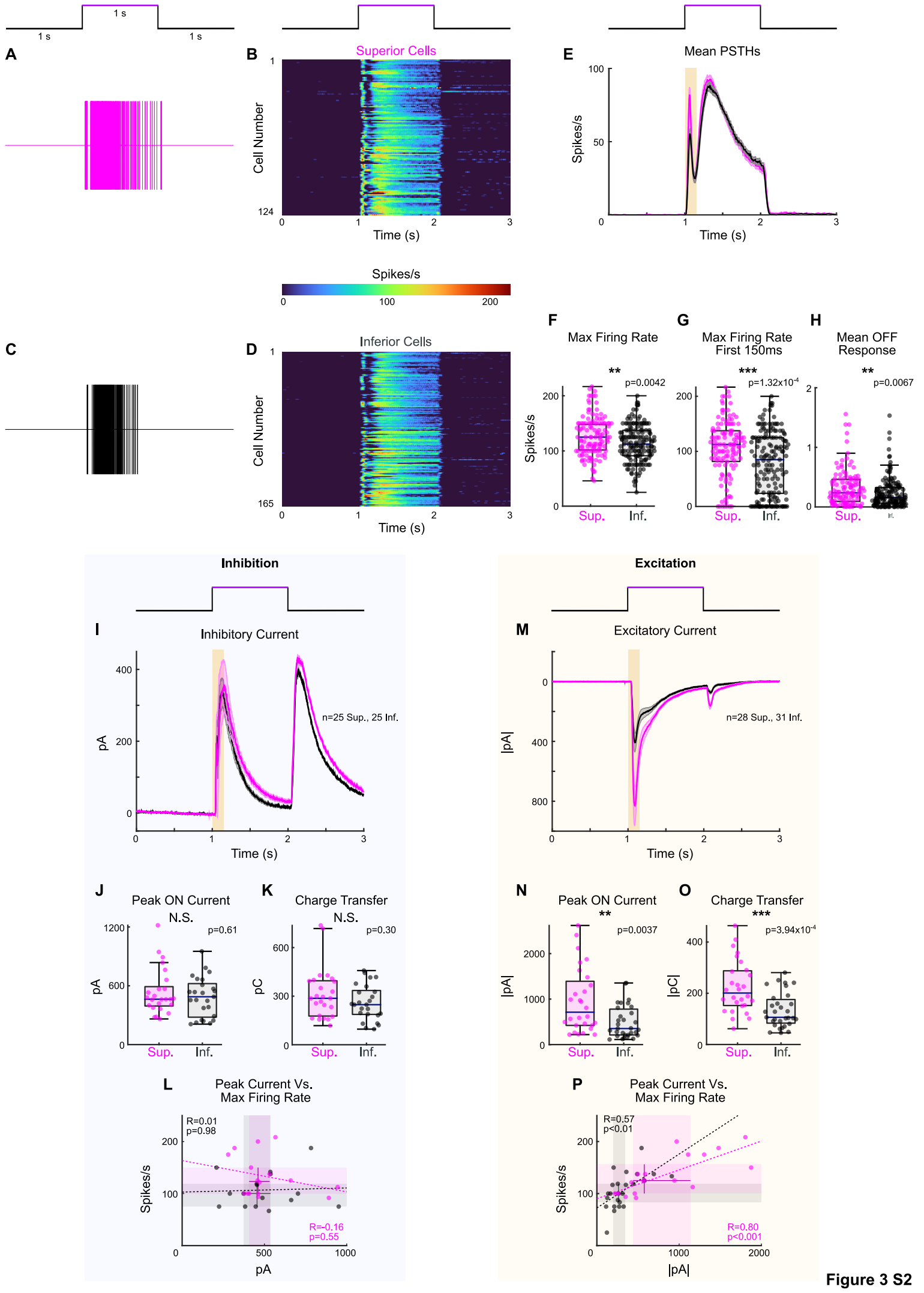
1 s
1 s
1 s
A
B
Superior Cells
Cell Number
1
124
0
1
2
3
Time (s)
Spikes/s
0
100
200
E
Mean PSTHs
Spikes/s
100
50
0
1
2
3
Time (s)
C
D
Inferior Cells
Cell Number
1
165
0
1
2
3
Time (s)
F
Max Firing Rate
**
p=0.0042
Spikes/s
200
100
0
Sup.
Inf.
G
Max Firing Rate
First 150ms
***
p=1.32x10-4
200
100
0
Sup.
Inf.
H
Mean OFF
Response
**
p=0.0067
2
1
0
Sup.
Inf.
Inhibition
I
Inhibitory Current
400
200
0
pA
n=25 Sup., 25 Inf.
0
1
2
3
Time (s)
J
Peak ON Current
N.S.
p=0.61
1200
600
0
pA
Sup.
Inf.
K
Charge Transfer
N.S.
p=0.30
600
300
0
pC
Sup.
Inf.
L
Peak Current Vs.
Max Firing Rate
R=0.01
p=0.98
200
100
0
Spikes/s
R=-0.16
p=0.55
500
1000
pA
Excitation
M
Excitatory Current
0
400
800
|pA|
n=28 Sup., 31 Inf.
0
1
2
3
Time (s)
N
Peak ON Current
**
p=0.0037
2000
1000
0
|pA|
Sup.
Inf.
O
Charge Transfer
***
p=3.94x10-4
400
200
0
|pC|
Sup.
Inf.
P
Peak Current Vs.
Max Firing Rate
R=0.57
p<0.01
200
100
0
Spikes/s
R=0.80
p<0.001
1000
2000
|pA|

Figure 3 S2

Figure 3 - figure supplement 2. Full-field light increments elicit more spikes and excitation in Superior oDSGCs. (A, C) Example extracellular spike rasters from **(A)** a Superior and **(C)** an Inferior oDSGC in response to a 1 second light increment. The schematic above shows the timing of the increment relative to the data. **(B, D)** Peristimulus time histograms (PSTHs) of average cell-attached light increment responses for each of **(B)** n=124 Superior and **(D)** n=165 Inferior oDSGCs. **(E)** Average PSTH across all cells shown in (B) and (D) (mean±SEM). Highlighted region shows the first 150 ms after stimulus onset. **(F)** Distributions of each cell's maximum firing rate throughout the entirety of the light increment. **(G)** Maximum firing rates during the first 150 ms after stimulus onset, i.e., highlighted region in (E). **(H)** Mean firing rates ≥50 ms after stimulus offset. **(I)** Average inhibitory current in response to the 1 second light increment for Superior (magenta) and Inferior (gray) oDSGCs (mean±SEM; voltage-clamp at +10 mV). **(J)** Peak inhibitory currents for the duration of the stimulus. **(K)** Total inhibitory charge transfers for the duration of the stimulus. **(L)** Peak inhibitory currents versus maximum firing rate for cells in which both metrics were recorded. **(M)** Average excitatory current in response to the 1 second light increment for Superior (magenta) and Inferior (gray) oDSGCs (mean±SEM; voltage-clamp at -60 mV). **(N)** Peak excitatory currents for the duration of the stimulus. **(O)** Total excitatory charge transfers for the duration of the stimulus. **(P)** Peak excitatory current versus maximum firing rate for cells in which both metrics were recorded. Dashed lines are least-squares linear regressions for Superior (magenta) and Inferior (gray) oDSGCs. R and p values are the Spearman's rank correlation coefficient and associated significance, respectively. The magenta line falls below the black line, indicating that Superior oDSGCs have a lower ratio of spike output to excitatory input. For box plots, the horizontal line represents median, box boundaries are IQR, and whiskers represent the most extreme observation within 1.5xIQR. *p<0.05, **p<0.01, ***p<0.001

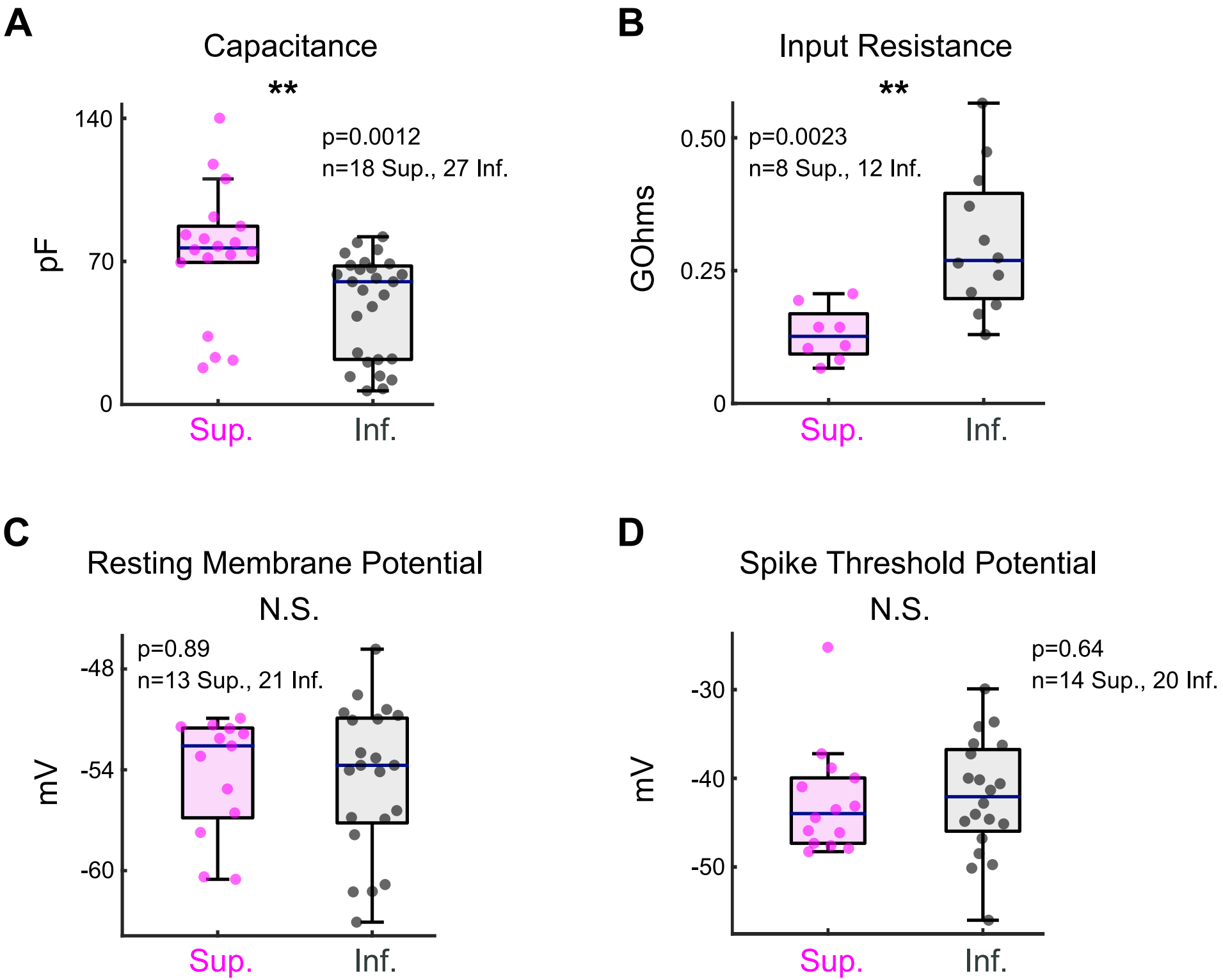
A
Capacitance
**
p=0.0012
n=18 Sup., 27 Inf.
pF
140
70
0
Sup.
Inf.
B
Input Resistance
**
p=0.0023
n=8 Sup., 12 Inf.
GOhms
0.50
0.25
0
Sup.
Inf.
C
Resting Membrane Potential
N.S.
p=0.89
n=13 Sup., 21 Inf.
mV
-48
-54
-60
Sup.
Inf.
D
Spike Threshold Potential
N.S.
p=0.64
n=14 Sup., 20 Inf.
mV
-30
-40
-50
Sup.
Inf.

Figure 4 S1

Figure 4 - Figure Supplement 1. Intrinsic electrophysiological properties of oDSGCs. (A) Membrane capacitance, (B) input resistance, (C) resting membrane potential, and (D) spike threshold potential were measured from Superior (magenta) and Inferior (gray) oDSGCs during whole-cell patch-clamp recordings. Consistent with their larger morphological size (Fig 4B), Superior oDSGCs have larger capacitances and lower input resistances than Inferior oDSGCs. There was no significant difference in either resting membrane potential or spike threshold potential across cell types. For all panels, the blue line represents median, box boundaries are IQR, and whiskers represent the most extreme observation within 1.5xIQR. *$p<0.05$, **$p<0.01$, ***$p<0.001$.

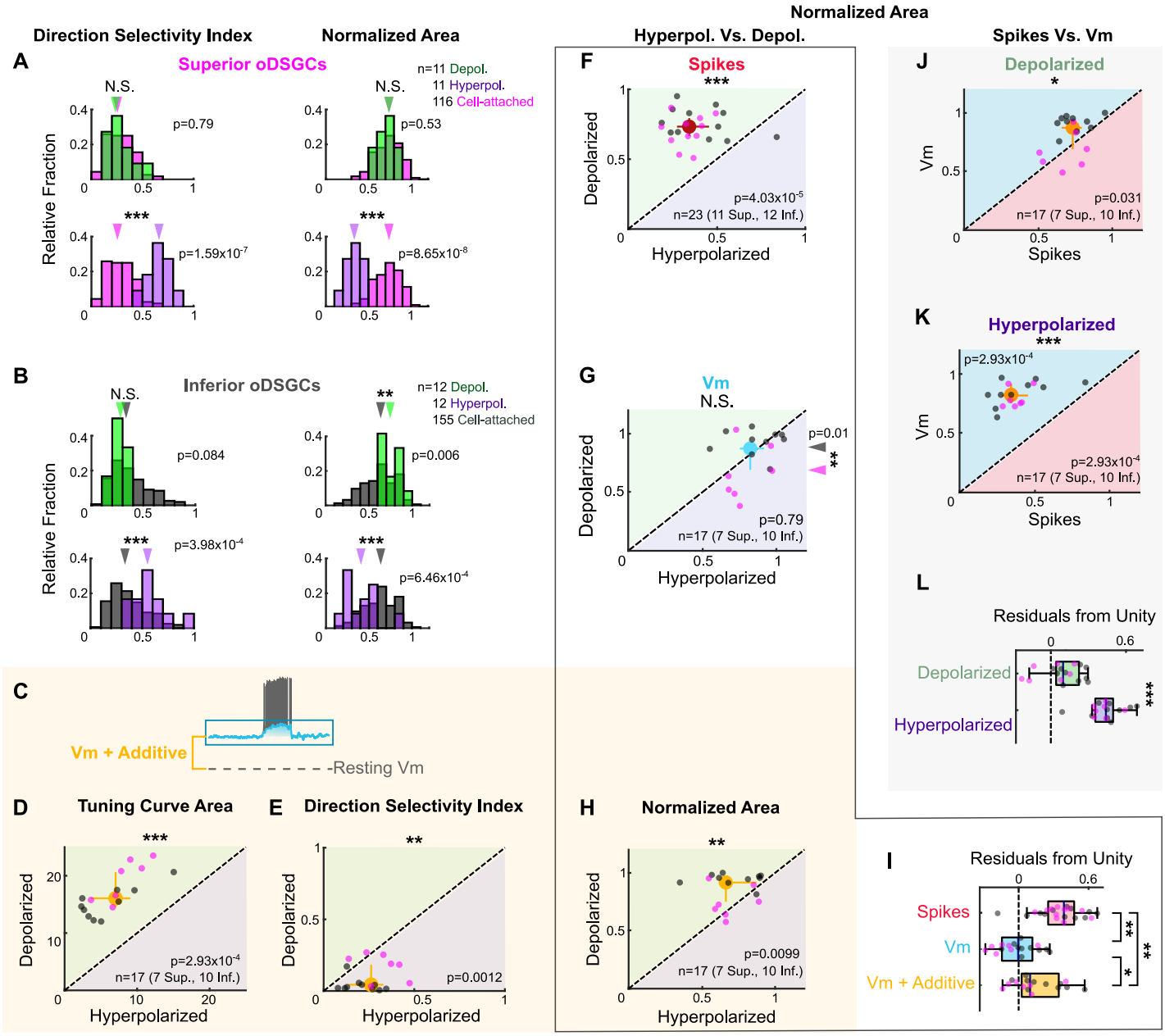
Direction Selectivity Index
Normalized Area
Normalized Area
Hyperpol. Vs. Depol.
Spikes Vs. Vm
A
Superior oDSGCs
n=11 Depol.
11 Hyperpol.
116 Cell-attached
N.S.
p=0.79
p=0.53
***
p=1.59x10-7
p=8.65x10-8
Relative Fraction
B
Inferior oDSGCs
n=12 Depol.
12 Hyperpol.
155 Cell-attached
N.S.
**
p=0.084
p=0.006
***
p=3.98x10-4
p=6.46x10-4
C
Vm + Additive
Resting Vm
D
Tuning Curve Area
p=2.93x10-4
n=17 (7 Sup., 10 Inf.)
E
Direction Selectivity Index
p=0.0012
F
Spikes
p=4.03x10-5
n=23 (11 Sup., 12 Inf.)
G
Vm
N.S.
p=0.01
p=0.79
n=17 (7 Sup., 10 Inf.)
H
Normalized Area
p=0.0099
n=17 (7 Sup., 10 Inf.)
Depolarized
Hyperpolarized
I
Residuals from Unity
Spikes
Vm
Vm + Additive
J
Depolarized
p=0.031
n=17 (7 Sup., 10 Inf.)
K
Hyperpolarized
p=2.93x10-4
n=17 (7 Sup., 10 Inf.)
Vm
Spikes
L
Residuals from Unity
Depolarized
Hyperpolarized

Figure 5 S1

Figure 5 - figure supplement 1. Spike and subthreshold voltage tuning curves with directionally untuned current injections. (A-B) Comparison of spike tuning curve metrics from cell-attached and current injection recordings. Histograms show the direction selectivity index (left) and area of the normalized tuning curve (right) for cell attached [magenta in (A) or gray in (B)], hyperpolarizing (green, top), and depolarizing (purple, bottom) conditions for **(A)** Superior and **(B)** Inferior oDSGCs. **(C)** Illustration of the voltage offset added via current injection during the depolarizing condition. The same offset was subtracted for the hyperpolarizing condition. Diagram is not shown to scale. **(D-E, H)** Metrics of the subthreshold membrane potential tuning curve during hyperpolarizing (abscissa) and depolarizing (ordinate) current injections with the additive offset taken into account: **(D)** linear tuning curve area, **(E)** direction selectivity index, **(H)** area of the normalized tuning curve. Regions of green [or purple] indicate that the metric is greater for depolarizing [or hyperpolarizing] currents. Points on the line indicate equivalent values under the two conditions. Individual cells are shown as dots (Superior in magenta, Inferior in gray). Yellow circles represent univariate medians collapsed across cell types and whiskers indicate 95% confidence intervals determined via bootstrapping. Significance values indicate whether the data tend to fall unevenly on one side of the unity line (2-sided signed-rank). Additive effects cause larger and broader membrane potential tuning curves following increases in the amount of untuned excitation. **(F-H)** Area of the normalized tuning curve during hyperpolarizing (abscissa) and depolarizing (ordinate) current injections for **(F)** spikes, **(G)** subthreshold voltages, and **(H)** subthreshold voltages with the additive offset taken into account. All metrics were measured simultaneously. **(I)** Residuals from the unity line for individual cells from the plots in (F-H). Dashed line indicates unity (i.e. no difference across depolarizing and hyperpolarizing conditions). Current injections influence spike tuning curves more than either version of the Vm tuning curves. **(J-K)** Area of the normalized tuning curve for spikes (abscissa) and simultaneously measured subthreshold voltages (ordinate) under **(J)** depolarizing and **(K)** hyperpolarizing conditions. **(L)** Residuals from the unity line for individual cells from the plots in (J-K). Dashed line indicates unity (i.e., no difference between spikes and subthreshold voltages). Comparisons in (I) and (L) are made between conditions (2-sided rank-sum). For box plots, the blue line represents median, box boundaries are IQR, and whiskers represent the most extreme observation within 1.5xIQR. *$p<0.05$, **$p<0.01$, ***$p<0.001$.

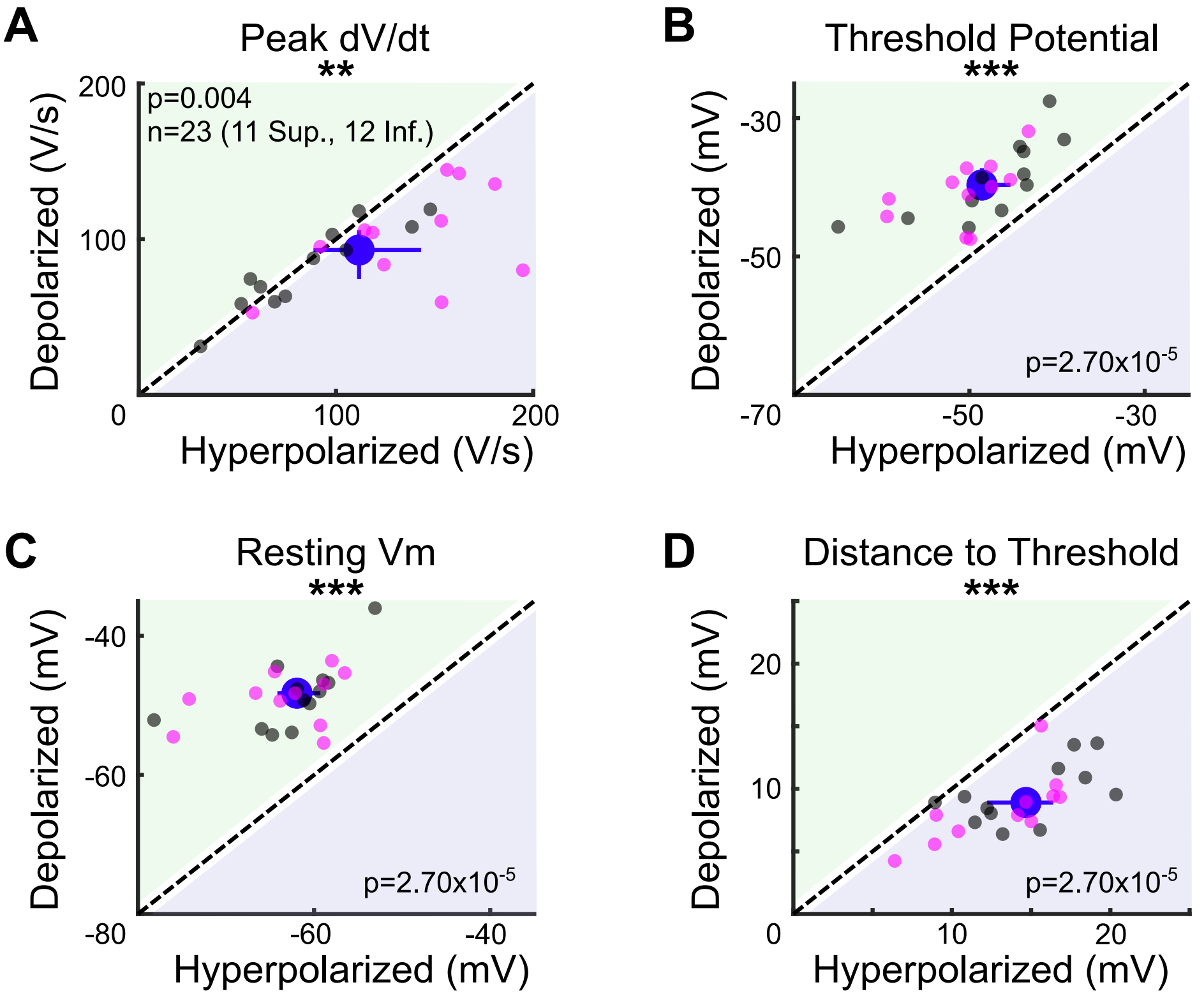
A
Peak dV/dt
**
p=0.004
n=23 (11 Sup., 12 Inf.)
Depolarized (V/s)
Hyperpolarized (V/s)
200
100
0
100
200
B
Threshold Potential
***
Depolarized (mV)
Hyperpolarized (mV)
-30
-50
-70
-50
-30
p=2.70x10-5
C
Resting Vm
***
Depolarized (mV)
Hyperpolarized (mV)
-40
-60
-80
-60
-40
p=2.70x10-5
D
Distance to Threshold
***
Depolarized (mV)
Hyperpolarized (mV)
20
10
0
10
20
p=2.70x10-5

Figure 5 S2

Figure 5 - figure supplement 2. Effects of current injection on intrinsic properties of oDSGCs. To measure the effects of depolarizing and hyperpolarizing current injections on the intrinsic properties of oDSGCs, the **(A)** peak rate of voltage change and **(B)** spike threshold potential were calculated for every cell under both conditions. Peak dV/dt was on average 10.9 V/s greater under hyperpolarizing relative to depolarizing conditions. The spike threshold potential was on average 9.0 mV more negative under hyperpolarizing conditions. Both of these changes are consistent with an increase in voltage-gated sodium channel availability in the hyperpolarizing condition. This intrinsic change increases the probability of spikes during hyperpolarizing relative to the depolarizing injections, and therefore cannot explain our experimental results of greater spikes and broader tuning curves under depolarizing conditions (Fig 5). The likely reason why our empirical data show increased spiking and broader tuning curves during depolarizing injections is that the relative distance between cells' resting membrane potentials and spike thresholds was greater in the hyperpolarizing condition. **(C)** The resting membrane potential was, on average, 12.6 mV more negative during hyperpolarizing injections than during depolarizing injections, whereas the spike threshold only changed by 9.0 mV **(B)**. Thus, the difference between resting membrane potential and spike threshold was greater under hyperpolarizing conditions. **(D)** On average, cells' resting membrane potentials were 5.1 mV further away from the spike threshold potential under hyperpolarizing relative to depolarizing conditions. Current injections may also influence conductances of other voltage-gated ion channels, including calcium channels, though evidence that oDSGCs express such channels is limited and these effects are difficult to quantify. For all panels, regions of green [or purple] indicate that the metric is greater for depolarizing [or hyperpolarizing] current injections. Points on the line indicate equivalent values under the two conditions. Individual cells are shown as dots (Superior in magenta, Inferior in gray). Blue circles represent univariate medians collapsed across cell types and whiskers indicate 95% confidence intervals determined via bootstrapping. Significance values indicate whether the data tend to fall unevenly on one side of the unity line (2-sided signed-rank). *$p<0.05$, **$p<0.01$, ***$p<0.001$.

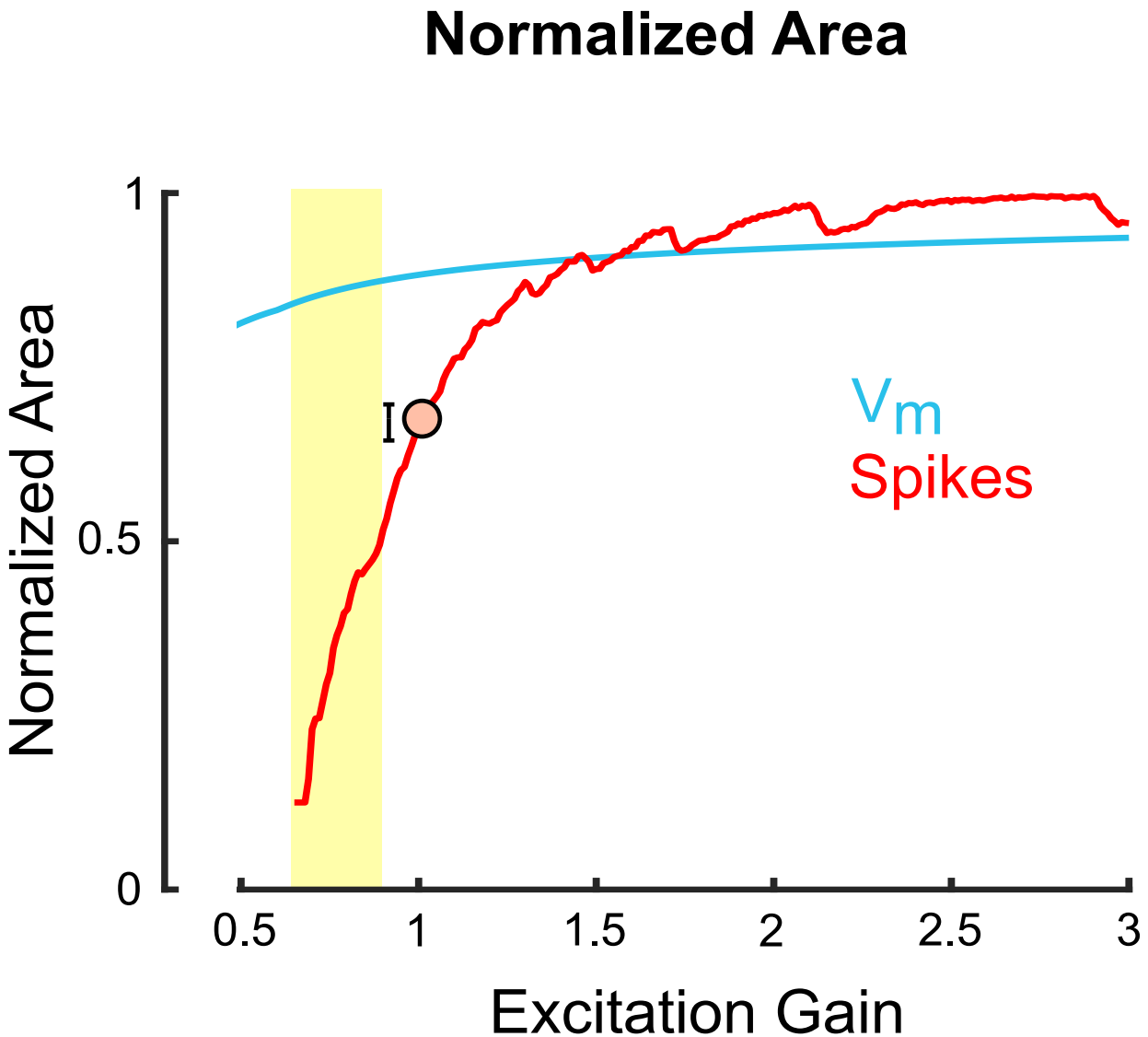
Normalized Area
Normalized Area
1
0.5
0
0.5
1
1.5
2
2.5
3
Excitation Gain
I
Vm
Spikes

Figure 6 S1

Figure 6 - figure supplement 1. The normalized area of model spike, but not subthreshold membrane potential, tuning curves are steeply influenced by excitation gain. Area of the normalized tuning curve for spikes (red) and underlying subthreshold membrane potentials (blue) as a function of the gain of an untuned excitatory input to a model oDSGC. Greater values along the vertical axis indicate a broader tuning curve. Additive excitation contributes to the slow rise of the membrane potential line, whereas thresholding effects cause the steep change in spike tuning curve shape. The orange dot [and error bars] corresponds to the empirically measured median [and 95% confidence intervals determined via bootstrapping] for this metric from cell-attached recordings, collapsed across cell types.

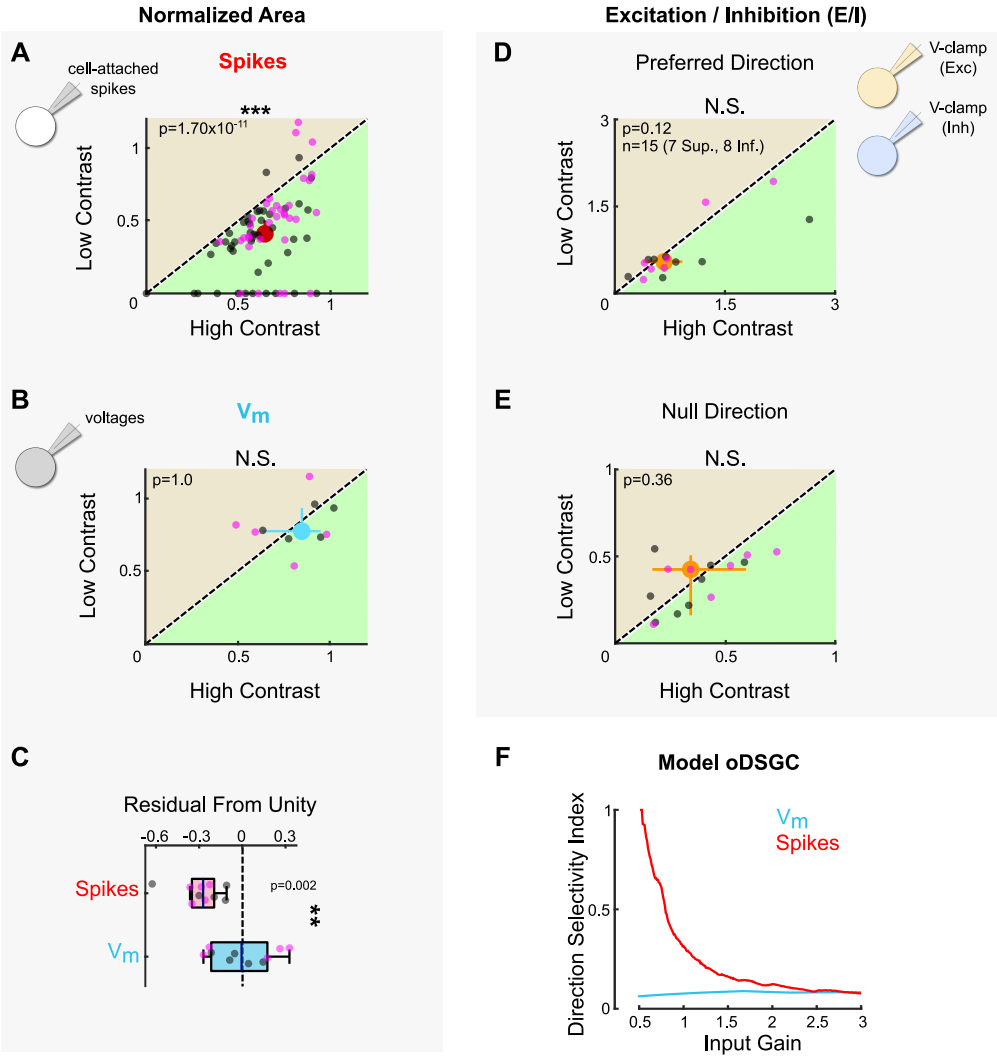
Normalized Area
Excitation / Inhibition (E/I)
A
cell-attached spikes
Spikes
***
p=1.70x10-11
Low Contrast
High Contrast
B
voltages
Vm
N.S.
p=1.0
Low Contrast
High Contrast
C
Residual From Unity
-0.6 -0.3 0 0.3
Spikes
Vm
p=0.002
**
D
Preferred Direction
V-clamp (Exc)
V-clamp (Inh)
N.S.
p=0.12
n=15 (7 Sup., 8 Inf.)
Low Contrast
High Contrast
E
Null Direction
N.S.
p=0.36
Low Contrast
High Contrast
F
Model oDSGC
Vm
Spikes
Direction Selectivity Index
Input Gain

Figure 7 S1

Figure 7 - figure supplement 1. Stimulus contrast modulates spike tuning curve width but not the ratio of excitation to inhibition. (A) Area of the normalized tuning curve from spike responses to high (abscissa) and low (ordinate) contrast bars drifting in 8 directions. Differences between Superior (magenta) and Inferior (gray) oDSGCs persist under low contrast (see Fig 2). **(B)** Area of the normalized tuning curve from subthreshold voltages in response to high (abscissa) and low (ordinate) contrast bars drifting in 8 directions. **(C)** Residuals from the unity line for simultaneously measured spikes [as in (A)] and subthreshold voltages [as in (B)]. The dashed line indicates unity (i.e. no difference between high and low contrast). Comparison is made across conditions. **(D-E)** Excitation-to-inhibition (E/I) ratios for high and low contrast bars drifting in **(D)** the preferred and **(E)** the null direction of each cell. **(F)** Direction selectivity index generated from a parallel conductance model of an oDSGC under different scale factors applied jointly to excitatory and inhibitory inputs (constant E/I). For all scatter plots, the region of green [or tan] indicates the metric is greater under high [or low] contrast conditions. Points on the line indicate equivalent metrics under the two conditions. Individual cells are represented by small dots. Large dots represent univariate medians (collapsed across cell type). Whiskers indicate 95% confidence intervals determined via bootstrapping. Significance values indicate whether the data tend to fall unevenly on one side of the unity line (2-sided signed-rank). Data acquired following epifluorescence targeting. *$p<0.05$, **$p<0.01$, ***$p<0.001$

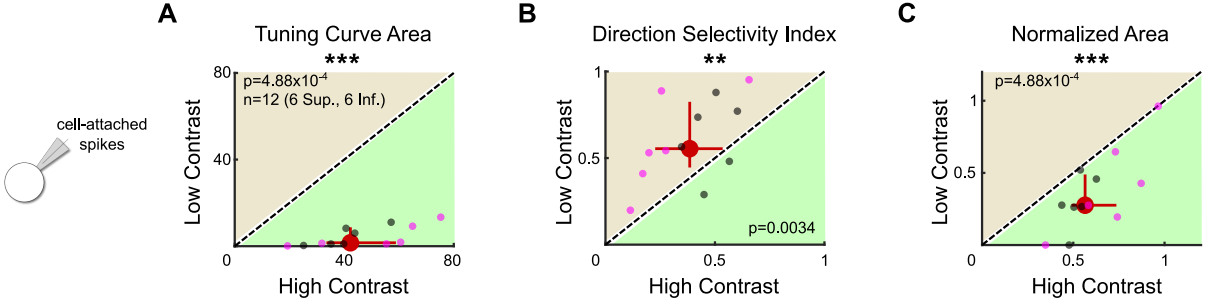
A
Tuning Curve Area
***
p=4.88x10-4
n=12 (6 Sup., 6 Inf.)
Low Contrast
High Contrast
0
40
80
cell-attached
spikes
B
Direction Selectivity Index
**
p=0.0034
Low Contrast
High Contrast
0
0.5
1
C
Normalized Area
***
p=4.88x10-4
Low Contrast
High Contrast
0
0.5
1

Figure7 S2

Figure 7 - figure supplement 2. Two-photon targeting confirms that oDSGCs are contrast sensitive. (A) Tuning curve area, **(B)** direction selectivity index, and **(C)** normalized area were measured in the cell-attached configuration in response to high and low contrast drifting bars following two-photon targeting of oDSGCs. As occurred following epifluorescence targeting (Fig 7), two-photon targeting revealed that the spike tuning curves of oDSGCs were smaller (A) and narrower (B, C) in response to low contrast stimuli. For all plots, regions of green [or tan] indicate that the metric is greater for high [or low] contrast stimuli. Points on the line indicate equivalent metrics under the two conditions. Individual cells are shown as dots (Superior in magenta, Inferior in gray). Red circles represent univariate medians collapsed across cell types. Whiskers indicate 95% confidence intervals determined via bootstrapping. Significance values indicate whether the data tend to fall unevenly on one side of the unity line (2-sided signed-rank). *$p<0.05$, **$p<0.01$, ***$p<0.001$.

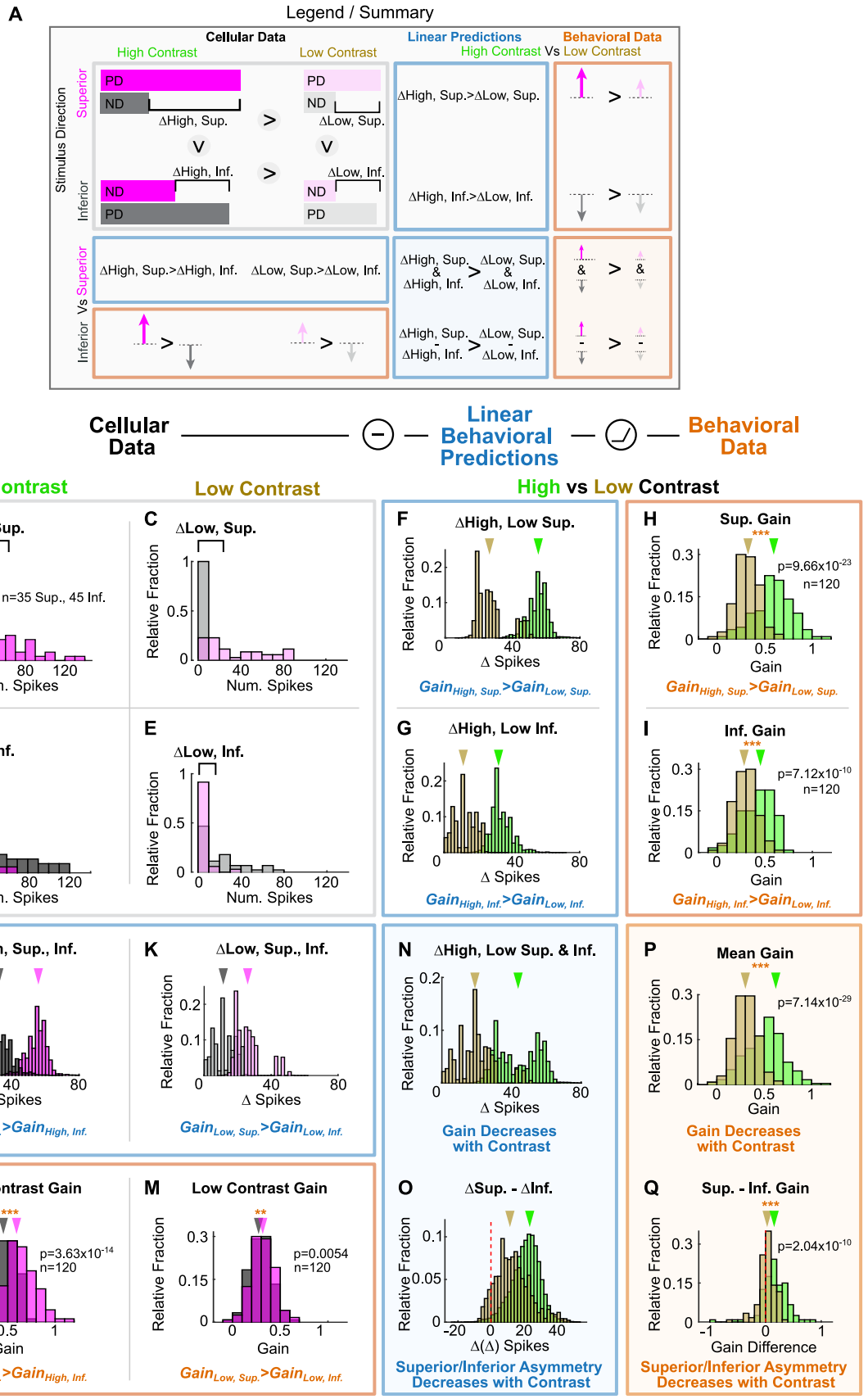
A
Legend / Summary
Cellular Data
High Contrast
Low Contrast
Linear Predictions
High Contrast Vs Low Contrast
Behavioral Data
Stimulus Direction
Superior
Inferior
PD
ND
ΔHigh, Sup.
ΔLow, Sup.
ΔHigh, Inf.
ΔLow, Inf.
ΔHigh, Sup.>ΔLow, Sup.
ΔHigh, Inf.>ΔLow, Inf.
Vs
ΔHigh, Sup.>ΔHigh, Inf.
ΔLow, Sup.>ΔLow, Inf.
Cellular Data
Linear Behavioral Predictions
Behavioral Data
High Contrast
Low Contrast
High vs Low Contrast
Superior Stimulus
Inferior Stimulus
Superior vs Inferior Stimulus
B ΔHigh, Sup.
n=35 Sup., 45 Inf.
C ΔLow, Sup.
D ΔHigh, Inf.
E ΔLow, Inf.
Relative Fraction
Num. Spikes
F ΔHigh, Low Sup.
Δ Spikes
Gain High, Sup.>Gain Low, Sup.
G ΔHigh, Low Inf.
Gain High, Inf.>Gain Low, Inf.
H Sup. Gain
p=9.66x10-23
n=120
Gain
Gain High, Sup.>Gain Low, Sup.
I Inf. Gain
p=7.12x10-10
n=120
Gain High, Inf.>Gain Low, Inf.
J ΔHigh, Sup., Inf.
Gain High, Sup.>Gain High, Inf.
K ΔLow, Sup., Inf.
Gain Low, Sup.>Gain Low, Inf.
N ΔHigh, Low Sup. & Inf.
Gain Decreases with Contrast
O ΔSup. - ΔInf.
Δ(Δ) Spikes
Superior/Inferior Asymmetry Decreases with Contrast
P Mean Gain
p=7.14x10-29
Gain Decreases with Contrast
Q Sup. - Inf. Gain
p=2.04x10-10
Gain Difference
Superior/Inferior Asymmetry Decreases with Contrast
L High Contrast Gain
p=3.63x10-14
n=120
Gain High, Sup.>Gain High, Inf.
M Low Contrast Gain
p=0.0054
n=120
Gain Low, Sup.>Gain Low, Inf.

Figure 8 S1

Figure 8 - figure supplement 1. Behavioral OKR prediction from drifting bar stimulus. Spikes of Superior and Inferior oDSGCs in response to the drifting bar stimulus were used to predict the magnitude of OKR gain in behaving animals. **(A)** Legend and summary for panels (B-Q). Cellular Data (gray box): The responses of Superior (magenta) and Inferior (gray) oDSGCs to preferred (PD) and null (ND) direction drifting bars at high (left column) and low (20% relative contrast, right column) contrasts. Linear predictions (blue boxes): the differences between responses in the preferred and null directions, represented by Δ, provide predictions of the relative OKR gain across stimulus directions and contrasts. Behavioral results (orange boxes): arrows represent the magnitude of OKR gain measured in behaving mice across stimulus directions and contrasts. Dark arrows represent high contrast stimuli and light arrows represent low contrast stimuli. **(B-E)** Cellular Data: Distributions of superior (magenta) and Inferior (gray) oDSGC spike responses to superior (top row) and inferior (bottom row) stimuli at high (left column) and low (right column) contrast. Brackets above show the difference between the medians of the two distributions. Same data plotted in Fig 8B. **(F-G, J-K, N-O)** Linear predictions from data in (B-E) for how behavioral OKR gain changes across stimulus directions and contrasts. The asymmetries in the tuning curves of Superior and Inferior oDSGCs resulted in four first-order linear predictions for how OKR gain changes across stimulus conditions: (1) for superior stimuli, gain is greater in response to high contrast stimuli than to low contrast stimuli **(F)**, (2) for inferior stimuli, gain is greater in response to high contrast stimuli than to low contrast stimuli **(G)**, (3) at high contrast, gain is greater in response to superior stimuli than to inferior stimuli **(J)**, and (4) at low contrast, gain is greater in response to superior stimuli than to inferior stimuli **(K)**. Two additional second-order hypotheses were made that rely on an approximately linear relationship between differences in oDSGC output and gain in the tested regime: (5) gain is higher under high contrast, regardless of stimulus direction **(N)**, and (6) behavioral asymmetries in response to superior and inferior stimuli diminish with decreasing contrast **(O)**. **(H-I, L-M, P-Q)** The six linear predictions were tested by measuring OKR in behaving mice in response to superior and inferior oscillating gratings at high and low contrast. All six linear predictions accurately matched behavior. Distributions in these panels are made up of the average OKR gain over the course of individual half oscillation cycles, arrows indicate medians (2-sided signed rank). *$p<0.05$, **$p<0.01$, ***$p<0.001$.

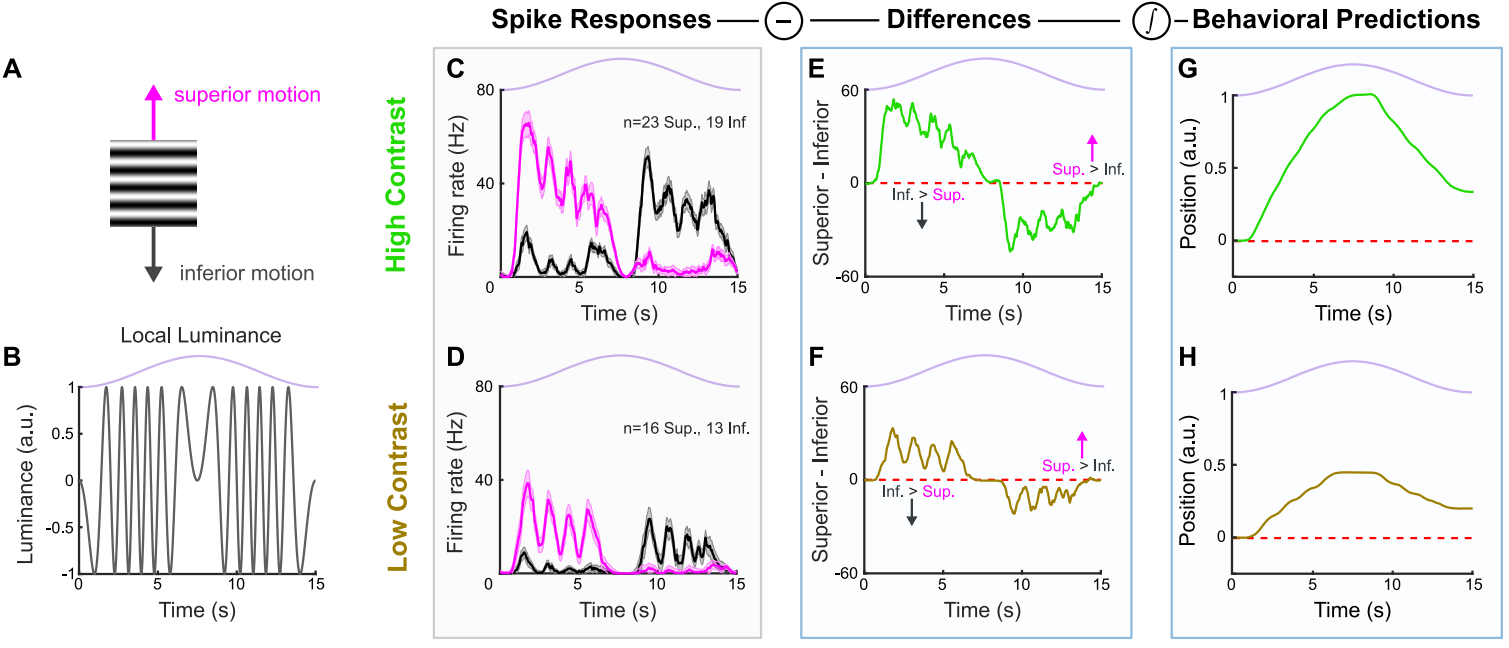
Spike Responses
Differences
Behavioral Predictions
A
superior motion
inferior motion
B
Local Luminance
Luminance (a.u.)
Time (s)
High Contrast
Low Contrast
C
n=23 Sup., 19 Inf
Firing rate (Hz)
Time (s)
D
n=16 Sup., 13 Inf.
Firing rate (Hz)
Time (s)
E
Superior - Inferior
Sup. > Inf.
Inf. > Sup.
Time (s)
F
Superior - Inferior
Sup. > Inf.
Inf. > Sup.
Time (s)
G
Position (a.u.)
Time (s)
H
Position (a.u.)
Time (s)

Figure 8 S2

Figure 8 - figure supplement 2. oDSGC responses to oscillating gratings. (A) Oscillating sinusoidal gratings used in oDSGC electrophysiology were equivalent to those used in behavioral experiments. Motion directions apply to all panels. **(B)** Luminance of a single point in space as the sinusoidal grating completes one oscillation cycle. A value of 1.0 along the ordinate indicates full luminance and -1.0 indicates minimal luminance. This luminance function is determined by both the spatial frequency of the grating and the velocity of the sinusoidal oscillation. The light available to a single oDSGC follows such luminance fluctuations over the course of a single stimulus oscillation cycle, but the position of the oDSGC relative to the phase of the grating will cause a corresponding phase shift in its luminance function. These luminance oscillations therefore likely account for the high frequency oscillations seen in (C-F). Stimulus position is shown above in lavender. **(C)** Median spike responses of Superior (magenta) and Inferior (gray) oDSGCs over the course of a single high contrast oscillation cycle. Two-photon targeting was used during all recordings in this data set. Error bars represent standard error of the mean. **(D)** Same as (C), but for a low contrast stimulus, which, for this experiment, was defined as 50% contrast relative to the high contrast stimulus (see Methods). **(E-F)** Moment-by-moment subtraction of the median Inferior oDSGC firing rate from the median Superior oDSGC firing rate for **(E)** high and **(F)** low contrast gratings. Values fall above unity (dashed red line) when Superior oDSGCs spike more than Inferior oDSGCs, and below unity when Inferior oDSGCs spike more than Superior oDSGCs. This subtraction constitutes a linear prediction of eye velocity for each point in time. **(G-H)** Linear predictions of eye position across time for a single **(G)** high and **(H)** low contrast oscillation cycle. These predictions are the cumulative integral of the firing rate differences shown in (E) for high contrast and (F) low contrast. For all plots, lavender trace indicates the position of the grating stimulus in its oscillation cycle across time. Two-photon targeting was used during all recordings in this data set.

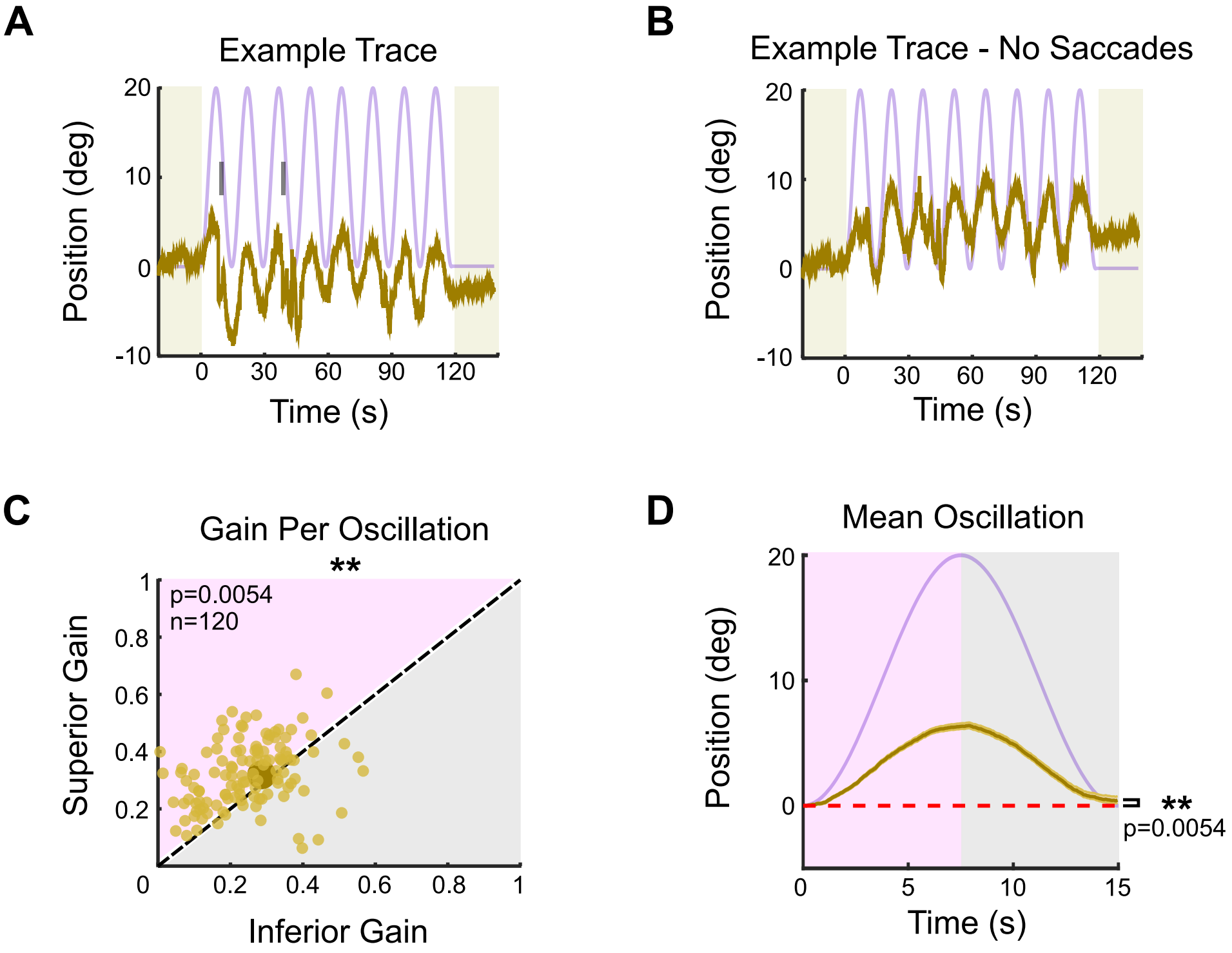
A
Example Trace
Position (deg)
20
10
0
-10
0
30
60
90
120
Time (s)
B
Example Trace - No Saccades
Position (deg)
20
10
0
-10
0
30
60
90
120
Time (s)
C
Gain Per Oscillation
**
p=0.0054
n=120
Superior Gain
1
0.8
0.6
0.4
0.2
0
0.2
0.4
0.6
0.8
1
Inferior Gain
D
Mean Oscillation
Position (deg)
20
10
0
**
p=0.0054
0
5
10
15
Time (s)

Figure 8 S3

Figure 8 - figure supplement 3. Optokinetic reflex at low contrast. Eye movements were measured from headfixed mice in response to an oscillating sinusoidal grating. All parameters of the grating were the same as under high contrast conditions (Fig 1), except for the grating contrast, which was five times lower (i.e., 20% relative contrast). **(A)** Example of OKR in response to the vertically oscillating low contrast grating. The eye position is shown in tan and the stimulus position is shown in lavender. Saccades are indicated by tick marks. **(B)** Same as A, but with saccades (fast nystagmuses) removed to reveal the asymmetry between superior and inferior OKR. For each epoch, animals viewed 8 oscillation cycles lasting a total of 120 seconds, flanked by 20 seconds of a static grating (shaded regions). **(C)** Average gain of slow nystagmus during the superior versus inferior stage of individual oscillations. Each small dot is a single oscillation. The region of magenta [or gray] indicates that gain was greater for the superior [or inferior] stage of the oscillation. Points that fall on the line indicate equivalent gain for both stimulus directions. Large point and whiskers represent univariate medians and 95% confidence intervals (via bootstrapping), respectively. Significance value indicates whether the points tend to fall unevenly on one side of the unity line (2-sided signed-rank). **(D)** Eye position (tan) and stimulus position (lavender) averaged across all oscillations and all animals (mean±SEM). Starting eye position is normalized to 0° at cycle onset. The average ending eye position is displaced in the superior direction (2-sided signed-rank). N=5 mice for all experiments; n=number of trials.

Spontaneous Eye Movements

A

Static Grating - Low Contrast

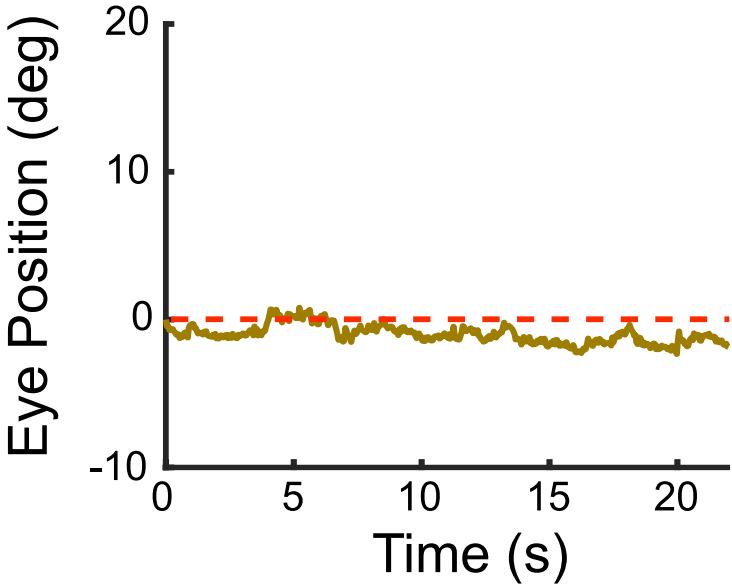

Absolute Eye Positions

B

Oscillating Grating - Low Contrast

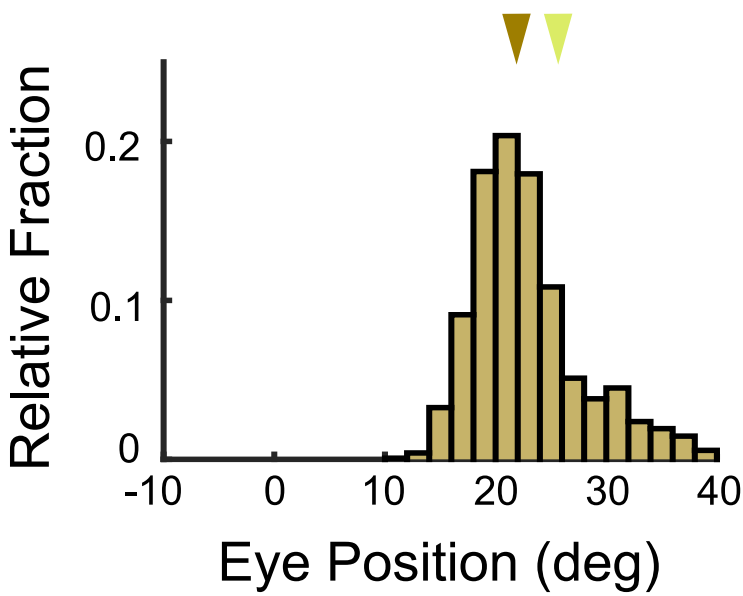

Figure 8 S4

Figure 8 - figure supplement 4. Baseline vertical eye movements to low contrast stimuli (see also Fig 1 - figure supplement 2). Vertical eye movements were measured in response to static, low (20% relative) contrast gratings to calculate eye drifts for baseline subtraction. **(A)** Example raw eye trace over 22 seconds of a static low contrast grating. The calculated position of the eye drifts downward over time. This may reflect true eye movements or a calibration error in our recording configuration, but these two possibilities cannot be disambiguated (see Methods). The magnitude of eye position drift during static gratings is approximately 11-fold less than the magnitude of the eye movements elicited by low contrast moving gratings (See Fig 1 - figure supplement 2A for comparison to high contrast grating). **(B)** Absolute vertical position of the eye without drift correction during low contrast gratings. Brown arrow marks the median of the distribution. Yellow arrow indicates median position of the eye prior to stimulus onset (as in Fig 1 - figure supplement 2C). Spontaneous drift velocity was baseline subtracted from eye positions in response to low contrast oscillating gratings since median eye position was similar to that measured in response to static gratings. For further data on eye drift and spontaneous eye movements to high contrast gratings see Fig 1 - figure supplement 2.

References

1. Zeil, J., Nalbach, G., and Nalbach, H.-O. (1989). Spatial Vision in a Flat World: Optical and Neural Adaptations in Arthropods. In Neurobiology of Sensory Systems, R. N. Singh and N. J. Strausfeld, eds. (Springer US), pp. 123–137. 10.1007/978-1-4899-2519-0_10.
2. Masseck, O.A., and Hoffmann, K.-P. (2009). Comparative Neurobiology of the Optokinetic Reflex. Ann. N. Y. Acad. Sci. *1164*, 430–439. 10.1111/j.1749-6632.2009.03854.x.
3. Simpson, J.I. (1984). The Accessory Optic System. Annu. Rev. Neurosci. *7*, 13–41. 10.1146/annurev.ne.07.030184.000305.
4. Collewijn, H. (1969). Optokinetic eye movements in the rabbit: Input-output relations. Vision Res. *9*, 117–132. 10.1016/0042-6989(69)90035-2.
5. Donaghy, M. (1980). The contrast sensitivity, spatial resolution and velocity tuning of the cat's optokinetic reflex. J. Physiol. *300*, 353–365.
6. Gravot, C.M., Knorr, A.G., Glasauer, S., and Straka, H. (2017). It's not all black and white: visual scene parameters influence optokinetic reflex performance in Xenopus laevis tadpoles. J. Exp. Biol. *220*, 4213–4224. 10.1242/jeb.167700.
7. Knorr, A.G., Gravot, C.M., Glasauer, S., and Straka, H. (2021). Image motion with color contrast suffices to elicit an optokinetic reflex in Xenopus laevis tadpoles. Sci. Rep. *11*, 8445. 10.1038/s41598-021-87835-2.
8. Leguire, L.E., Zaff, B.S., Freeman, S., Rogers, G.L., Bremer, D.L., and Wali, N. (1991). Contrast sensitivity of optokinetic nystagmus. Vision Res. *31*, 89–97. 10.1016/0042-6989(91)90076-H.
9. Cahill, H., and Nathans, J. (2008). The Optokinetic Reflex as a Tool for Quantitative Analyses of Nervous System Function in Mice: Application to Genetic and Drug-Induced Variation. PLOS ONE *3*, e2055. 10.1371/journal.pone.0002055.
10. Dehmelt, F.A., Meier, R., Hinz, J., Yoshimatsu, T., Simacek, C.A., Huang, R., Wang, K., Baden, T., and Arrenberg, A.B. (2021). Spherical arena reveals optokinetic response tuning to stimulus location, size, and frequency across entire visual field of larval zebrafish. eLife *10*, e63355. 10.7554/eLife.63355.
11. Shimizu, N., Tabata, H., Wada, Y., Sugita, Y., Yamanaka, T., Hosoi, H., and Kawano, K. (2010). Distribution of optokinetic sensitivity across the retina of mice in relation to eye orientation. Neuroscience *168*, 200–208. 10.1016/j.neuroscience.2010.03.025.
12. Dhande, O.S., Stafford, B.K., Lim, J.-H.A., and Huberman, A.D. (2015). Contributions of Retinal Ganglion Cells to Subcortical Visual Processing and Behaviors. Annu. Rev. Vis. Sci. *1*, 291–328. 10.1146/annurev-vision-082114-035502.
13. Giolli, R.A., Blanks, R.H.I., and Lui, F. (2006). The accessory optic system: basic organization with an update on connectivity, neurochemistry, and function. In Progress in Brain Research Neuroanatomy of the Oculomotor System., J. A. Büttner-Ennever, ed. (Elsevier), pp. 407–440. 10.1016/S0079-6123(05)51013-6.
14. Oyster, C.W. (1968). The analysis of image motion by the rabbit retina. J. Physiol. *199*, 613–635. 10.1113/jphysiol.1968.sp008671.
15. Oyster, C.W., and Barlow, H.B. (1967). Direction-Selective Units in Rabbit Retina: Distribution of Preferred Directions. Science *155*, 841–842. 10.1126/science.155.3764.841.
16. Sabbah, S., Gemmer, J.A., Bhatia-Lin, A., Manoff, G., Castro, G., Siegel, J.K., Jeffery, N., and Berson, D.M. (2017). A retinal code for motion along the gravitational and body axes. Nature *546*, 492–497. 10.1038/nature22818.
17. Dhande, O.S., Estevez, M.E., Quattrochi, L.E., El-Danaf, R.N., Nguyen, P.L., Berson, D.M., and Huberman, A.D. (2013). Genetic Dissection of Retinal Inputs to Brainstem Nuclei Controlling Image Stabilization. J. Neurosci. *33*, 17797–17813. 10.1523/JNEUROSCI.2778-13.2013.
18. Lilley, B.N., Sabbah, S., Hunyara, J.L., Gribble, K.D., Al-Khindi, T., Xiong, J., Wu, Z.,

Berson, D.M., and Kolodkin, A.L. (2019). Genetic access to neurons in the accessory optic system reveals a role for Sema6A in midbrain circuitry mediating motion perception. J. Comp. Neurol. *527*, 282–296. 10.1002/cne.24507.

19. Sun, L.O., Brady, C.M., Cahill, H., Al-Khindi, T., Sakuta, H., Dhande, O.S., Noda, M., Huberman, A.D., Nathans, J., and Kolodkin, A.L. (2015). Functional Assembly of Accessory Optic System Circuitry Critical for Compensatory Eye Movements. Neuron *86*, 971–984. 10.1016/j.neuron.2015.03.064.
20. Yonehara, K., Shintani, T., Suzuki, R., Sakuta, H., Takeuchi, Y., Nakamura-Yonehara, K., and Noda, M. (2008). Expression of SPIG1 Reveals Development of a Retinal Ganglion Cell Subtype Projecting to the Medial Terminal Nucleus in the Mouse. PLoS ONE *3*. 10.1371/journal.pone.0001533.
21. Yonehara, K., Ishikane, H., Sakuta, H., Shintani, T., Nakamura-Yonehara, K., Kamiji, N.L., Usui, S., and Noda, M. (2009). Identification of Retinal Ganglion Cells and Their Projections Involved in Central Transmission of Information about Upward and Downward Image Motion. PLoS ONE *4*. 10.1371/journal.pone.0004320.
22. Togt, C. van der, Want, J. van der, and Schmidt, M. (1993). Segregation of direction selective neurons and synaptic organization of inhibitory intranuclear connections in the medial terminal nucleus of the rat: An electrophysiological and immunoelectron microscopical study. J. Comp. Neurol. *338*, 175–192. 10.1002/cne.903380204.
23. Kay, J.N., Huerta, I.D. la, Kim, I.-J., Zhang, Y., Yamagata, M., Chu, M.W., Meister, M., and Sanes, J.R. (2011). Retinal Ganglion Cells with Distinct Directional Preferences Differ in Molecular Identity, Structure, and Central Projections. J. Neurosci. *31*, 7753–7762. 10.1523/JNEUROSCI.0907-11.2011.
24. Osterhout, J.A., Stafford, B.K., Nguyen, P.L., Yoshihara, Y., and Huberman, A.D. (2015). Contactin-4 Mediates Axon-Target Specificity and Functional Development of the Accessory Optic System. Neuron *86*, 985–999. 10.1016/j.neuron.2015.04.005.
25. Pak, M.W., Pinto, L.H., Mangini, N.J., Vanable, J.W., Giolli, R.A., and Gregory, K.M. (1987). Retinopretectal and accessory optic projections of normal mice and the OKN-defective mutant mice beige, beige-J, and pearl. J. Comp. Neurol. *258*, 435–446. 10.1002/cne.902580311.
26. Oyster, C.W., Takahashi, E., and Collewijn, H. (1972). Direction-selective retinal ganglion cells and control of optokinetic nystagmus in the rabbit. Vision Res. *12*, 183–193. 10.1016/0042-6989(72)90110-1.
27. Wei, W. (2018). Neural Mechanisms of Motion Processing in the Mammalian Retina. Annu. Rev. Vis. Sci. *4*, 165–192. 10.1146/annurev-vision-091517-034048.
28. Takahashi, M., Sakurai, S., and Kanzaki, J. (1978). Horizontal and Vertical Optokinetic Nystagmus in Man. ORL J Otorhinolaryngol Relat Spec *40*, 43–52. 10.1159/000275385.
29. Hainline, L., Lemerise, E., Abramov, I., and Turkel, J. (1984). Orientational asymmetries in small-field optokinetic nystagmus in human infants. Behav. Brain Res. *13*, 217–230. 10.1016/0166-4328(84)90164-5.
30. Murasugi, C.M., and Howard, I.P. (1989). Up-down asymmetry in human vertical optokinetic nystagmus and afternystagmus: contributions of the central and peripheral retinae. Exp. Brain Res. *77*, 183–192. 10.1007/BF00250580.
31. van den Berg, A.V., and Collewijn, H. (1988). Directional asymmetries of human optokinetic nystagmus. Exp. Brain Res. *70*, 597–604. 10.1007/BF00247608.
32. Knapp, C.M., Proudlock, F.A., and Gottlob, I. (2013). OKN Asymmetry in Human Subjects: A Literature Review. Strabismus *21*, 37–49. 10.3109/09273972.2012.762532.
33. Hoffmann, K.-P., and Fischer, W.H. (2001). Directional effect of inactivation of the nucleus of the optic tract on optokinetic nystagmus in the cat. Vision Res. *41*, 3389–3398. 10.1016/S0042-6989(01)00184-5.
34. Evinger, C., and Fuchs, A.F. (1978). Saccadic, smooth pursuit, and optokinetic eye

movements of the trained cat. J. Physiol. *285*, 209–229. 10.1113/jphysiol.1978.sp012568.
35. Grasse, K.L., and Cynader, M.S. (1988). The effect of visual cortex lesions on vertical optokinetic nystagmus in the cat. Brain Res. *455*, 385–389. 10.1016/0006-8993(88)90100-X.
36. Wallman, J., and Velez, J. (1985). Directional asymmetries of optokinetic nystagmus: developmental changes and relation to the accessory optic system and to the vestibular system. J. Neurosci. *5*, 317–329. 10.1523/JNEUROSCI.05-02-00317.1985.
37. Takahashi, M., and Igarashi, M. (1977). Comparison of Vertical and Horizontal Optokinetic Nystagmus in the Squirrel Monkey. ORL *39*, 321–329. 10.1159/000275374.
38. Denman, D.J., Siegle, J.H., Koch, C., Reid, R.C., and Blanche, T.J. (2017). Spatial Organization of Chromatic Pathways in the Mouse Dorsal Lateral Geniculate Nucleus. J. Neurosci. *37*, 1102–1116. 10.1523/JNEUROSCI.1742-16.2016.
39. Yonehara, K., Fiscella, M., Drinnenberg, A., Esposti, F., Trenholm, S., Krol, J., Franke, F., Scherf, B.G., Kusnyerik, A., Müller, J., et al. (2016). Congenital Nystagmus Gene FRMD7 Is Necessary for Establishing a Neuronal Circuit Asymmetry for Direction Selectivity. Neuron *89*, 177–193. 10.1016/j.neuron.2015.11.032.
40. Briggman, K.L., Helmstaedter, M., and Denk, W. (2011). Wiring specificity in the direction-selectivity circuit of the retina. Nature *471*, 183–188. 10.1038/nature09818.
41. Fried, S.I., Münch, T.A., and Werblin, F.S. (2002). Mechanisms and circuitry underlying directional selectivity in the retina. Nature *420*, 411–414. 10.1038/nature01179.
42. Wei, W., Hamby, A.M., Zhou, K., and Feller, M.B. (2011). Development of asymmetric inhibition underlying direction selectivity in the retina. Nature *469*, 402–406. 10.1038/nature09600.
43. Ding, H., Smith, R.G., Poleg-Polsky, A., Diamond, J.S., and Briggman, K.L. (2016). Species-specific wiring for direction selectivity in the mammalian retina. Nature *535*, 105–110. 10.1038/nature18609.
44. Amthor, F.R., Keyser, K.T., and Dmitrieva, N.A. (2002). Effects of the destruction of starburst-cholinergic amacrine cells by the toxin AF64A on rabbit retinal directional selectivity. Vis. Neurosci. *19*, 495–509. 10.1017/S0952523802194119.
45. Yonehara, K., Balint, K., Noda, M., Nagel, G., Bamberg, E., and Roska, B. (2011). Spatially asymmetric reorganization of inhibition establishes a motion-sensitive circuit. Nature *469*, 407–410. 10.1038/nature09711.
46. Yoshida, K., Watanabe, D., Ishikane, H., Tachibana, M., Pastan, I., and Nakanishi, S. (2001). A Key Role of Starburst Amacrine Cells in Originating Retinal Directional Selectivity and Optokinetic Eye Movement. Neuron *30*, 771–780. 10.1016/S0896-6273(01)00316-6.
47. Mauss, A.S., Vlasits, A., Borst, A., and Feller, M. (2017). Visual Circuits for Direction Selectivity. Annu. Rev. Neurosci. *40*, 211–230. 10.1146/annurev-neuro-072116-031335.
48. Vaney, D.I., Sivyer, B., and Taylor, W.R. (2012). Direction selectivity in the retina: symmetry and asymmetry in structure and function. Nat. Rev. Neurosci. *13*, 194–208. 10.1038/nrn3165.
49. Mani, A., Yang, X., Zhao, T., Leyrer, M.L., Schreck, D., and Berson, D.M. (2021). A retinal circuit that vetoes optokinetic responses to fast visual motion (Neuroscience) 10.1101/2021.10.31.466688.
50. Matsumoto, A., Briggman, K.L., and Yonehara, K. (2019). Spatiotemporally Asymmetric Excitation Supports Mammalian Retinal Motion Sensitivity. Curr. Biol. *29*, 3277-3288.e5. 10.1016/j.cub.2019.08.048.
51. Koulen, P., Fletcher, E.L., Craven, S.E., Bredt, D.S., and Wässle, H. (1998). Immunocytochemical Localization of the Postsynaptic Density Protein PSD-95 in the Mammalian Retina. J. Neurosci. *18*, 10136–10149. 10.1523/JNEUROSCI.18-23-10136.1998.
52. Sassoè-Pognetto, M., Kirsch, J., Grünert, U., Greferath, U., Fritschy, J.M., Möhler, H., Betz,

H., and Wässle, H. (1995). Colocalization of gephyrin and GABAA-receptor subunits in the rat retina. J. Comp. Neurol. *357*, 1–14. 10.1002/cne.903570102.
53. Sassoè-Pognetto, M., and Wässle, H. (1997). Synaptogenesis in the rat retina: subcellular localization of glycine receptors, GABAA receptors, and the anchoring protein gephyrin. J. Comp. Neurol. *381*, 158–174. 10.1002/(SICI)1096-9861(19970505)381:2<158::AID-CNE4>3.0.CO;2-2.
54. Matsumoto, A., Agbariah, W., Nolte, S.S., Andrawos, R., Levi, H., Sabbah, S., and Yonehara, K. (2021). Direction selectivity in retinal bipolar cell axon terminals. Neuron *0*. 10.1016/j.neuron.2021.07.008.
55. Percival, K.A., Venkataramani, S., Smith, R.G., and Taylor, W.R. (2019). Directional excitatory input to direction-selective ganglion cells in the rabbit retina. J. Comp. Neurol. *527*, 270–281. 10.1002/cne.24207.
56. Poleg-Polsky, A., and Diamond, J.S. (2011). Imperfect Space Clamp Permits Electrotonic Interactions between Inhibitory and Excitatory Synaptic Conductances, Distorting Voltage Clamp Recordings. PLOS ONE *6*, e19463. 10.1371/journal.pone.0019463.
57. Summers, M.T., and Feller, M.B. (2022). Distinct inhibitory pathways control velocity and directional tuning in the mouse retina. Curr. Biol. 10.1016/j.cub.2022.03.054.
58. Yonehara, K., Farrow, K., Ghanem, A., Hillier, D., Balint, K., Teixeira, M., Jüttner, J., Noda, M., Neve, R.L., Conzelmann, K.-K., et al. (2013). The First Stage of Cardinal Direction Selectivity Is Localized to the Dendrites of Retinal Ganglion Cells. Neuron *79*, 1078–1085. 10.1016/j.neuron.2013.08.005.
59. Oesch, N., Euler, T., and Taylor, W.R. (2005). Direction-Selective Dendritic Action Potentials in Rabbit Retina. Neuron *47*, 739–750. 10.1016/j.neuron.2005.06.036.
60. Poleg-Polsky, A., and Diamond, J.S. (2016). NMDA Receptors Multiplicatively Scale Visual Signals and Enhance Directional Motion Discrimination in Retinal Ganglion Cells. Neuron *89*, 1277–1290. 10.1016/j.neuron.2016.02.013.
61. Poleg-Polsky, A., and Diamond, J.S. (2016). Retinal Circuitry Balances Contrast Tuning of Excitation and Inhibition to Enable Reliable Computation of Direction Selectivity. J. Neurosci. *36*, 5861–5876. 10.1523/JNEUROSCI.4013-15.2016.
62. Sethuramanujam, S., McLaughlin, A.J., deRosenroll, G., Hoggarth, A., Schwab, D.J., and Awatramani, G.B. (2016). A Central Role for Mixed Acetylcholine/GABA Transmission in Direction Coding in the Retina. Neuron *90*, 1243–1256. 10.1016/j.neuron.2016.04.041.
63. Sethuramanujam, S., Yao, X., deRosenroll, G., Briggman, K.L., Field, G.D., and Awatramani, G.B. (2017). “Silent” NMDA Synapses Enhance Motion Sensitivity in a Mature Retinal Circuit. Neuron *96*, 1099-1111.e3. 10.1016/j.neuron.2017.09.058.
64. Soodak, R.E., and Simpson, J.I. (1988). The accessory optic system of rabbit. I. Basic visual response properties. J. Neurophysiol. *60*, 2037–2054. 10.1152/jn.1988.60.6.2037.
65. Giolli, R.A., Peterson, G.M., Ribak, C.E., McDonald, H.M., Blanks, R.H., and Fallon, J.H. (1985). GABAergic neurons comprise a major cell type in rodent visual relay nuclei: an immunocytochemical study of pretectal and accessory optic nuclei. Exp. Brain Res. *61*, 194–203. 10.1007/bf00235635.
66. Grasse, K.L., and Cynader, M.S. (1982). Electrophysiology of medial terminal nucleus of accessory optic system in the cat. J. Neurophysiol. *48*, 490–504. 10.1152/jn.1982.48.2.490.
67. Natal, C.L., and Britto, L.R.G. (1988). The rat accessory optic system: effects of cortical lesions on the directional selectivity of units within the medial terminal nucleus. Neurosci. Lett. *91*, 154–159. 10.1016/0304-3940(88)90760-4.
68. Simpson, J.I., Soodak, R.E., and Hess, R. (1979). The Accessory Optic System and its Relation to the Vestibulocerebellum. In Progress in Brain Research Reflex Control of Posture And Movement., R. Granit and O. Pompeiano, eds. (Elsevier), pp. 715–724. 10.1016/S0079-6123(08)60868-7.

69. Mowrer, O.H. (1936). A comparison of the reaction mechanisms mediating optokinetic nystagmus in human beings and in pigeons. Psychol. Monogr. *47*, 294–305. http://dx.doi.org/10.1037/h0093419.
70. Liu, B., Huberman, A.D., and Scanziani, M. (2016). Cortico-fugal output from visual cortex promotes plasticity of innate motor behaviour. Nature *538*, 383–387. 10.1038/nature19818.
71. Wood, C.C., Spear, P.D., and Braun, J.J. (1973). Direction-specific deficits in horizontal optokinetic nystagmus following removal of visual cortex in the cat. Brain Res. *60*, 231–237. 10.1016/0006-8993(73)90862-7.
72. Cook, J.E., and Podugolnikova, T.A. (2001). Evidence for spatial regularity among retinal ganglion cells that project to the accessory optic system in a frog, a reptile, a bird, and a mammal. Vis. Neurosci. *18*, 289–297. 10.1017/S0952523801182131.
73. Dann, J.F., and Buhl, E.H. (1987). Retinal ganglion cells projecting to the accessory optic system in the rat. J. Comp. Neurol. *262*, 141–158. 10.1002/cne.902620111.
74. Ruff, T., Peters, C., Matsumoto, A., Ihle, S.J., Morales, P.A., Gaitanos, L., Yonehara, K., del Toro, D., and Klein, R. (2021). FLRT3 Marks Direction-Selective Retinal Ganglion Cells That Project to the Medial Terminal Nucleus. Front. Mol. Neurosci. *14*.
75. Tauber, E.S., and Atkin, A. (1968). Optomotor Responses to Monocular Stimulation: Relation to Visual System Organization. Science *160*, 1365–1367.
76. Holmgren, C.D., Stahr, P., Wallace, D.J., Voit, K.-M., Matheson, E.J., Sawinski, J., Bassetto, G., and Kerr, J.N. (2021). Visual pursuit behavior in mice maintains the pursued prey on the retinal region with least optic flow. eLife *10*, e70838. 10.7554/eLife.70838.
77. Al-Khindi, T., Sherman, M.B., Kodama, T., Gopal, P., Pan, Z., Kiraly, J.K., Zhang, H., Goff, L.A., du Lac, S., and Kolodkin, A.L. (2022). The transcription factor Tbx5 regulates direction-selective retinal ganglion cell development and image stabilization. Curr. Biol. 10.1016/j.cub.2022.07.064.
78. Lee, S., Chen, L., Chen, M., Ye, M., Seal, R.P., and Zhou, Z.J. (2014). An unconventional glutamatergic circuit in the retina formed by vGluT3 amacrine cells. Neuron *84*, 708–715. 10.1016/j.neuron.2014.10.021.
79. Sivyer, B., Tomlinson, A., and Taylor, W.R. (2019). Simulated Saccadic Stimuli Suppress ON-Type Direction-Selective Retinal Ganglion Cells via Glycinergic Inhibition. J. Neurosci. *39*, 4312–4322. 10.1523/JNEUROSCI.3066-18.2019.
80. Kittila, C.A., and Massey, S.C. (1997). Pharmacology of Directionally Selective Ganglion Cells in the Rabbit Retina. J. Neurophysiol. *77*, 675–689. 10.1152/jn.1997.77.2.675.
81. Sivyer, B., and Williams, S.R. (2013). Direction selectivity is computed by active dendritic integration in retinal ganglion cells. Nat. Neurosci. *16*, 1848–1856. 10.1038/nn.3565.
82. Carandini, M., and Heeger, D.J. (2012). Normalization as a canonical neural computation. Nat. Rev. Neurosci. *13*, 51–62. 10.1038/nrn3136.
83. Barlow, H.B. (1953). Summation and inhibition in the frog's retina. J. Physiol. *119*, 69–88.
84. Hartline, H.K., Wagner, H.G., and MacNichol, E.F. (1952). The Peripheral Origin of Nervous Activity in the Visual System. Cold Spring Harb. Symp. Quant. Biol. *17*, 125–141. 10.1101/SQB.1952.017.01.013.
85. Kuffler, S.W. (1953). Discharge patterns and functional organization of mammalian retina. J. Neurophysiol. *16*, 37–68. 10.1152/jn.1953.16.1.37.
86. Dacey, D.M., Crook, J.D., and Packer, O.S. (2014). Distinct synaptic mechanisms create parallel S-ON and S-OFF color opponent pathways in the primate retina. Vis. Neurosci. *31*, 139–151. 10.1017/S0952523813000230.
87. De Monasterio, F.M., and Gouras, P. (1975). Functional properties of ganglion cells of the rhesus monkey retina. J. Physiol. *251*, 167–195. 10.1113/jphysiol.1975.sp011086.
88. Field, G.D., Greschner, M., Gauthier, J.L., Rangel, C., Shlens, J., Sher, A., Marshak, D.W., Litke, A.M., and Chichilnisky, E.J. (2009). High-sensitivity rod photoreceptor input to the blue-yellow color opponent pathway in macaque retina. Nat. Neurosci. *12*, 1159–1164.

10.1038/nn.2353.
89. Suver, M.P., Matheson, A.M.M., Sarkar, S., Damiata, M., Schoppik, D., and Nagel, K.I. (2019). Encoding of Wind Direction by Central Neurons in Drosophila. Neuron *102*, 828-842.e7. 10.1016/j.neuron.2019.03.012.
90. Martin, H. (1965). Osmotropotaxis in the Honey-Bee. Nature *208*, 59–63. 10.1038/208059a0.
91. Schwenk, K. (1994). Why snakes have forked tongues. Science *263*, 1573.
92. Middlebrooks, J.C., and Green, D.M. (1991). Sound Localization by Human Listeners. Annu. Rev. Psychol. *42*, 135–159. 10.1146/annurev.ps.42.020191.001031.
93. Peirce, J.W. (2007). PsychoPy—Psychophysics software in Python. J. Neurosci. Methods *162*, 8–13. 10.1016/j.jneumeth.2006.11.017.
94. Stahl, J.S., van Alphen, A.M., and De Zeeuw, C.I. (2000). A comparison of video and magnetic search coil recordings of mouse eye movements. J. Neurosci. Methods *99*, 101–110. 10.1016/S0165-0270(00)00218-1.
95. Stahl, J.S. (2004). Eye Movements of the Murine P/Q Calcium Channel Mutant Rocker, and the Impact of Aging. J. Neurophysiol. *91*, 2066–2078. 10.1152/jn.01068.2003.
96. Zoccolan, D., Graham, B.J., and Cox, D.D. (2010). A Self-Calibrating, Camera-Based Eye Tracker for the Recording of Rodent Eye Movements. Front. Neurosci. *4*, 193. 10.3389/fnins.2010.00193.
97. Rodieck, R.W. (1991). The density recovery profile: A method for the analysis of points in the plane applicable to retinal studies. Vis. Neurosci. *6*, 95–111. 10.1017/S095252380001049X.
98. Care, R.A., Kastner, D.B., De la Huerta, I., Pan, S., Khoche, A., Della Santina, L., Gamlin, C., Santo Tomas, C., Ngo, J., Chen, A., et al. (2019). Partial Cone Loss Triggers Synapse-Specific Remodeling and Spatial Receptive Field Rearrangements in a Mature Retinal Circuit. Cell Rep. *27*, 2171-2183.e5. 10.1016/j.celrep.2019.04.065.
99. Care, R.A., Anastassov, I.A., Kastner, D.B., Kuo, Y.-M., Santina, L.D., and Dunn, F.A. (2020). Mature Retina Compensates Functionally for Partial Loss of Rod Photoreceptors. Cell Rep. *31*. 10.1016/j.celrep.2020.107730.
100. Remtulla, S., and Hallett, P.E. (1985). A schematic eye for the mouse, and comparisons with the rat. Vision Res. *25*, 21–31. 10.1016/0042-6989(85)90076-8.
101. Antoine, M.W., Langberg, T., Schnepel, P., and Feldman, D.E. (2019). Increased Excitation-Inhibition Ratio Stabilizes Synapse and Circuit Excitability in Four Autism Mouse Models. Neuron *101*, 648-661.e4. 10.1016/j.neuron.2018.12.026.
102. Santina, L.D., Inman, D.M., Lupien, C.B., Horner, P.J., and Wong, R.O.L. (2013). Differential Progression of Structural and Functional Alterations in Distinct Retinal Ganglion Cell Types in a Mouse Model of Glaucoma. J. Neurosci. *33*, 17444–17457. 10.1523/JNEUROSCI.5461-12.2013.
103. Santina, L.D., Yu, A.K., Harris, S.C., Soliño, M., Ruiz, T.G., Most, J., Kuo, Y.-M., Dunn, F.A., and Ou, Y. (2021). Disassembly and rewiring of a mature converging excitatory circuit following injury. Cell Rep. *36*. 10.1016/j.celrep.2021.109463.